

Dissertation

submitted to the
Combined Faculties for the Natural Sciences and for Mathematics
of the
Ruperto-Carola University of Heidelberg, Germany
for the degree of
Doctor of Natural Sciences

Put forward by
Marco Linke
born in Wuppertal
Oral examination: 10.01.2017

Image analysis and modeling of cellular organization in micropatterned environments

Referees: Prof. Dr. Ulrich Schwarz
Prof. Dr. Heinz Horner

Bildanalyse und Modellierung der Zellorganisation in mikrostrukturierten Umgebungen

In der experimentellen Zellbiophysik ist es mittlerweile Standard geworden die Form und Organisation von adhärennten Zellen zu kontrollieren. Hierfür werden mikrostrukturierte Umgebungen verwendet, die mit Methoden aus den Materialwissenschaften hergestellt werden. Dadurch kann die zelluläre Variabilität reduziert werden, wodurch die statistische Analyse vereinfacht und einen detaillierter Vergleich mit mathematischen Modellen ermöglicht wird. In dieser Arbeit verbinden wir Bildverarbeitung mit computergestützter Modellierung und nutzen die Normierungseigenschaften von mikrostrukturierten Umgebungen um die Zellorganisation zu untersuchen. Im ersten Teil wenden wir Techniken der Bildanalyse an, um die Form und interne Struktur von Zellen zu charakterisieren. Hierzu analysieren wir zunächst, wie kontraktile Polymerbündel, sogenannte Stressfasern, die Form von adhärennten Zellen in zwei und drei Dimensionen bestimmen. Dann untersuchen wir die detaillierte Struktur dieser Bündel und quantifizieren außerdem den Einfluss von Stressfasern auf die zelluläre Kontraktionsdynamik. Schließlich analysieren wir, wie sich die Normierung der Zellform auf die Organisation des intrazellulären Polymernetzwerks der Mikrotubuli auswirkt. Im zweiten Teil der Arbeit entwickeln wir verschiedene Ansätze der computergestützten Modellierung um ein tieferes Verständnis für das Wechselspiel von Zellform und Mikrotubuli-Netzwerk zu erlangen. Wir stellen Modelle auf, die einerseits auf stochastischen Simulationen von Polymeren und andererseits auf einer effektiven Kontinuumstheorie für Flüssigkristalle basieren. Mit diesen Modellen können wir experimentelle Ergebnisse erklären und die interne Architektur von Zellen voraussagen, die auf Mikrostruktursubstraten adhärieren.

Image analysis and modeling of cellular organization in micropatterned environments

In experimental cellular biophysics, it has become standard practice to control the shape and organization of adherent cells. For this purpose, micropatterned environments are being used, which are fabricated using techniques from materials science. Thereby, cell variability can be reduced, which facilitates statistical analysis and allows for a detailed comparison to mathematical models. In this thesis we combine image processing with computational modeling and use the normalization properties of micropatterned environments to investigate cellular organization. In the first part, we apply image analysis techniques to study cell shape and internal organization. For this, we first analyze how contractile polymer bundles, so-called stress fibers, determine the shape of adherent cells in two and three dimensions. Next, we investigate the detailed structure of such bundles and quantify their influence on cellular contraction dynamics. In the second part of the thesis we develop different computational modeling approaches to gain deeper understanding into the interplay between cell shape and the microtubule network. We propose models that are based either on stochastic simulations of polymers or on an effective continuum theory for liquid crystals. With these models we can explain experimental results and predict the internal architecture of cells adhering to micropatterned substrates.

Contents

1. Introduction	1
1.1. Imaging techniques	1
1.2. Micropatterning techniques	4
1.2.1. Two-dimensional substrates	5
1.2.2. Three-dimensional scaffolds	7
1.3. Organelles and compartmentalization	9
1.4. The cytoskeleton	10
1.4.1. Actin	12
1.4.2. Microtubules	14
1.4.3. Intermediate filaments	17
1.4.4. Cytoskeletal crosstalk	17
1.4.5. Regulation of cellular contractility	18
1.5. Cell adhesion and cell shape	19
1.6. Models for cell shape	20
1.7. Outline of the thesis	22
I. Image Analysis	25
2. Image processing techniques	27
2.1. Image registration	28
2.2. Segmentation	29
2.3. Automated detection of circular arcs	32
2.4. Estimation of local orientation	34
2.4.1. Structure tensor	34
2.4.2. Coherency measure	35
2.4.3. Implementation	36
2.4.4. Circular statistics	37
2.5. Motion estimation	37
3. Analysis of the actin cytoskeleton using micropatterned environments	41
3.1. Automated fitting of circular arcs	41
3.1.1. Results	44
3.1.2. Discussion	45
3.2. Analysis of circular arcs in 3D	46
3.2.1. Cell shape in 3D microscaffolds	47

3.2.2.	Fitting of actin arcs in 3D	50
3.2.3.	Combining experimental results with theoretical modeling . . .	52
3.2.4.	Conclusion	53
3.3.	Analysis of stress fiber microstructure	54
3.3.1.	Localization of myosin II minifilaments	55
3.3.2.	Results and outlook	57
4.	Intracellular dynamics of the actin cytoskeleton	59
4.1.	Validation of the optical flow method	61
4.2.	Correlating cytoskeletal flow and stress fiber orientation	62
4.3.	Results	64
4.4.	Conclusion	69
5.	Analysis of the microtubule cytoskeleton	71
5.1.	Experiments	72
5.2.	Analysis	73
5.3.	Results and discussion	74
6.	Analysis of intracellular integrin accumulation in cells on micropatterns	79
6.1.	Spatial distribution maps for intracellular compartments	80
6.1.1.	Assessment of statistical significance	81
6.2.	Experimental procedure	81
6.2.1.	Validation of the experimental setup	82
6.3.	Influence of knockdown on cell-wide integrin accumulation	83
6.4.	Changes in the spatial distribution of internalized integrin	85
6.5.	Conclusion	86
II.	Modeling	87
7.	Modeling of the microtubule network	89
7.1.	Models for cytoskeletal organization	91
7.2.	Boundary definition and analysis of the proposed models	93
7.2.1.	Comparison of simulated orientation fields to the experiments .	94
8.	Filament based models	97
8.1.	Persistent random walk model	97
8.1.1.	Boundary interactions	99
8.1.2.	Partial versus complete depolymerization at concave boundaries	99
8.1.3.	Orientation fields on various micropatterns	102
8.1.4.	Comparison to experimental results	103
8.2.	Brownian dynamics: Cytosim	104
8.2.1.	Boundary interactions	105
8.2.2.	Binding and unbinding at the cell cortex	106

8.2.3. Orientation fields on various micropattern geometries	109
8.2.4. Comparison to the experiments	110
8.3. Comparison of the models	113
8.4. Discussion	115
9. Liquid crystal model	119
9.1. Introduction into liquid crystals	120
9.2. Applicability of a liquid crystal model to microtubules	122
9.3. Mathematical description of liquid crystals	123
9.3.1. Thermotropic energy	125
9.3.2. Elastic energy	126
9.3.3. Surface energy and boundary conditions	127
9.3.4. Scaling of the Landau–de Gennes free energy	128
9.4. Biologically motivated choice of boundary conditions	129
9.5. Numerical implementation	130
9.6. Influence of the parameters ε and W	132
9.7. Comparison to the experiments	135
9.8. Liquid crystal model compared to filament-based models	137
9.9. Conclusion	138
10. Conclusion	141
A. Appendix	145
A.1. Parameters for the persistent random walk simulations	145
A.2. Parameters for the Cytosim simulations	146
A.3. Derivation of the minimizer of the Landau–de Gennes free energy	147
A.4. Parameters for the liquid crystal model	148
Bibliography	149
List of abbreviations	169
List of manuscripts	171
Danksagung	173

1

Introduction

In this chapter we will give an overview of insights from multiple scientific fields that influence biophysical research. We will discuss advanced imaging techniques that are required to capture biological processes, about microfabrication techniques that have been transferred to biophysical research in order to control cellular behavior, about the basics of cellular function and organization, and about modeling approaches for cell shape that allow researchers to gain a deeper understanding of the experimental effects and their underlying principles.

1.1. Imaging techniques

Optical microscopy is one of the most commonly used techniques to study the detailed structure of organisms. A large number of advances in biological, biophysical or clinical research is due to observations of cellular behavior, only possible due to advances in imaging techniques. Nowadays the most widely used sample preparation technique for cell microscopy is the fluorescent labeling of subcellular components [1]. Such components are marked with antibodies, small proteins that bind only to specific subgroups of larger proteins, and these antibodies can in turn be tagged with fluorescent dyes. Another technique is a modification of the DNA in such a way that fluorescent proteins, e.g. green fluorescent protein (GFP), are expressed directly inside the cell.

Classical optical microscopy is limited by diffraction and Abbe's famous formula for the resolution limit of optical microscopes

$$d_{\text{Abbe}} = \frac{\lambda}{2n \sin \alpha} = \frac{\lambda}{2NA} \quad (1.1)$$

states that the minimum resolvable distance between two objects is given by half the wavelength λ divided by the refractive index n times the sine of the aperture angle α . $n \sin \alpha$ is also called the numerical aperture NA . The Rayleigh criterion, which states that the peaks of the diffraction pattern of two point sources can be distinguished if there is a drop of at least 26.5% between the peaks, defines the resolution limit as $d_{\text{Rayleigh}} = 0.61 \frac{\lambda}{NA}$ [2]. For typical wavelengths of $\lambda = 500 \text{ nm}$ and numerical apertures of $NA = 1.4$ the Rayleigh criterion yields $d_{\text{Rayleigh}} \approx 200 \text{ nm}$. Many structures in the cell are larger than this limit, but there are also small vesicles, proteins or filaments that fall below it and will appear blurred. In fact, the resolution limit applies only to the lateral direction and for imaging of voluminous objects there will be strong scattering along the axial direction which severely limits sectioning in this direction.

One technique that slightly increases the lateral resolution, but has a strong effect on axial resolution is confocal microscopy. Here, a pinhole is included in the beam path in front of the detector that blocks out scattered light from the axial direction and creates a very narrow depth of field of the microscope (Fig. 1.1a). Thus, the lateral and axial resolutions can be increased to

$$d_{\text{confocal, lateral}} = 0.44 \frac{\lambda}{NA} \quad (1.2)$$

$$d_{\text{confocal, axial}} = 1.4n \frac{\lambda}{NA}, \quad (1.3)$$

where the axial resolution limit depends on the refractive index n and is still three to four times larger than the lateral limit [2]. Confocal microscopy allows for optical sectioning in the axial direction and is therefore suitable for recording of volumetric images.

In the last 25 years various super-resolution microscopy techniques have emerged that allow imaging of structures, smaller than the classic Abbe limit [5]. One category are purely optical techniques, like 4Pi-microscopy, where light is collected by two objectives and can increase the axial resolution [6], or structured illumination microscopy (SIM) in which patterned illumination fields overlaid over the sample [7]. If such (sinusoidal) patterns are overlaid over structures with fine detail, they form moiré patterns, which can be imaged with widefield microscopy (Fig. 1.1b). The limited sampling of the reciprocal space with a radius $|\mathbf{k}_0|$ by a widefield microscope is extended to a region $|\mathbf{k}_0| + |\mathbf{k}_1|$ due to the sinusoidal patterns with frequency $|\mathbf{k}_1|$ (Fig. 1.1c). By rotating the illumination pattern the reciprocal space can be sampled isotropically [8]. The fine details can then be reconstructed by computational techniques.

The second set of techniques utilizes properties of the fluorophores to break the diffrac-

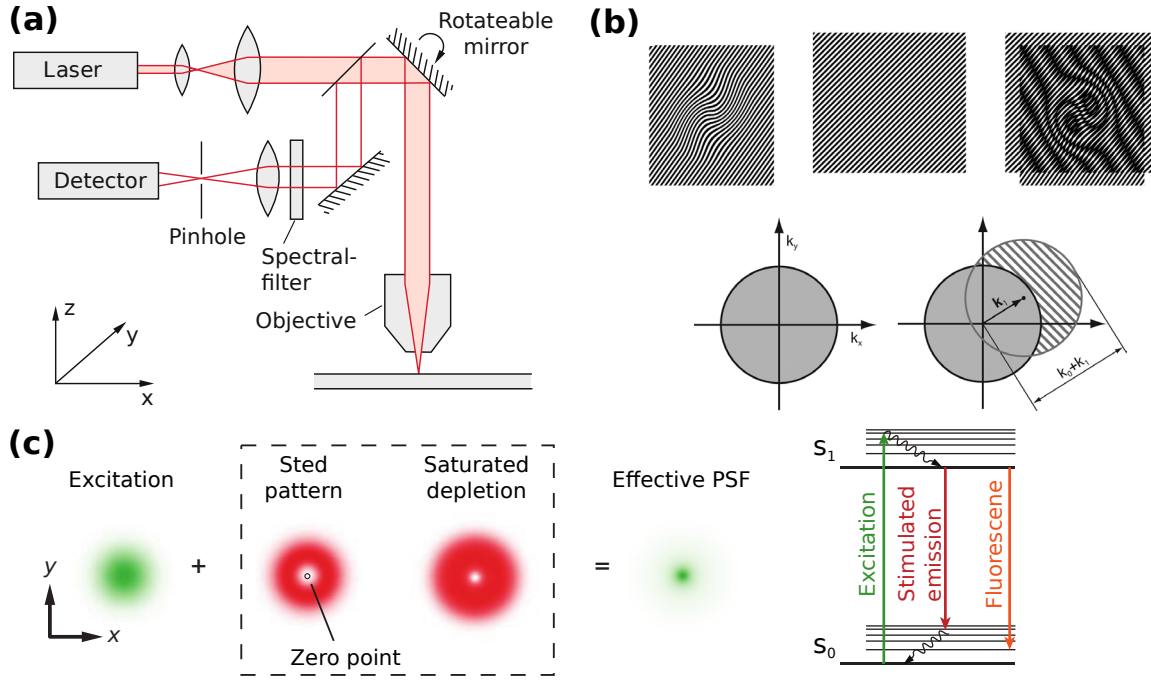


Figure 1.1.: (a) Schematic of a confocal laser scanning microscope. Pinhole removes scattered light from the axial direction. Rotateable mirror allows for scanning of the specimen. From [3]. (b) Principle of SIM illustrated by an overlay of two pattern with fine details into one moiré pattern that shows the structure at a larger scale, which can be imaged with a widefield microscope. Reconstruction of the fine details is done in post-processing. The frequency space explorable with a widefield microscope (gray center region) can be extended by sinusoidal illumination patterns [4]. By rotating the patterns the frequency space can be covered uniformly. (c) Principle of STED microscopy. An excitation beam is combined with a donut-shaped STED beam that deexcites fluorophores in all regions except its center and creates a spatially confined PSF. Deexcitation is achieved by stimulated emission, in which the relaxation from an excited state (S_1) into the ground state (S_0) is initiated by a an incident photon with suitable wavelength. From [5].

tion limit. The most well known techniques are stimulated emission depletion (STED) microscopy, photoactivated localization microscopy (PALM) and stochastic optical reconstruction microscopy (STORM), of which the former two have been awarded with the Nobel prize in chemistry in 2014 [9]. The ability of focusing a laser beam to one point is also diffraction limited and its extent is given by the point spread function (PSF) of the microscope, i.e. the response of the imaging system to a point source. STED uses one focused laser beam to excite fluorophores and a second, so called STED beam, to deplete the in a ring around the excitation beam. Thus, an effective PSF is created that has a much smaller extent than the original one and allows to resolve structures smaller than the diffraction limit [10] (Fig. 1.1d). STED requires high laser intensities that can lead to de-

struction of the fluorophores (bleaching) and not only requires to construction of suitable optics, but also the development of dyes that are more resistant to bleaching. Nowadays, commercially available STED microscopes can achieve resolutions below 30 nm [11].

In PALM [12, 13] and STORM [14] fluorophores are activated stochastically and to achieve a sparse emission pattern from molecules. The peaks of the PSFs can be estimated with high precision and by sequentially recording many images of stochastic activation patterns an image can be reconstructed. With these techniques lateral resolutions on the order of 25 nm can be reached [5].

There are numerous other microscopy techniques focusing on imaging of different aspects of the specimen, for example light sheet microscopy to image large volumes with high temporal resolution [15, 16]. For more information on this topic see [2, 5, 8, 17].

1.2. Micropatterning techniques

The advances in imaging techniques allow for very precise capture of cellular structure and dynamics, but the quantification of observations is often impeded by cellular variability. Cells are complex biological systems and already show a high degree of variability between cells of the same type and even more between different cell lines. This becomes especially evident if experiments are conducted on planar substrates with homogeneous coating of proteins that allow cells to spread and migrate (Fig. 1.2a). Most experimental work is conducted on such substrates and much effort has to be put into developing suitable analysis methods due to the high cellular variability.

With the onset high throughput screening for academic and commercial applications, such as genome-wide specific gene silencing by RNA interference (RNAi) [18], it is even more important to find experimental protocols that allow for fast and reliable analysis of image data. Here, the normalization of cell shape and intracellular structure by micropattern (MP) substrates can have significant impact on the screening efficiency.

Over the past two decades micropatterning (MP) techniques and specifically designed substrates have been used to control and manipulate cellular behavior. This section will give an overview of the techniques to fabricate such substrates in 2D and 3D geometries and also discuss applications to biophysical research.

1.2.1. Two-dimensional substrates

In 2D, cell spreading can be controlled by limiting the adhesive area available to cells and enforce spatial boundary conditions that should translate into a reduced variability in shape and intracellular organization [19].

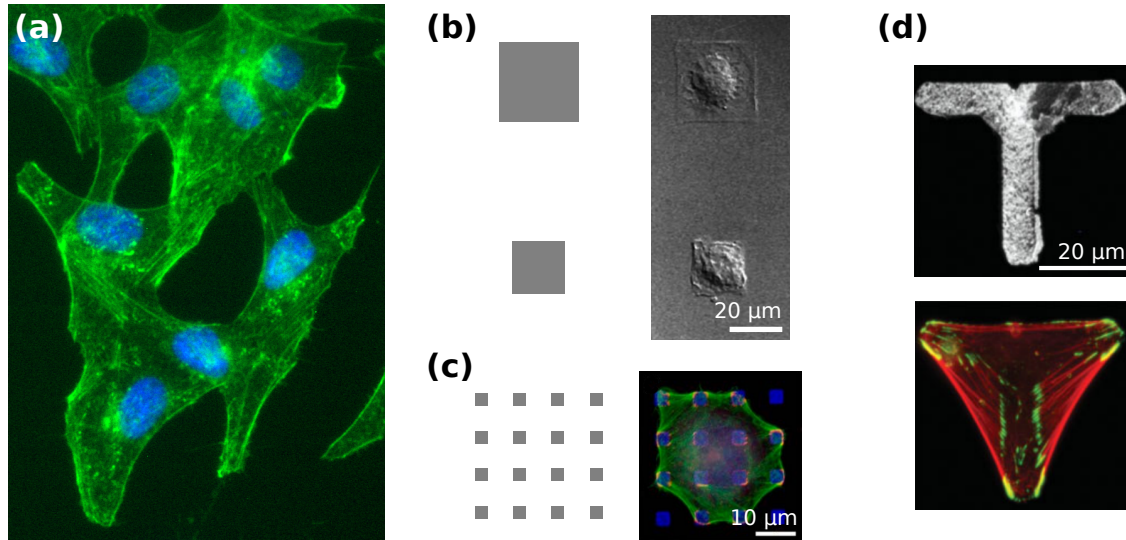


Figure 1.2.: Micropatterning techniques for cell shape normalization. **(a)** Fluorescent micrographs of cells adhering on a planar substrate with homogeneous protein coating show large variability in shape and organization. Actin is colored in green, the cell nucleus in blue. Image is courtesy of Vytaute Starkuviene-Erfle. **(b)** Square-shaped adhesive islands enable the cell to adopt a predefined shape. From [20]. **(c)** Microdot pattern allows for more flexibility in cell shape and the cell forms invaginated actin arcs with discrete spanning distances. From [21]. **(d)** Concave MPs (top) provide normalization in cell shape and also allows the formation of invaginated arcs at boundaries of the cell that span non-adhesive parts of the substrate. Actin is shown in red, the focal adhesion protein vinculin in green. From [22].

In seminal work Ingber and co-workers [23] designed substrates with adhesive islands by transferring the protein laminin to an otherwise nonadhesive substrate by microcontact printing [24]. Those islands confine cell spreading to a predefined geometry (Fig. 1.2b). Microcontact printing is one technique of the field of soft lithography that is also used to fabricate microfluidic devices, microelectromechanical systems or flexible electronics [25]. Stamps for such fabrications techniques are usually created out of the optically transparent elastomer poly(dimethylsiloxane) (PDMS). The stiffness of this elastomer can easily be controlled over several orders of magnitude from very soft (Young's modulus $E \approx 5$ kPa) to stiffer ($E \approx 2$ MPa) [26], but the material is still much softer than thermoplastics such as polycarbonate ($E \approx 2$ GPa) [27]. Typical values used for micro-

contact printing are $E \approx 0.5$ MPa. The PDMS technique allows to produce stamps with feature sizes on the order of 100 nm and masters for the stamps are usually fabricated by photolithographic techniques or electron-beam lithography [25].

The PDMS technique allows for cost effective production of MP substrates, which is why it is favored by many biological and biophysical laboratories, because a clean-room is only required for the initial production of the stamp master. Recently, new techniques have become available that allow fabrication of MP substrates directly by photolithographic processes [28]. Here, a photomask is used to directly graft extracellular matrix (ECM) proteins to a coated glass surface using the photo initiator benzophenone. Techniques like this allow to produce MP substrates in large quantities and make them commercially available [29].

With such MP substrates it has been shown, that cell shape rather than adhesion area is the most important factor for long-term survival and growth of cells [30]. There are also several studies, which were conducted using MP substrates, that suggest an influence of cell shape on stem cell differentiation [31–33].

In a series of influential papers Bornens, Théry and co-workers advanced the use of MP substrates to investigate intracellular organization. Using concave MPs, they related the cellular division axis [34], the distribution of stress fibers (SFs) [22] and cellular polarization [35] to cell shape (Fig. 1.2d).

In [35], the authors found that centrosome and Golgi position were located close to the cell centroid (more details on cellular organization will be given in Section 1.3), whereas the average nucleus position was off-centered towards the non-adhesive edges of the cell (Fig. 1.3a). Due to the shape normalization properties of the MPs, cell images can be aligned and averaged to create a spatial distribution profile of, for example, the actin cytoskeleton (CSK) (Fig. 1.3b,c)

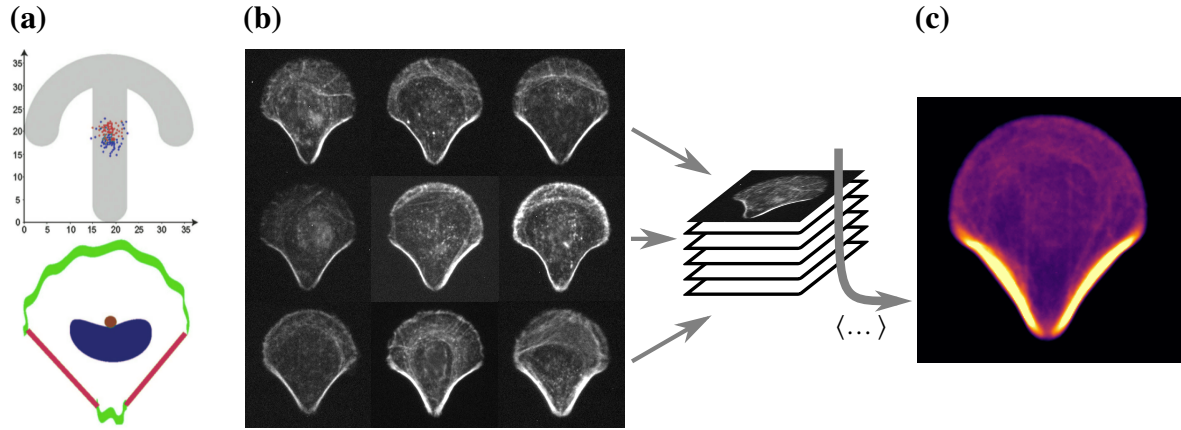


Figure 1.3.: Analysis of cellular organization using MP substrates. **(a)** A Υ -shaped MP (top) is used to enforce a regular cell shape (bottom), with actin cortex at adhesive edges (green), SFs spanning non-adhesive regions (red), nucleus (blue) and centrosome (orange) at well-defined positions. Dots in the upper figure symbolize positions of the cell nucleus (blue) and centrosome (orange) measured in multiple cells. Figure modified from [35]. **(b)** Cells adhering to a regular grid of MPs show normalization in cellular organization (fluorescent staining of actin). Individual cell images are collected into an image stack and averaging can be performed to obtain the distribution of the actin network in a typical cell, **(c)**. Bright colors correspond to high actin density. Images from a collaboration with Vytaute Starkuviene-Erfle.

1.2.2. Three-dimensional scaffolds

While planar substrates have a lot of advantages in fabrication, experimental procedures and imaging, they are also a large simplification of the ECM geometry found *in vivo*. Multiple fabrication methods exist that aim at the creation of artificial ECMs by designing 3D matrices. Here, we will mention only the most general principles and point to an extensive review for further details on the experimental procedures [36].

Perhaps the simplest method of generating a 3D matrix is to mix cells with a hydrogel solution and initialize the gelling process by changing the physical or chemical conditions [37]. Such matrigels provide a more realistic ECM to numerous cell types and can induce behavior that resembles the cells natural function. For example, breast epithelial cells cultured in a 3D matrix secrete milk proteins, which cannot be observed on planar substrates [38]. A drawback of matrigels is that the pore size can only be controlled indirectly, which might hinder cell migration [36].

More controlled approaches of creating artificial ECMs include electrospinning of fibers with controllable diameter that can be assembled into a fibrous matrix, to mimic for example the collagen network present in many tissues. Another technique is the cre-

ation of sponge-like matrices by gas-foaming, where compressed polymers are exposed to CO₂ under high pressure, which infiltrates the polymer and creates a porous structure [36]. Also microfluidic techniques, where bubbles of controllable size are placed in gelatin, can be used to create very regular scaffolds [39, 40]. Due to greater control over the pore size and interconnectivity, such materials are more suited for cell migration assays or can be used for clinical applications such as bone tissue engineering [41].

Another group of fabrication techniques are computer-assisted methods, which can be summarized under the general term 3D printing. Here, structures are created layer-by-layer by either selective laser sintering of powdered materials, inkjet-like printing or nozzle-based techniques [36]. Artificial fabrication of organs and tissues, where mixtures of cells and ECM proteins are directly printed by the methods mentioned above, are an area of extensive ongoing research with large potential for clinical applications (see [42] for an extensive review).

The method of direct laser writing has large potential (Fig. 1.4a) for material science as well as biophysical research. This technique was originally developed for the fabrication of artificial crystals, so called photonic metamaterials, that enable magnetism at optical frequencies [43, 44]. A magnetic permeability of $\mu \neq 1$, or even $\mu < 0$ can be induced by such materials, which can lead to a negative refractive index [45]. Such metamaterials find application in antennas with precise directional control [46], could be used for superlenses that can overcome the diffraction limit [47] or cloaking devices that redirect the electromagnetic field around an object in such a way that it cannot be detected in the far field [48].

For applications focusing on mechanical properties of cells, DLW can be used to create microscaffolds for controlled cell adhesion. Here, a photoresist is exposed to focused laser light and polymerization is induced by two-photon absorption [49]. Such structures can be functionalized by either using two-component photoresists [50] or by applying surface chemical methods in a second round of exposure to laser light [51] (Fig. 1.4a,b). Structures like this have been used for example to study the mechanical behavior and reinforcement processes of the CSK upon external deformation [52]. They can also be used to study cell shape in 3D (Fig. 1.4c,d).

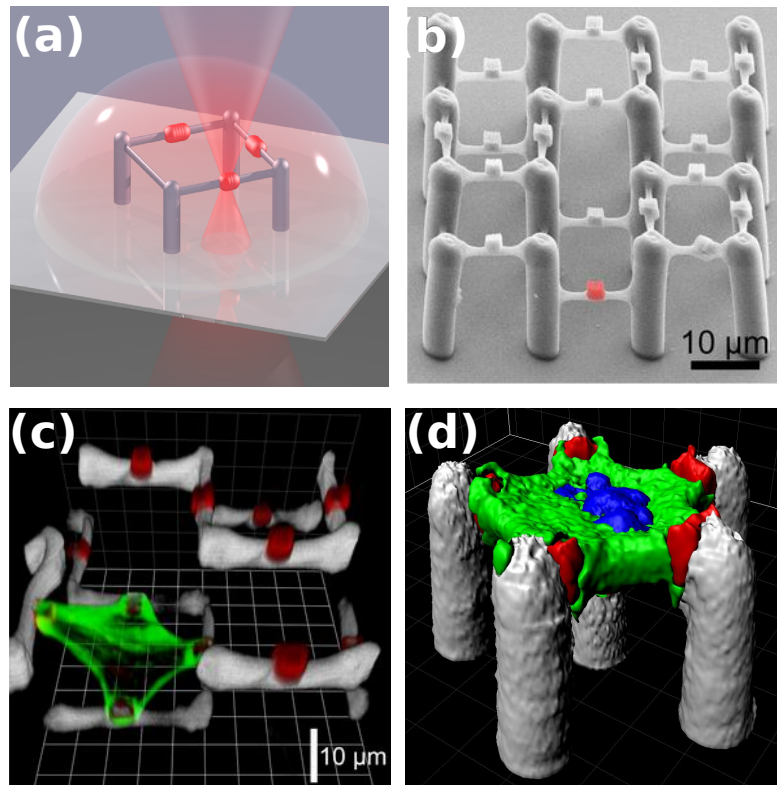


Figure 1.4.: Fabrication of micro scaffolds by direct laser writing. **(a)** Focused laser light initiates polymerization of a photo resist to write structures. **(b)** Electron microscopy image of fabricated scaffolds with one of the functionalized cuboids highlighted in red. **(c)** Reconstruction of an image obtained by confocal microscopy showing a cell (green) adhering inside the scaffold. **(d)** Reconstruction of a cell (green) with cell nucleus (blue) adhering in a pentagonal structure (gray) at functionalized cuboids (red). Images are courtesy of the group of Martin Bastmeyer.

1.3. Organelles and compartmentalization

On the cellular level, the living world can be divided into two categories: Prokaryotes and eukaryotes [1]. The main difference between the former and the latter is, that eukaryotes enclose their DNA in a compartment called the nucleus, while in prokaryotes no such compartment exists. While prokaryotes are exclusively single-celled organisms (bacteria and archaea), eukaryotes exist as single- or multi-celled organisms. Prokaryotes are easier to study due to their simpler internal organization and smaller genome [53], but the more diverse role of eukaryotic cells and especially the relevance for clinical applications makes it highly desirable to investigate their structure and function.

Eukaryotic cells have a more hierarchical intracellular structure than prokaryotes with well defined membrane-enclosed compartments (cf. Fig. 1.5). Compartmentalization al-

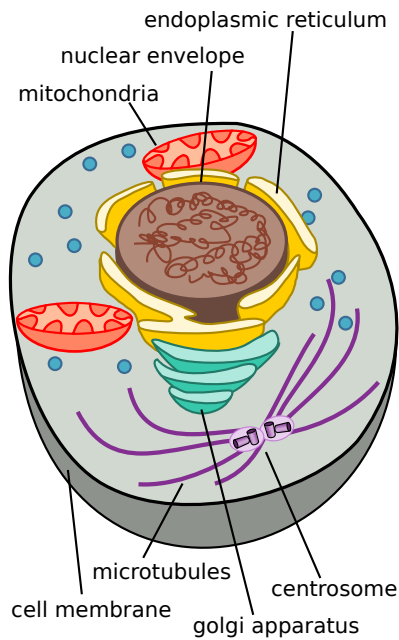


Figure 1.5.: Internal structure of an eukaryotic cell. The cell nucleus carries the genetic material in form of decondensed chromosomes and is enclosed by the nuclear envelope. Endoplasmic reticulum localizes around nucleus and is involved in protein and lipid synthesis. Golgi apparatus is involved in protein synthesis and intracellular trafficking. Mitochondria are the main energy generators in the cell. Microtubules are anchored at the centrosome and form the mitotic spindle during cell division. Other compartments are shown in blue, but might differ in size, function and internal structure. For more details on the function of the compartments and the cycle of cell division see main text. Figure modified from [54].

lows for more complex cellular functions necessary for higher organisms.

The nucleus is the largest and most prominent intracellular compartment as it stores the genetic material of the organism, but it occupies only 6% of the cellular volume in comparison to 22% for numerous smaller mitochondria, which are responsible for energy conversion in cells by phosphorylation of Adenosine diphosphate (ADP) to Adenosine triphosphate (ATP) [1]. Other compartments of varying size, like the endoplasmic reticulum, the Golgi apparatus or various endosomes are involved in functions like protein synthesis, degradation and sorting. Not all eukaryotic cells show the compartmentalized structure discussed above. Red blood cells, for example have no cell nucleus or other compartments [1].

1.4. The cytoskeleton

The extracellular environment in higher organisms is very diverse and therefore mechanisms and structures are needed to enable eukaryotic cells to adapt to these environments. An important element is the extracellular matrix (ECM), which is mixture of various proteins and polysaccharides and determines the mechanical properties of tissue and also enables cellular signaling [1].

The cell is not just a passive membrane shell with compartments floating around in it,

but rather it should be considered as an active system that has to resist external stresses and strains due to changes in the ECM and it needs to be able to exert forces onto the ECM, move through it, or modify it. Such mechanical interactions are mediated by the CSK, an assembly of various types of filaments, molecular motors as well as crosslinking and regulatory proteins. The CSK provides mechanical integrity for the cell by reinforcing the otherwise fragile cell membrane, it helps the cell to sense its extracellular environment, enables individual cells to move or arrays of cells to generate macroscopic movement of muscles, or allows neurons to extend dendrites and axon to form connections [55]. Apart from mechanical functions, the CSK also serves the function of directed intracellular transport of different kinds of proteins.

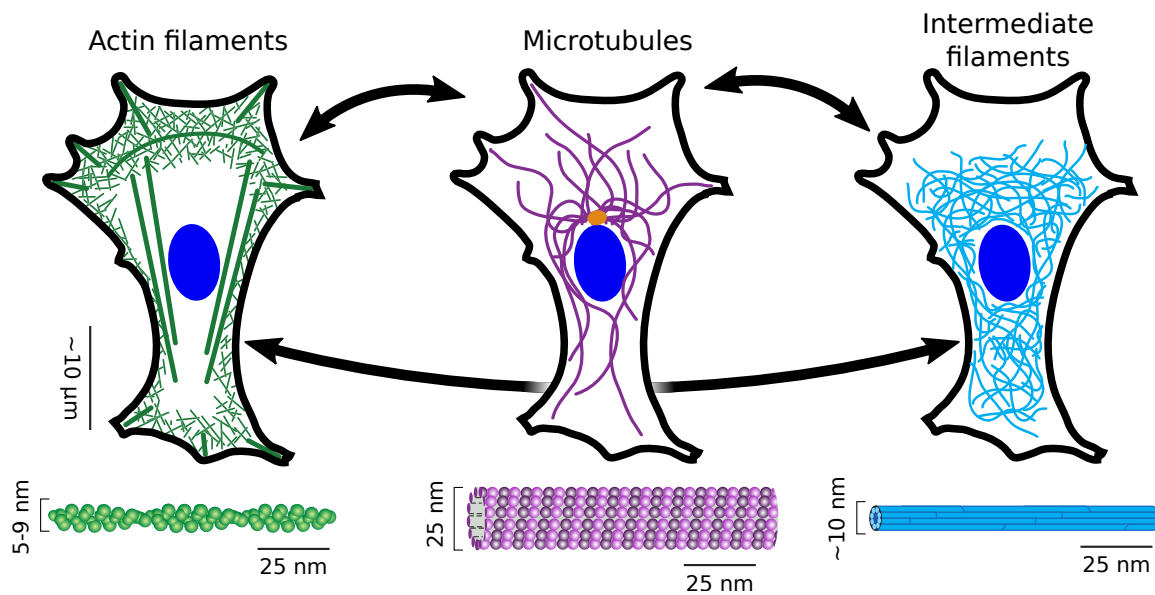


Figure 1.6.: Schematic drawing of the three different types of filamentous proteins constituting the CSK. All filaments mutually interact via various crosslinkers and molecular motors. Cell nucleus is shown in blue. Figure adapted from [1, 56].

The three main components of the CSK are the polymers actin filaments (AFs), microtubules (MTs) and intermediate filaments (Fig. 1.6). Though their function and mechanical properties are very distinct, they all consist of smaller protein subunits that polymerize and disassemble dynamically. Individual components are held together only by weak noncovalent interactions, which allows the cell to rapidly adapt to changes in the extracellular environment. For example to change its direction of movement by disassembling the CSK filaments at one side of the cell and initiate polymerization at another part. It also means that there are no CSK filaments that are static over extended periods of time and turnover rates range from milliseconds, during polymerization of AF and microtubules,

up to hours for the recycling of intermediate filaments [56].

The diameter of the filamentous polymer of the CSK is on the order of 10 nm and therefore is small compared to the range of filament length of $L \approx 0.1 - 10 \mu\text{m}$. A commonly used quantity to describe fluctuations in the shape of polymers is the persistence length l_p . It sets an arc length ξ of a polymer, on which significant bending fluctuations occur. One can define the persistence length in terms of the correlation function g of the tangent vectors τ [57]

$$g(\xi) = \langle \tau(\xi) \cdot \tau(0) \rangle = e^{-\xi/l_p}. \quad (1.4)$$

CSK filaments can be considered as elastic inextensible rods with a bending Hamiltonian

$$\mathcal{H}_{\text{bend}} = \frac{\kappa}{2} \int_0^L \left| \frac{d\tau}{d\xi} \right|^2 d\xi, \quad (1.5)$$

where the flexural rigidity $\kappa = EI$ is the product of the Young's modulus E and the geometric moment I . For an elastic rod with constant radius of curvature R and length L the bending energy is

$$U_{\text{bend}} = \frac{EIL}{2R^2}. \quad (1.6)$$

With typical values for the flexural rigidity of AFs, $\kappa_{\text{actin}} \approx 7 \cdot 10^{-26} \text{ N m}$, and the filament length, $L \approx 1 \mu\text{m}$, a bending energy on the order of $k_B T \approx 4 \cdot 10^{-21} \text{ J}$ corresponds to a radius of curvature of $R \approx 3 \mu\text{m}$. Using Eq. (1.5) and the equipartition theorem, in three dimensions, the persistence length l_p can be defined as the ratio between flexural rigidity and thermal energy [58]

$$l_p = \frac{EI}{k_B T}. \quad (1.7)$$

A more detailed discussion of this will be given in Section 8.1. CSK filaments can be considered as semiflexible polymers in the sense that their contour length is on the order of their persistence length and they are neither completely straight rods nor very flexible chains.

1.4.1. Actin

Actin is the most common protein in mammalian cells [59] and was also the first CSK component to be discovered. The first attempts of extracting actin from muscle cells date back to the late 19th century [60] and the first isolation of pure actin is credited to Straub and Szent-Györgyi [61]. Straub and Feuer [62] also discovered the involvement of ATP in actin polymerization. Actin monomers (G-actin) polymerize into AF (F-actin), which

are flexible, two-stranded polymers with a diameter of 5-9 nm and a persistence length of $l_p^{\text{actin}} \approx 17 \mu\text{m}$ [63]. These filaments can be characterized by a fast growing end (plus-end or barbed end) and a slow growing end (minus-end or pointed end) with different polymerization rates that reflect filament polarity.

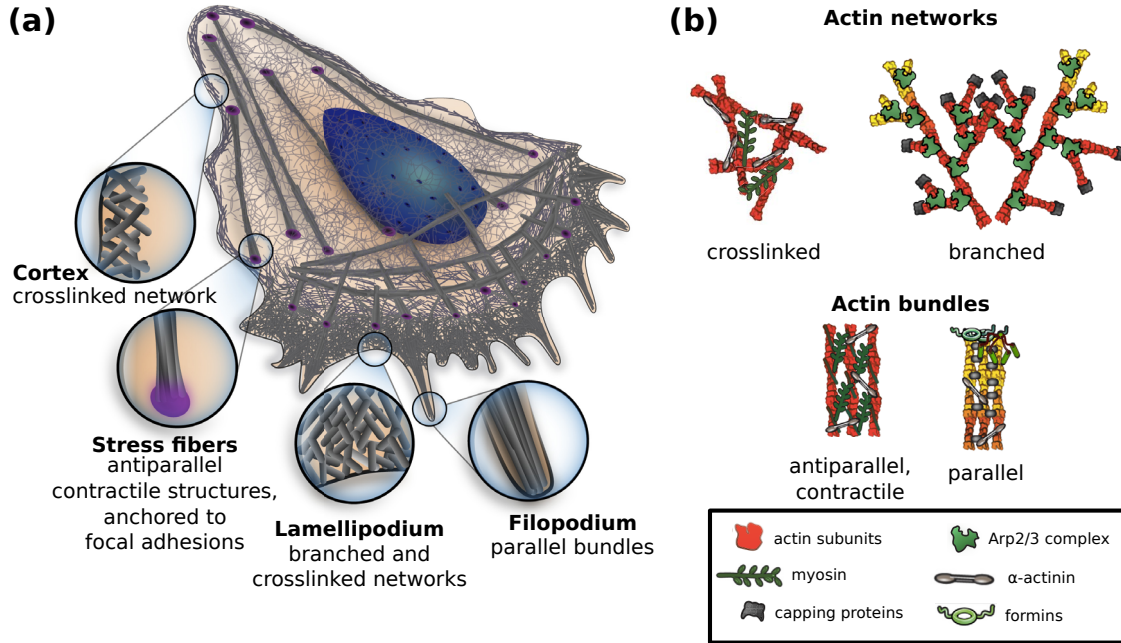


Figure 1.7.: (a) Schematic drawing of the various components of the actin CSK. (b) Detailed structure of actin networks and actin bundles with the most important proteins highlighted. For more details about structure and function see main text. Figure modified from [64].

Actin filaments can form crosslinked, contractile networks if they are combined with the myosin family of molecular motors. These proteins perform step-like motion along AFs by ATP hydrolysis and can generate a force on the order of 1 pN per myosin head [57]. Myosins can be categorized into plus-end targeting and minus-end targeting motors and can also act as crosslinkers by connecting adjacent AFs. Such networks can be found for example at the cell cortex, where the plasma membrane is reinforced from the inside and maintenance as well as changes of cell shape can be established (Fig. 1.7a). At the lamellopodium, which forms at the leading edge of a migrating cell, a branched and crosslinked actin network pushes the cell membrane outwards by polymerizing against it [65]. Here, other passive crosslinkers like the Arp2/3 complex are involved in connecting individual AFs (Fig. 1.7b).

Actin filaments can also form larger linear bundles like SFs and filopodia. Here, one usually distinguishes between parallel structures (e.g. filopodia), where all the plus-ends

are directed towards the cell membrane to form finger-like protrusions, which are important for cell migration and cellular sensing, and anti-parallel bundles (e.g. SFs) that carry the ability to actively contract [64]. The contractile bundles can be categorized into SFs and transverse arcs. The former are linked to the cells surrounding environment by focal adhesions (FAs) [66] (then often termed ventral SFs) and can thereby exert forces on the order of 10 nN per FA (purple dots in Fig. 1.7) onto the substrate [67, 68]. Transverse arcs form parallel to the leading edge of a migrating cell, but are not connected to the ECM [69].

Contractile SFs contain myosin motors as force generating elements and individual filaments are linked by crosslinking proteins such as α -actinin (Fig. 1.7b). This makes them similar to the structure of muscle myofibrils, with which they share the internal organization consisting of periodic subunits (sarcomeres), although with less order than muscle cells [70]. To generate forces, each of these sarcomeres contracts by a small amount, in sum leading to macroscopic contraction of the whole fiber.

1.4.2. Microtubules

The second major component of the CSK are microtubules, which are stiff, tubular filaments with a diameter of 24 nm and a persistence length on the order of several millimeters [63]. MTs are generated by polymerization out of the protein tubulin, which was discovered 50 years ago [72, 73]. In the mid 1980s the molecular motors kinesin [74–76] and dynein [77, 78] were identified, which can walk along MTs. Most motors from the kinesin family target the plus-end and dyneins moves towards the minus-end (Fig. 1.8a).

Microtubules grow with dynamic instability and can alternate between a state of slow growth and rapid disassembly [79]. α -tubulin and β -tubulin form heterodimers that assemble into protofilaments, which in turn make up the microtubule (Fig. 1.8b). Both tubulin subunits contain GTP and after polymerization the GTP-molecule in β -tubulin eventually gets hydrolyzed to GDP, which weakens the bond between them, but still keeps β -tubulin enclosed inside the filament. As long as hydrolysis occurs far away from the growing plus-end of the MT, a GTP-cap ensures persistent growth. If however, the hydrolysis catches up to the plus-end, the weakened α -tubulin– β -tubulin bond will lead to rapid depolymerization of the MT (Fig. 1.8b). This process is often called a MT catastrophe. The GTP-cap can be regained and the MT is “rescued” from the catastrophe, which reinitializes growth [1].

MTs play an essential role in cellular division by forming the mitotic spindle that mechanically separates chromosomes with the help of kinesin motors (Fig. 1.8c,d). In the

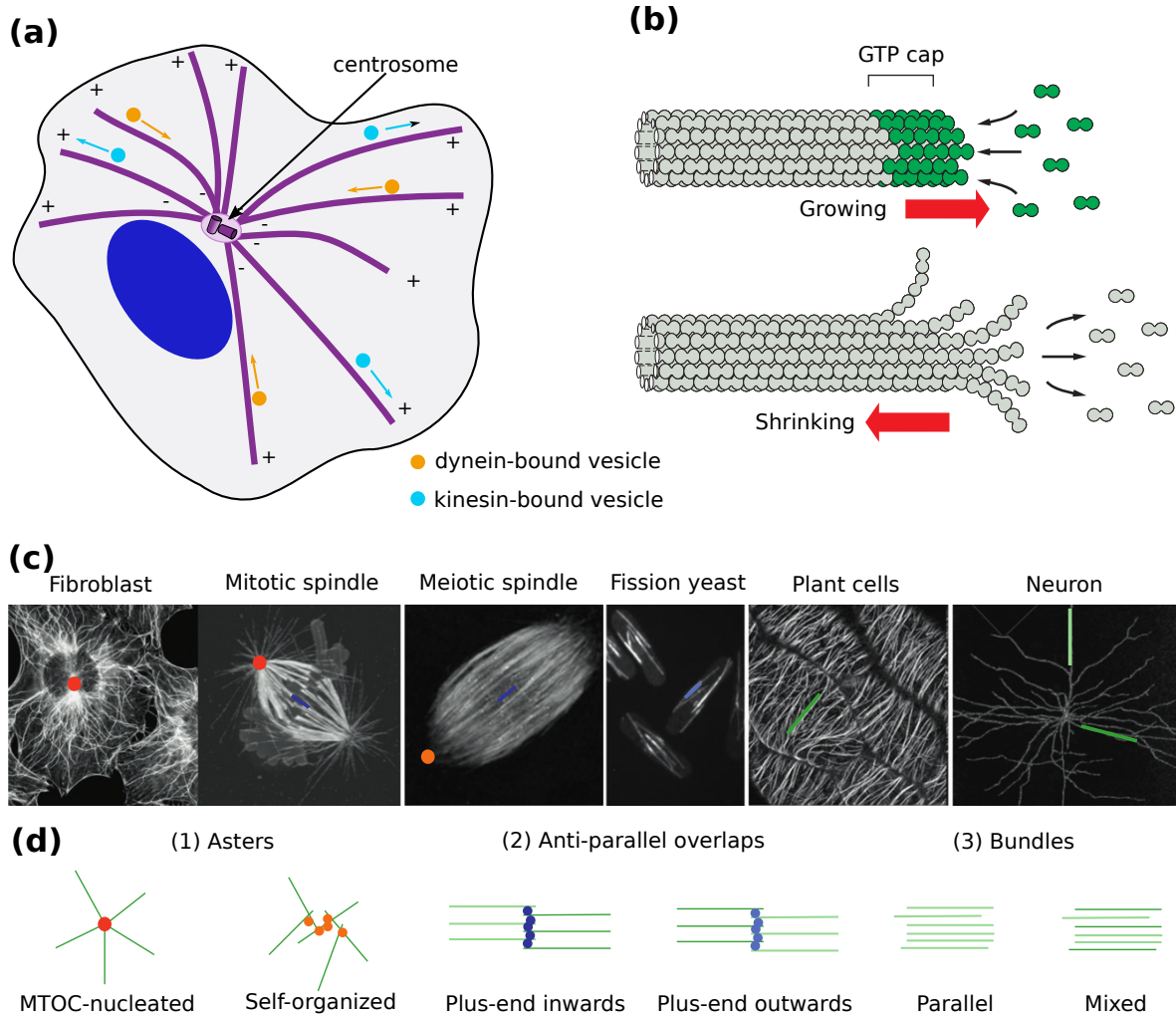


Figure 1.8.: (a) Typical layout of the MT CSK in a cell adhering to a planar substrate. MTs (purple) plus ends grow outwards from the centrosome, which acts as a microtubule organizing center (MTOC). MT network provides a frame of reference by locating the centrosome at the cell center. Transport of vesicles towards the cell membrane is mediated by plus-end targeting kinesin motors and transport to the perinuclear region by minus-end targeting dynein motors. (b) Microtubules grow by polymerizing from tubulin heterodimers in the GTP-bound state (green). Hydrolysis of GTP to GDP weakens the bond between the heterodimers, but MT remains intact as long as the GTP cap is sufficiently large. Kinesin and dynein motors are sketched, which transport vesicular cargo along the MTs. If hydrolysis catches up to the MT tip, rapid depolymerizing occurs. Figure modified from [1]. (c), (d) Alternative arrangements of MTs for different functions or in different cell types. Figure taken from [71].

newly formed daughter cells the MT network positions the centrosome, which acts as a microtubule organizing center (MTOC) and provides a point of reference for intracellular organization (Fig. 1.8a) [80, 81]. MTs also serve as tracks in which intracellular

vesicles are transported from the cell periphery to the cell center and vice versa. One prominent example is the reformation of the Golgi complex after cell division, during which it is split into multiple smaller vesicles and dispersed throughout the cytoplasm. After mitosis, when the centered microtubule network has reformed, the Golgi vesicles are transported towards the nucleus by dynein motors, where they are assembled again into the larger Golgi complex [82].

Another important process where MTs are involved is the regulation of focal contacts and cell adhesion [83]. By transport of the APC protein towards the plus end, seeding of new focal contacts at the cells leading edge can be induced and there is evidence that certain MT binding guanine nucleotide exchange factors (GEFs) are involved in the modulation of acto-myosin activity [84] via the Rho pathway (see Section 1.4.5). MTs have also been shown to dissociate FAs [85] and also to be stabilized by FAs [86].

Mature FAs with actin SFs attached to them can be targeted by growing MTs that are guided along the SFs by CSK crosslinking proteins. Once FAs are reached, MTs can be stabilized by so called and thereby transport pathways targeting FAs can be established [84].

MTs do not only serve as tracks for intracellular transport, but they also play a role in CSK mechanics. In neurons for example, microtubules reinforce axons, dendrites and synapses. In axons they are organized as short filaments in a parallel fashion, with the plus-ends pointing towards the axon tip (Fig. 1.8c,d). During axonal growth, there is important interplay between actin and MTs, as a contractile actin cap bundles advancing MTs, which leads to enhanced mechanical stability and the ability to follow guidance cues. Once the actin cap is lost, the MT bundle splays and the growth cone branches, enabling it to explore a larger region [87]. The current model for the formation of synapses is, that MTs curl and form loops, creating blebs and inflating presynaptic terminals [87].

Neurons are the cell type where MTs have the most dramatic influence on mechanical properties and development, but also in most other cells they are involved in the formation of membrane protrusions at the leading edge of migrating cells. It was found that the majority of MTs cannot pass through the densely crosslinked actin mesh at the lamellopodium [88], but individual MTs might advance into this area and facilitate the formation of protrusions due to mechanical interactions or by their transport and signaling properties [83].

MTs also represent the central mechanical component of cilia and flagella, which are hair-like appendages that enable for example sperm cells to swim or are found in the human respiratory tract, where they beat in a synchronous fashion to transport mucus or

bacteria out of the lungs [1].

1.4.3. Intermediate filaments

The third class of CSK fibers are intermediate filaments, which are rope-like polymers and form a heterogeneous group with variabilities in protein composition, function and occurrence. Mostly, IFs are associated with the physical strengthening of cells and tissues and are often found in cells which are subject to external stresses [1]. In contrast to AFs and MTs, they are not polarized and less dynamic. For this thesis intermediate filaments are only of secondary importance and will not be discussed in more detail. A comprehensive review on intermediate filaments is given [89].

1.4.4. Cytoskeletal crosstalk

In the last sections it has become evident that the various CSK components cannot be considered individually and, that there is substantial crosstalk between all constituents. *In vitro* experiments with a reconstituted actin CSK showed that such a network is able to deform MTs in the presence of myosin motors [90]. Similar observations have been made *in vivo*, where MTs showed bending predominantly on small length scales of $\approx 3\mu\text{m}$ and had an effective persistence length of $l_p \approx 30\mu\text{m}$ [91]. This is two orders of magnitude lower than the persistence length of $l_p \approx 5.2\text{ mm}$ observed *in vitro* [63], when only thermal fluctuations act on MTs. By depleting cells of ATP, and thereby inducing a strong decrease in the activity of myosin and other molecular motors, it was also shown that the bending is of nonthermal origin, because fluctuations were absent in the depleted cells [91].

In vivo, it is less clear where the interactions originate, but numerous crosslinkers and molecular motors have been identified that mediate interactions between CSK filaments (Fig. 1.9) [56].

Important for the interaction of MTs with other CSK components is the heterogeneous group of plus-end tracking proteins [92]. One example is EB1, which mediates interactions with the cell cortex and other compartments. EB1 can also be used to study the dynamics of MTs, because it is easy to tag with fluorescent markers [93].

Additionally, biological engineered crosslinking proteins have been shown to facilitate interactions between actin bundles and MTs [95] and could induce the alignment of large parts of MTs with actin bundles (zipping). Similar effects of MT guidance by AFs could be related to the action of molecular motors kinesin [96] and also myosin II, which

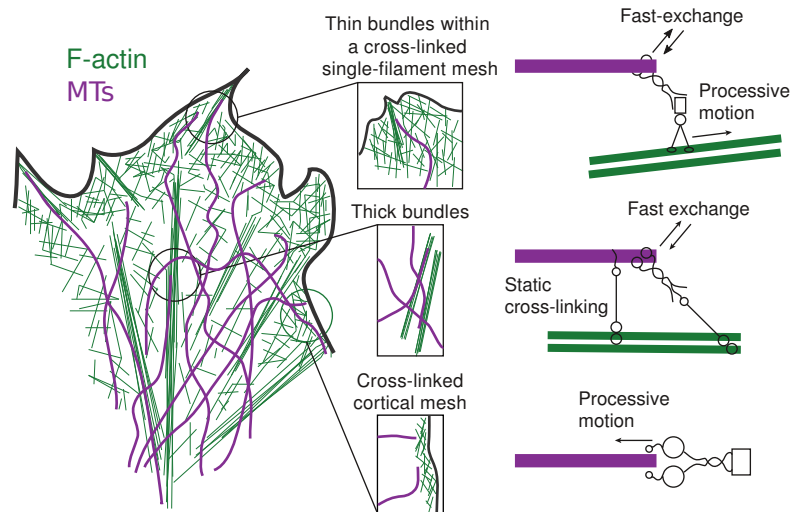


Figure 1.9.: Crosstalk between the actin CSK and MTs can occur for all AF sizes and is mediated by either dynamic molecular motors or static crosslinkers. Modified from [94].

influence the guidance of MTs by intracellular SFs [97].

The interaction between the actin CSK and the MT network is not unidirectional and the dynamics of both filament types is intertwined [98]. Recent research suggest that the centrosome [99] and microtubule plus-end can initiate actin polymerization [100].

1.4.5. Regulation of cellular contractility

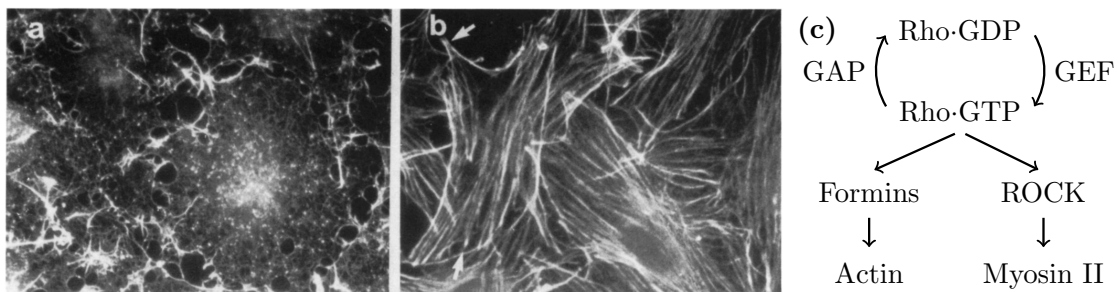


Figure 1.10.: (a) Micrograph of serum-starved Swiss 3T3 cells with fluorescent labeling of actin that display almost no SFs. (b) After injection of RhoA the formation of SFs sets in. (c) Pathway of Rho activation leading to cell contractility. Figures (a) and (b) from [101].

Polymerization dynamics of the actin CSK and the formation of SFs are closely linked to the GTP-binding protein RhoA as was shown in seminal work by Ridley and Hall [101, 102]. In those experiments, cells were serum-starved, i.e. cultured in a medium lacking typical growth factors, which resulted in cells with very few SFs and actin mainly

distributed as small filamentous structures (Fig. 1.10a). After injection of RhoA, the actin CSK underwent drastic remodeling and formation of SFs could be observed (Fig. 1.10b). New FAs were found to assemble by the addition of RhoA [101].

Nowadays, the pathway leading to this structural changes is well understood [103]. In mammalian cells about 20 Rho GTPases exist, which are not only important for the dynamics of the actin CSK, but also play a role in microtubule organization, intracellular vesicle trafficking and the regulation of the cell cycle [104]. Rho GTPases act as molecular switches and they can cycle between an active, GTP-bound state (Rho-GTP) and an inactive, GDP-bound state (Rho-GDP) [105]. During activation, Rho GTPases are recruited to the plasma membrane and the switching from an inactive to an active state is mediated by various GEFs, whereas the process of inactivation is governed by a family of GTPase-activating proteins (GAPs). Rho-GTP leads to downstream activation of Rho-associated kinase (ROCK) and formins. Thereby actin polymerization and the phosphorylation of the myosin light chain is induced, which then promotes myosin activity [106]. Those active acto-myosin complexes enable the formation of SFs and cell contraction (cf. Fig. 1.10c).

1.5. Cell adhesion and cell shape

Cells establish connections to the ECM mainly through the integrin family of transmembrane proteins. Initial small focal complexes that form underneath the lamellopodium of migrating cells can be linked to the actin CSK by various anchor proteins such as α -actinin, talin, filamin or vinculin (Fig. 1.11). It has been shown that there are some integrins whose bond lifetimes increase under force [107]. Such a catch-bond behavior can stabilize the connection between the actin CSK and the ECM and thereby focal complex can recruit additional integrins to mature into a FA. Focal adhesions have been shown to transmit force on the order of $5 \text{ nN}/\mu\text{m}^2 = 5 \text{ kPa}$ to the substrate [67, 68] and that they grow under external forces [108]. By such mechanisms, FAs enable the cell to sense its environment [109]. Various proteins, such as formins or zyxin, have been shown to contribute to force dependent actin polymerization and also translate extracellular cues to intracellular signals via the Rho pathway.

In mammalian cells, the family of integrin proteins consists of 24 distinct integrin dimers that are formed by α and β -subunits [110]. Integrins are not only involved in the formation of adhesions sites, but also control a range of other essential cellular processes, like proliferation, differentiation, migration and apoptosis. In contrast to most other trans-

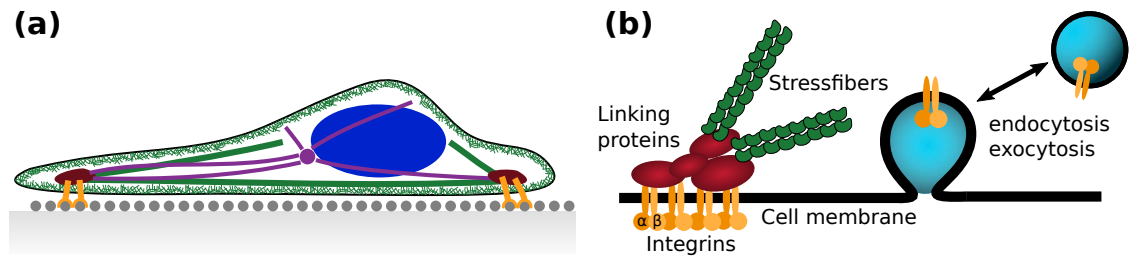


Figure 1.11.: (a) Shape and internal organization of a cell adhering to a planar substrate. Focal adhesions are formed by the family of integrin transmembrane proteins (orange) and various linking proteins (dark red) that connect them to SFs (green, bold). MTs (purple) can target FA by guidance along SFs by crosslinking proteins and molecular motors (pink). (b) Simplified structure of FAs. Integrins are formed by α and β -subunits. Integrins are not exclusively bound to the cell membrane, but can be internalized by endocytosis and transported throughout the cytoplasm inside vesicles or can be distributed at the membrane (exocytosis) for inside-out signaling.

membrane proteins, integrins function as bidirectional signaling molecules that link the extracellular to the intracellular environment and vice versa (outside-in and inside-out signaling) [111]. The process of FA formation is an example of an outside-in signal, but also the reverse process of inside-out signaling plays a role in a number of cellular processes. The adhesion of leukocytes (white blood cells) to sites of inflammation, for example, is controlled by surface bound integrins that can be activated if chemoattractants are sensed. This enables the leukocyte to firmly adhere to sites of inflammation [112].

Integrins are not only linked to inflammatory responses, but also play a role in a number of diseases, such as thrombosis and cancer. A highly important aspect for the progression of cancer is the ability of cells to migrate through tissue and form metastasis [113]. Here, integrins play a major role in the invasion of cells from a primary tumor to neighboring tissue or the blood stream, e.g. by the the formation of invasive pseudopods that penetrate dense tissue and can initiate cell migration [114, 115].

1.6. Models for cell shape

In this section we discuss the shape of adherent cells and will mention experimental results in conjunction with theoretical models.

Adhesive cells show invaginations of their membrane between sites of adhesion [116] and a decrease in the concentration of polymerized actin increases these invaginations [117]. Even stronger inhibition of the actin cortex leads to the formation of tubular protrusions that resemble a shape like a chain of pearls [117]. This pearling effect is a result

of the Plateau–Rayleigh instability of tubes under tension [118]. Such observations can be explained by a model in which a line tension γ between adhesion sites balances a surface tension σ of the membrane [117]. Following the Laplace law, this force balance can be expressed as [21, 117]

$$\sigma \mathbf{v} = \lambda \frac{d\boldsymbol{\tau}}{d\xi} = \frac{\lambda}{R} \mathbf{v}, \quad (1.8)$$

with the surface normal \mathbf{v} , the surface tangent $\boldsymbol{\tau}$, the contour coordinate ξ and the radius of curvature R , which leads to $R = \lambda/\sigma$ (Fig. 1.12b).

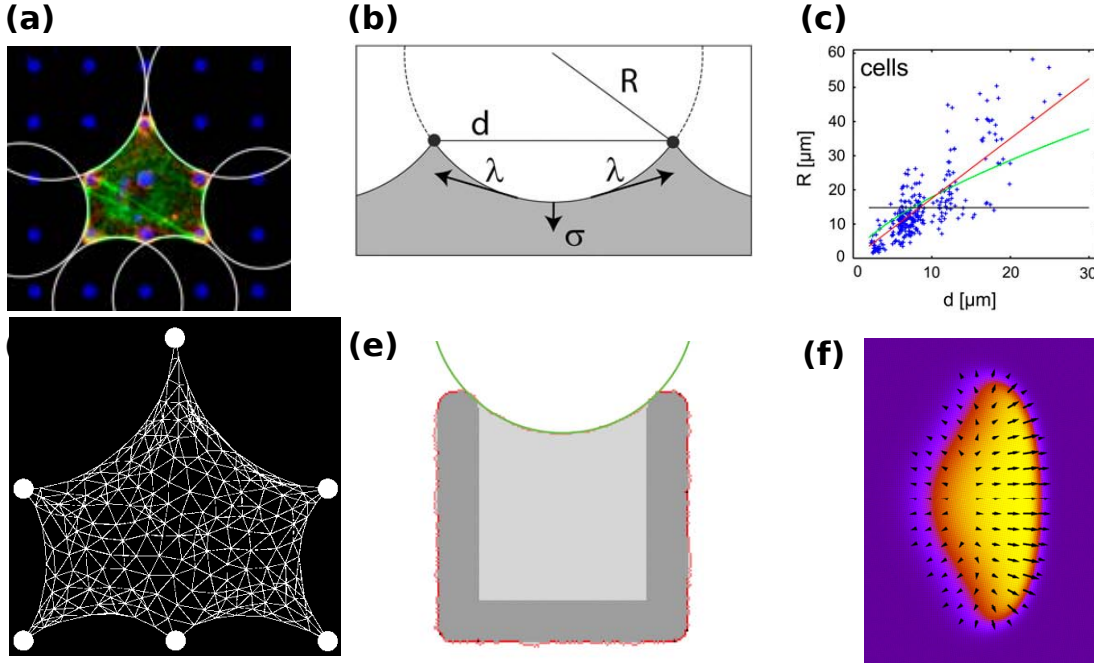


Figure 1.12.: (a) Cell on microdot pattern shows invaginated circular arcs between adhesion sites. (b) Definition of spanning distance d and arc radius R of inward-curved circular arcs. Simple tension model based on a Laplace law with line tension λ and surface tension σ . (c) Fits of the tension-elasticity model to experimental data. (d) Disordered cable network yields same shape as the tension-elasticity model. (a)-(d) modified from [21]. (e) Cellular Potts model for cell shape and dynamics on MP substrates. From [119]. (f) Phase field model for migrating keratocytes. From [120].

Théry et al. [22] noted that SFs between adhesions show an increase in the radius of curvature, caused by an increased contractility of the fibers during reinforcement. Bischofs et al. [21] investigated circular arcs formed by cells adhering to a microdotted substrate (Fig. 1.12a) and found that for larger spanning distances radii of curvature were higher. This contradicts Eq. (1.8), which predicts a constant radius, but can be explained by the tension-elasticity model, in which a modified line tension is introduced according to linear

elasticity theory:

$$\lambda = EA \frac{L - L_0}{L_0}. \quad (1.9)$$

EA is the rigidity of the contour, $\frac{L-L_0}{L_0}$ the relative deformation with arc length L and resting length L_0 . By this modification an implicit equation for the radius of curvature can be derived, which is a monotonously increasing function of the spanning distance

$$R = l_f \left(\frac{2R}{\alpha d} \arcsin \left(\frac{d}{2R} \right) - 1 \right). \quad (1.10)$$

$l_f = EA/\sigma$ is a length scale defined by the ratio of rigidity to surface tension and $\alpha = L_0/d$ is a rest-length parameter. This model is able to quantitatively explain the experimental findings of increasing radius of curvature for increasing spanning distance (Fig. 1.12c) [21].

The effects described above can also be explained by models based on contractile cable networks, that were studied in 2D [21, 121] and in 3D [122] (Fig. 1.12d).

Another class of models that can predict cell shape are cellular Potts models (CPM). Here, a binary variable is defined on a lattice and its state defines if the lattice site belongs to a cell or to the background. This definition makes CPMs comparable to the classic Ising model. To simulate the shape of adherent cells, a suitable Hamiltonian has to be defined that incorporates surface tension, line tension, as well as adhesion and cell spreading [123] (Fig. 1.12e). Such models can also be extended to study cell migration and tissue dynamics [119].

Recently, phase field models have been proposed for cell shape [124]. Such models define cell shape implicitly as the isocontour $\Phi = 1/2$ of an abstract phase field Φ that ranges between 0 and 1 (Fig. 1.12f). The dynamics of the phase field is coupled to other fields, such as the polarization field of the actin CSK to study the shape of migrating cells [120] or collective cell migration [125].

1.7. Outline of the thesis

In this thesis we connect quantitative image analysis of cell shape and internal organization with computational modeling. The unifying element for the various aspects of cellular architecture we investigate are micropatterned substrates that normalize cellular behavior.

The thesis is divided into two parts. In **Chapter 2** we start by introducing techniques

and algorithms for image processing, which will be applied to experimental data in the following chapters. Those techniques include segmentation of the relevant parts of an image from the background, detection of circular arcs at the cell boundary, measuring the local orientation of features in the image and ways to estimate motion in a sequence of images.

In **Chapter 3** we apply the aforementioned techniques to study the actin CSK of cells on MP substrates. By automatically detect peripheral circular actin arcs in cells adhering to a 2D MP substrate, we measure the important parameters radius of curvature and spanning distance. We relate the extracted parameters to the tension-elasticity model, which predicts an increasing radius with increasing spanning distance, and obtain very good agreement between both. Furthermore, we extend the analysis of circular arcs to three dimensions and study cell shape in 3D microscaffolds. Here, the measured parameters will be compared to a computational model based on contractile cable networks. To gain a deeper understanding in the microstructure of SFs we demonstrate a method to accurately determine the position of the force generating myosin II minifilaments in the SFs and give an outlook how this can be utilized for future modeling and experimental work.

In **Chapter 4** we analyze the contraction dynamics of the actin CSK under external stimulation, which can be induced by optogenetics. We apply an optical flow technique to extract flow fields of the CSK from timelapse recordings and quantify how SFs contribute to the contraction dynamics.

In **Chapter 5** we continue our analysis of the structure of the CSK by measuring the orientation field of the MT network in cells on MP substrates. We show that the MT network is organized differently in the vicinity of SFs that freely span between adhesion sites, compared to regions where the cell spreads over adhesive parts of the substrate.

In **Chapter 6** we temporarily move away from the study of the CSK and present a method to quantify changes in the intracellular accumulation of integrin, depending on a knockdown of gene expression by RNAi. We utilize the normalization of cell shape by MP substrates to extract the spatial distribution of intracellular integrin. The influence of RNAi will be assessed with the help of statistical tests.

The second part of the thesis focuses on modeling of the organization of the MT network in cells with predefined shape. In **Chapter 7** we discuss the model assumptions based on the former analysis of the MT network and give an overview of mathematical models for the CSK.

In **Chapter 8** we study the organization MT network by modeling it as a collection of growing polymers. We simulate the growth of polymers by a persistent random walk

or the with Brownian dynamics and predict the orientation of the MT network in cells whose shape is determined by MP substrates. With this approach we can explain our earlier experimental results and predict the layout of the MT network in cells for any given shape.

In **Chapter 9** we present an alternative way to model the MT network. We develop an effective continuum description based on the theory of liquid crystals and motivate boundary conditions according to the former analysis of experimental data. With such an approach we can directly predict the MT orientation field for cells on MP substrates and show that this and the previous models yield very similar results.

Chapter 10 summarizes and concludes the thesis.

Part I.

Image Analysis

Image processing techniques

Image processing is the general task of applying mathematical operations to images, while image analysis aims at the extraction of quantitative information. Image analysis is one of the key components in the workflow of obtaining quantitative knowledge about biological systems. It links the technical field of imaging, which is influenced by advances in physics, chemistry and biology, to more high-level fields, such as theoretical biophysics, bioinformatics or systems biology. While the latter aim to model, classify or interpret data, image analysis is responsible for providing quantitative information about the systems under study. Of course, the aforementioned scenario is only one example where image analysis provides such a link. Other fields are optical remote sensing, materials testing, medical scenarios, and many more. Image processing and analysis plays a large role in the field of computer vision, where tasks for image understanding are executed by computers.

In this chapter we will give an overview of the analysis methods relevant the remainder of this thesis. Those techniques were developed and implemented with the aim to extract quantitative information for a clearly defined research question. Nevertheless, such methods can be generalized and applied to other fields of research if similar information needs to be extracted. One could classify the techniques discussed in the following as classic techniques, in the sense that they were designed to extract one or more specific features out of image data and are static, i.e. they will perform the task they were designed for, but need to be adapted for other tasks.

Modern image analysis often involves, to more or less extend, the concept of machine learning. Here, training data, which can be taken from existing databases or provided by expert users, is provided to an algorithm. This algorithm then performs tasks such as categorizing data or recognizing features. One example for such an approach is the soft-

ware ilastik [126], in which a user provides annotations for different classes present in an image and an algorithm generalizes the annotations and classifies features in previously unseen images. Another example from clinical applications is the use of deep convolutional neural networks [127] for automated detection of cancer in biopsy specimen to aid pathologists [128]. The contrast between the two approaches is that in the former the user has to provide annotations and selects image features and the algorithm then determines their relative importance, while in the latter also the features will be generated by a neural network.

Although machine learning algorithms are very powerful, they are dependent on the availability of enough and suitable training data. In biophysical research one is often confronted with difficult experiments leading to little available data and more complex questions than simple yes-no-classification. For such data it is often already a hard task to provide meaningful annotations and therefore classic image analysis methods, tailored to the specific research question, are a suitable way to extract the desired information.

Image processing is usually performed in a sequential process starting from image formation over image enhancement, e.g. calibration, registration or transformation, to image analysis, where feature extraction, segmentation and classification takes place [129]. Also in various applications of image analysis discussed in this thesis, the same steps are necessary and in the following sections we will discuss the methods used in more detail.

2.1. Image registration

When spatial information about structures should be extracted from multiple images, it is necessary to find a common reference coordinate system. One way of finding such a coordinate system is image registration, where individual images are aligned to a reference image. In clinical applications, registration tasks often involve, for example, the alignment of data obtained from different imaging techniques such as magnetic resonance imaging (MRI) or computed tomography (CT) or recordings taken over a longer period to visualize the progression of a disease [130].

Compared to the task of aligning volumetric data obtained by different imaging techniques, as mentioned above, the processing 2D micrographs is simpler. Micropatterned substrates facilitate this task even more, because an adhesive micropattern can be used as a reference to align multiple fluorescent images. Furthermore, we expect only translational and rotational mismatches between different images and no distortions that might occur in volumetric data.

In practice, the task of registration is performed by finding a transformation between the images by optimizing a cost function that measures the similarity of an image and a reference [131].

For our purpose we used open source algorithms from the Insight Segmentation and Registration Toolkit (ITK) [132]. Mattes mutual information [133] was used as a measure for image similarity and we chose a regular step gradient descent as suggested by several application examples given in the ITK documentation [134]. To avoid local minima in the optimization process usually an iterative scheme is applied where downscaled versions of the images are registered first and then the overlap is refined further.

It turned out that Gaussian smoothing of the binary reference image is beneficial for robust registration, because the sharp edges of non-smoothed image might lead to local minima during the optimization process. Additionally, median filtering of the test images was applied, because the micrographs often show bright spots in the micropattern images, which might lead to misalignments.

Instead of directly implementing the registration with ITK in C++, there are alternatives aiming for greater user-friendliness such as the command line driven software elastix [49, 135] that is accompanied by SimpleElastix [136] to provide bindings to commonly used scripting languages such as Python.

2.2. Segmentation

Often, the next step after image enhancement is the segmentation of important parts of the image (foreground) from unimportant parts (background). In natural images this task is often very difficult, e.g. segmenting a tiger from a dense vegetation background. For most of the images used in this thesis, the segmentation task is simpler, because usual micrographs of cells contain a homogeneous (often dark) background and bright, fluorescently-labeled structures. In such images the segmentation between foreground and background can be performed by choosing a suitable intensity threshold θ and classifying an intensity image $I(\mathbf{x})$ into a binary image $B(\mathbf{x})$, where \mathbf{x} symbolizes discrete sites of the underlying grid.

$$B(\mathbf{x}) = \begin{cases} 0 & I(\mathbf{x}) < \theta \\ 1 & I(\mathbf{x}) \geq \theta. \end{cases} \quad (2.1)$$

A suitable θ for intensity based thresholding can be estimated, for example from the global histogram of intensity values or from histograms in a local neighborhood, which is

beneficial if the background is non-homogeneous. A commonly used technique for determining θ is Otsu's method, in which the histogram is split into two classes by maximizing the inter-class variance of the two clusters [137]. We found that a histogram-based k-means clustering [138] is better suited for the segmentation of cells on micropatterned substrates. This method can be understood as a quantization of an image with many brightness values, i.e. 256 for 8-bit images or up to 65536 for 16-bit images, into an image with only k intensity levels. The algorithm is inspired by [139] and works as follows. For an image histogram H , with N bins defined by the number of pixels h_n belonging to bin n ,

1. Initiate k cluster centers μ^0
2. Assign histogram each histogram value h_n to one cluster c_i :

$$c_i = \{h_n : ||h_n - \mu_i||^2 \leq ||h_n - \mu_j||^2, \forall n, 0 \leq n < N, \forall j, 0 \leq j < k\}$$

3. Compute new cluster centers:

$$\mu_i^{t+1} = \frac{\sum_{h_n \in c_i} h_n \frac{n}{N} I_{\max}}{\sum_{h_n \in c_i} h_n},$$

where I_{\max} is the maximum intensity value of the image.

4. Repeat until μ_i do not change any more.
5. Define quantization thresholds:

$$q_{l+1} = \frac{\mu_{l+1} - \mu_l}{2}, \forall j, 0 \leq k,$$

with $q_0 = 0, q_{k+1} = I_{\max}$.

6. Quantize image according to:

$$I_q(\mathbf{x}) = j \quad \text{if} \quad q_j < I(\mathbf{x}) \leq q_{j+1}, \forall j, 0 \leq j < k.$$

With such a quantized image, we can still not determine background and foreground directly, but it turned out that for most usage cases with values of $6 \leq k \leq 8$, the quantization level I_0 corresponds to the background to be estimated (Fig. 2.1). For cells on micropatterned substrates, usually a reference shape is available that can be obtained by

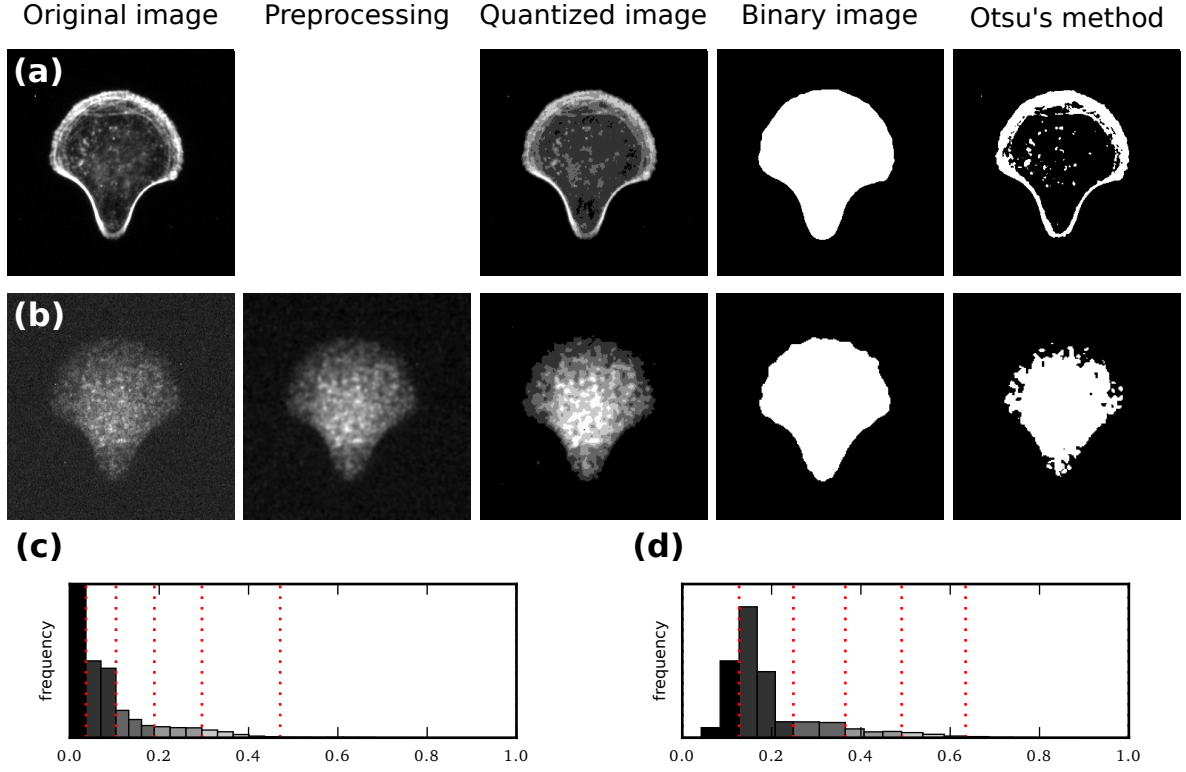


Figure 2.1.: k-means segmentation applied to two images of cells on a ∇ -shaped micropattern. **(a)** Image with good signal to noise ratio can be quantized and binarized without preprocessing. Binary image is shown with postprocessing consisting of filling of holes and removal of small objects. Otsu's method is shown for comparison and could be improved by postprocessing steps to yield the same result. **(b)** Image with lower contrast can be segmented robustly by applying a preprocessing step (here: Gaussian smoothing) and k-means segmentation. Otsu's method yields worse estimation of the cell and can only marginally improved by postprocessing. **(c)** Corresponding histogram of (a) with quantization levels indicated by red lines. **(d)** Same as above, for image (b).

averaging over a stack of images, to obtain an averaged image with a high signal to noise ratio, and segmenting this image. By utilizing this reference shape, or more precisely its area, the threshold θ_q of the quantized image can be chosen, such that the segmented image closely matches the reference image. For low values of $k \approx 6$ to 8 the area difference of I_q at the various quantization levels large enough to make this method robust.

Preprocessing steps, such as median filtering or Gaussian smoothing, can increase the performance of the segmentation procedure as well as postprocessing steps, like filling of holes in the binary image or removing too small objects from the segmented image B (Fig. 2.1).

2.3. Automated detection of circular arcs

The detection of shapes and curves is one of the most fundamental tasks in image analysis and is usually a follow-up on segmentation of image background and foreground. One of the earliest techniques to find curves in images is the Hough transform that was developed in 1962 by Paul Hough in order to detect straight lines [140]. Numerous refinements of this technique were proposed over the following decades with improvements like the detection of ellipses [141] or a generalization to arbitrary shapes [142, 143].

The basic idea of Hough was to transform spatially extended objects in image space into more compact objects in a parameter space, so that the recognition task can be simplified to a peak detection task in parameter space [144]. For the detection of lines one possible parameter space can be defined by slope m and interception c with the corresponding transform f [144]

$$f((m, c), (x, y)) = y - mx - c = 0 . \quad (2.2)$$

By this, a straight line in image space is transformed into a family of straight lines in parameter space which intersect at one specific point that defines the slope and intersection of the original line. The lines in parameter space can be discretized on a grid and for each grid site the number of lines that pass through this site are collected into an accumulator array. Parameter estimation of the line in image space then translates to finding maxima in the accumulator array. The basic idea of applying a transformation from image space to parameter space can also be extended to other parametric curves or it can be used to match templates by using a parameter space given by rotation, translation and scaling [142].

The classic Hough transform has some shortcomings like large memory requirements, rather high computational time and difficult peak detection in the parameter space, especially for curves with many parameters [143]. Although memory usage and runtime are no serious challenges for modern computers, alternative implementations of Hough's classic idea are possible. One of them is the randomized Hough transform (RHT) [145], in which n random points of an edge are selected and then a system of linear equations is solved to estimate the parameters. If no linear scheme can be defined, least squares fitting of a larger sample size can provide an estimate of the parameters [143]. Votes for parameter values are again accumulated until a certain level is reached and this votes can then be used to find the corresponding curve in image space.

For later applications to the analysis of the CSK in Section 3.1, we are interested in the automated detection of circular arcs and mainly follow the algorithm of the RHT,

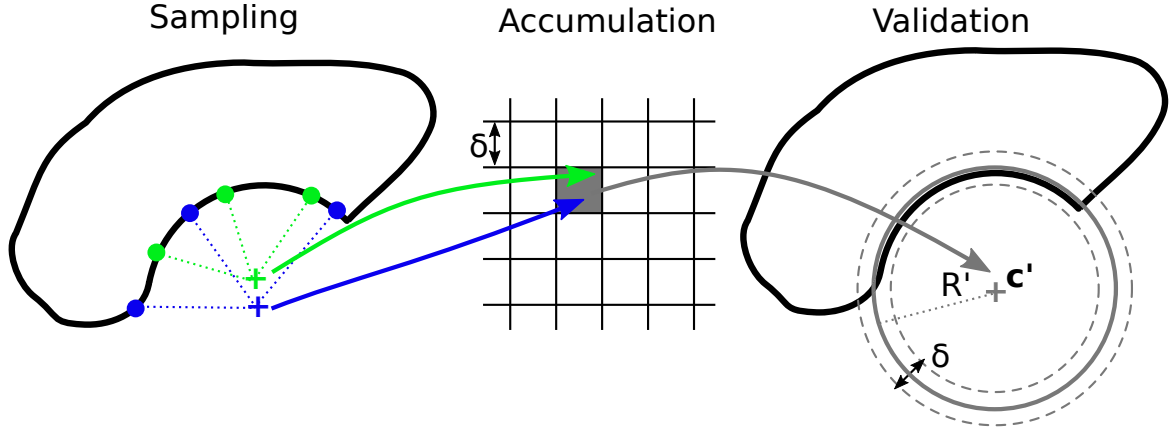


Figure 2.2.: Procedure of circular arc detection by the randomized Hough transform. Triples of points are sampled from an edge image (green, blue) and parameter votes are collected in an accumulator array. If enough votes are accumulated, the edge images is checked, if the votes belong to a circular arc.

outlined in [145]. Three points are sampled randomly from the edge of a segmented object to determine the center and the radius of a circular arc. For every point (x_i, y_i) the following equation holds:

$$(x_i - c_x)^2 + (y_i - c_y)^2 = R^2, \quad (2.3)$$

with $\mathbf{c} = (c_x, c_y)$ the center of the circle and R its radius. As the radius is unknown, one can set up the following system of equations:

$$(x_1 - c_x)^2 + (y_1 - c_y)^2 = (x_2 - c_x)^2 + (y_2 - c_y)^2 \quad (2.4)$$

$$(x_2 - c_x)^2 + (y_2 - c_y)^2 = (x_3 - c_x)^2 + (y_3 - c_y)^2, \quad (2.5)$$

which can be rewritten in matrix form $\mathbf{Ac} = \mathbf{b}$ as

$$\begin{pmatrix} x_2 - x_1 & y_2 - y_1 \\ x_3 - x_2 & y_3 - y_2 \end{pmatrix} \begin{pmatrix} c_x \\ c_y \end{pmatrix} = \frac{1}{2} \begin{pmatrix} y_2^2 - y_1^2 + x_2^2 - x_1^2 \\ y_3^2 - y_2^2 + x_3^2 - x_2^2 \end{pmatrix}. \quad (2.6)$$

Solving this linear systems of according to $\mathbf{c} = \mathbf{A}^{-1}\mathbf{b}$ for $\det \mathbf{A} \neq 0$ then yields the circle center. The corresponding radius R can be calculated according to

$$R = \sqrt{(c_x - x_1)^2 + (c_y - y_1)^2}. \quad (2.7)$$

For each three points sampled from the objects edge, one vote in the three-dimensional

accumulator array is collected (Fig. 2.2). The accumulator array is discretized into bins of size δ and the estimated parameters are collected into these bins. A trade-off has to be made for the choice of δ between the accuracy of parameter estimation and sparseness of the accumulator array. If δ is chosen too small, only very few votes will be accumulated in each bin and the detection procedure might fail, because no bin has enough votes to be considered as a robust detection.

Random sampling of points and vote accumulation continues until a predefined threshold of votes is reached. From the estimated parameters, a check is performed in the original image to check if the estimate corresponds to a real arc in the edge image. Edge pixels inside a ring with the estimated center \mathbf{c}' and radius $R' - \delta \leq R \leq r' + \delta$ are counted. If a long enough arc is detected, pixels are removed from the edge image, parameters are saved and a new detection loop is started.

2.4. Estimation of local orientation

For some application the detection of individual objects is not necessary and alternative approaches can be pursued to extract information about the structures present in an image. One of such approaches is to calculate the local orientation of structures in the image by a gradient-based approach using the structure tensor. Alternative approaches for orientation detection are steerable filters [146] or the software FilamentSensor [147] that first detects fibers and then analyzes their orientation. For an overview of alternative methods see [148].

2.4.1. Structure tensor

The following derivation of the structure tensor and its properties follows the one outlined in [149]. Let the local orientation be given by a unit vector $\hat{\mathbf{n}}$, perpendicular to lines of constant gray value. To find $\hat{\mathbf{n}}$ within a local neighborhood in the image, one tries to minimize the deviations of $\hat{\mathbf{n}}$ and the image gradient ∇I that can be achieved by maximizing

$$(\nabla I^T \cdot \hat{\mathbf{n}})^2. \quad (2.8)$$

The corresponding integral to be maximized in the 2-dimensional neighborhood is then

$$\int w(\mathbf{x} - \mathbf{x}') (\nabla I(x')^T \cdot \hat{\mathbf{n}})^2 d^2 x', \quad (2.9)$$

with a suitable windowing function w that is usually chosen to be a Gaussian function. Eq. (2.9) can be written as

$$\hat{\mathbf{n}}^T \mathbf{J} \hat{\mathbf{n}} \rightarrow \text{maximum} \quad (2.10)$$

and the components of \mathbf{J} can be expressed as a convolution of the windowing function w with a product of the image gradients:

$$J_{ij} = \int_{-\infty}^{\infty} w(\mathbf{x} - \mathbf{x}') \left(\frac{\partial I(\mathbf{x}')}{\partial x_i} \frac{\partial I(\mathbf{x}')}{\partial x_j} \right) d^2 x' . \quad (2.11)$$

The tensor \mathbf{J} is symmetric and can be diagonalized by a suitable rotation of the coordinate system. Utilizing this, Eq. (2.10) can be rewritten as

$$\mathbf{J}' = (n'_1, n'_2) \begin{pmatrix} J'_{11} & 0 \\ 0 & J'_{22} \end{pmatrix} \begin{pmatrix} n'_1 \\ n'_2 \end{pmatrix} \rightarrow \text{maximum}. \quad (2.12)$$

Without loss of generality we can assume that $J'_{11} \geq J'_{22}$ and it becomes clear, that $\hat{\mathbf{n}}' = (1, 0)$ maximizes Eq. (2.12).

The maximization problem can now be solved by rotating \mathbf{J} into its principal axis coordinate system according to $\mathbf{J}' = \mathbf{R}^T \mathbf{J} \mathbf{R}$ with rotation matrix \mathbf{R} ,

$$\begin{pmatrix} J'_{11} & 0 \\ 0 & J'_{22} \end{pmatrix} = \begin{pmatrix} \cos \vartheta & -\sin \vartheta \\ \sin \vartheta & \cos \vartheta \end{pmatrix} \begin{pmatrix} J_{11} & J_{12} \\ J_{12} & J_{22} \end{pmatrix} \begin{pmatrix} \cos \vartheta & \sin \vartheta \\ -\sin \vartheta & \cos \vartheta \end{pmatrix}. \quad (2.13)$$

Solving this equation for the angle ϑ then yields

$$\vartheta = \frac{1}{2} \arctan \left(\frac{2J_{12}}{J_{22} - J_{11}} \right). \quad (2.14)$$

As in the initial assumptions, the unit-vector $\hat{\mathbf{n}} = (\cos \vartheta, \sin \vartheta)$ now lies perpendicular to lines of constant gray value and defines their orientation.

2.4.2. Coherency measure

We assumed that for the eigenvalues of \mathbf{J} , that $J'_{11} \geq J'_{22}$ and found $\hat{\mathbf{n}}$ as the direction of the strongest change in the intensity values. \mathbf{J} has an orthogonal system of principle axes and the orthogonal axis to $\hat{\mathbf{n}}$ is related to the eigenvalue J'_{11} . In principle, there are now multiple possibilities of how the eigenvalues could be related:

$$\begin{aligned}
 J'_{11} = J'_{22} = 0 & \quad \text{rank}(\mathbf{J})=0, \text{ local neighborhood is constant.} \\
 J'_{11} > 0, J'_{22} = 0 & \quad \text{rank}(\mathbf{J})=1, \text{ gray values change only in one direction.} \\
 J'_{11} > 0, J'_{22} > 0 & \quad \text{rank}(\mathbf{J})=2, \text{ gray values change along both principle axes.}
 \end{aligned}$$

The estimation of local orientation will most likely be performed for line-like features or objects with strong edges. If images are blurred due to optical imperfections of the imaging system, camera noise or if multiple objects overlap, one can assume, that the gray values will not only change in direction of $\hat{\mathbf{n}}$, but also orthogonal to it and $J'_{22} > 0$.

To measure how well the local orientation can be estimated in the local neighborhood, one can define a coherency measure c that allows to quantify the relations of the structure tensor eigenvalues mentioned above [149]:

$$c = \frac{J'_{11} - J'_{22}}{J'_{11} + J'_{22}} = \frac{\sqrt{(J_{22} - J_{11})^2 + 4J_{12}^2}}{J_{11} + J_{22}}. \quad (2.15)$$

This measure now is 0 if there is an isotropic change in the gray values and a local orientation cannot be defined. It reaches its maximum of 1 if the intensity changes only in one direction and the orientation is a perfect description of the local neighborhood. For gray value changes in both directions it will range between $0 < c < 1$ and allows to measure the quality of the local orientation estimation. For a very small denominator $J'_{11} + J'_{22} \ll 1$, usually a cutoff c_c is defined and $c = 0$.

2.4.3. Implementation

To calculate the structure tensor for various images, we used the Vision with Generic Algorithms (VIGRA) library [150, 151]. There, the structure tensor is implemented by using Gaussian derivative filters to calculate the gradients and a Gaussian window function to define the local neighborhood. There are other implementations of the structure tensor, such as the ImageJ plugin OrientationJ [148] or inside the Python library scikit-image [152].

As an image derivative usually increases the noise level, one approach is to apply a smoothing filter before convolution with the derivative filter. A Gaussian derivative uses the properties of the convolution operation, by applying the derivative of a Gaussian function to the image and combining both steps.

For the windowing function w also a Gaussian is chosen. For both, the derivative filter and the windowing function, the width of the Gaussian has to be defined and adjusted to the size of the structures to which the structure tensor should be applied. A common

approach is to define the width σ of the Gaussian derivative and set the width of the windowing function as 2σ .

The parameters used for practical application of the structure tensor will be given in the corresponding sections.

2.4.4. Circular statistics

To calculate moments from a distribution of angles or other periodic data, one has to apply circular statistics [153]. For our purposes we only need the circular mean and circular variance and we define the first trigonometric sample moment of the samples α_k as

$$\bar{m}_1 = \sum_{k=1}^N e^{i\alpha_k}. \quad (2.16)$$

The circular mean is then given by

$$\langle \alpha \rangle = \mu_c = \arg(\bar{m}_1) \quad (2.17)$$

and the circular variance reads

$$\sigma_c^2 = 1 - |\bar{m}_1|. \quad (2.18)$$

The variance ranges between 0 and 1 and gives information about the spread of the samples.

2.5. Motion estimation

So far, we only discussed methods to extract information out of static images. The dynamics of biological processes is often of great importance for understanding cellular functions and therefore, a method to estimate motion fields within image sequences will be discussed. In Chapter 4 this method will be applied to extract intracellular flows of the CSK. In biological context applications for motion detection lie in estimating the movement of tissue [154], plant growth [155] or tracking of cell nuclei in embryogenesis [156]. The general concept of motion estimation is used in many other areas, such as meteorology or engineering applications or computer vision tasks, like motion detection and interpolation in natural scenes, or video compression algorithms. Also the task of image registration discussed in Section 2.1 falls into the field of motion estimation and similar techniques as the ones discussed in the following could be applied, but often, sim-

pler alignment methods are sufficient, because the motion patterns are much simpler than the ones occurring in natural scenes.

One way of estimating motion is to find the optical flow (OF), which can be defined as "the distribution of apparent velocities of movement of brightness patterns" [157]. There are many approaches to determine OF and often different scientific communities use different terminology for similar principles. The most commonly used methods to determine OF are based on correlation measures or differential methods. For a general overview see [158, 159].

Correlation-based techniques are often applied for particle image velocimetry (PIV), which originates from the field of fluid mechanics and was originally intended for the visualization of flow fields by tracer particles embedded into a viscous medium [160]. Here, motion patterns are estimated from two images of a sequence by computing the cross-correlation between smaller interrogation windows of the images. The maximum correlation coefficient then yields the particle displacement between the frames. In the field of materials testing, correlation-based techniques are known as digital image correlation (DIC) or digital volume correlation (DVC), but the underlying principles are comparable [161]. For both application scenarios also gradient based algorithms can be used to establish the match between images.

While correlation-based techniques assume that signals in subsequent frames are highly correlated, an alternative assumption is that objects retain a constant brightness upon displacement [162]

$$I(x, y, t) = I(x + u, y + v, t + 1). \quad (2.19)$$

By linearizing Eq. (2.19) by a first order Taylor-expansion under the assumption that the flow is small, one obtains

$$I(x, y, t) = I(x, y, t) + u \frac{\partial I}{\partial x} + v \frac{\partial I}{\partial y} + \frac{\partial I}{\partial t}, \quad (2.20)$$

which then yields the OF constraint

$$u \frac{\partial I}{\partial x} + v \frac{\partial I}{\partial y} + \frac{\partial I}{\partial t} = 0. \quad (2.21)$$

An issue of the OF constraint is that it consists only of one equation for the two components of the velocity field and it is therefore an ill-posed problem. This is commonly referred to as the aperture problem. If only a small region of an image is observed, e.g. by looking through an aperture, and the region under observation does not show any texture

or brightness changes then motion of such a part of the image cannot be detected [162].

Methods to solve Eq. (2.21) rely on image gradients and two well known approaches rely either on the assumption that the OF is constant in a local neighborhood of a pixel and then solve the OF equation for patches of the image [163] or on global smoothness constraints and minimize a global energy function by variational techniques [157]. These classical techniques and more advanced versions are implemented in a usage-ready form in the OpenCV library [164].

Brox et al. [165] developed an OF method that tries to preserve spatial and temporal smoothness, which is in contrast to the vast majority of OF methods that only preserve spatial smoothness and therefore, might be better suited for biological application scenarios with a lot of noise present in subsequent images. In addition to the brightness constancy assumption (OF constraint) Brox et al. [165] introduced a gradient constancy assumption

$$\nabla I(x, y, t) = \nabla I(x + u, y + v, t + 1) \quad (2.22)$$

and combined it with a spatiotemporal smoothness assumption to set up an energy functional

$$E(u, v) = \int_{\Omega} \Psi \left((I(\mathbf{x} + \mathbf{w}) - I(\mathbf{x}))^2 \right) d\mathbf{x} + \gamma \int_{\Omega} \Psi \left(|\nabla I(\mathbf{x} + \mathbf{w}) - \nabla I(\mathbf{x})|^2 \right) d\mathbf{x} \quad (2.23)$$

$$+ \alpha \int_{\Omega} \Psi \left(|\nabla_3 u|^2 + |\nabla_3 v|^2 \right) d\mathbf{x}, \quad (2.24)$$

with $\Psi(s^2) = \sqrt{s^2 + \epsilon^2}$ a function enabling convex L^1 optimization, \mathbf{w} the vector of displacements and $\nabla_3 = (\partial_x, \partial_y, \partial_t)$ a spatiotemporal gradient. This formulation is a slight modification of the functional proposed by Brox et al. [165] who combined the first two terms into Ψ . By splitting the combined argument of Ψ into two integrals the functional becomes more robust in the sense that the brightness constancy or the gradient constancy terms can become zero independently of each other [166]. This approach was also employed by Sanchez, Monzon, and Salgado [167] who developed and published an implementation of the algorithm outlined above.

Analysis of the actin cytoskeleton using micropatterned environments

In this chapter we apply the aforementioned image analysis techniques to study the actin CSK. MP environments are used for cell culturing, which leads to a normalization of the cell shape and the internal organization. This facilitates image analysis and the quantification of the observations. We start by estimating parameters of peripheral SFs in a fully automated way for cells on 2D MP substrates. A similar analysis is performed for cells in 3D microscavolds. In both cases the parameters are fitted to mathematical models that predict cell shape. In the last section of this chapter, we analyze how myosin II minifilaments are distributed along SFs and give an outlook on how this information can be incorporated into future models.

3.1. Automated fitting of circular arcs

Bischofs et al. [21] performed a systematic curvature analysis of actin SFs, which spanned over nonadhesive regions of a MP substrate. They found a dependence of radius of curvature R on spanning distance d and could explain this with the tension-elasticity model (cf. Section 1.6). Their approach to image processing of fluorescent micrographs of the actin CSK was semi-automated and required the experimenter to manually select the adhesion points and some initial points along the actin arc. Precise estimation of the arc radius was then conducted automatically by performing a least squares fit to the maxima of radial intensity profiles.

This method of analysis has proven robust and suitable for the task of investigating circular actin arcs, but it requires substantial manual effort. With the advances in auto-

mated high-throughput screening and specific knockdown of genes by RNAi [18] and related methods, it is desirable to use image processing tools that perform analysis in an automated fashion in order to save manpower and financial resources.

In this section, we will combine the methods of automated circular arc detection introduced in Section 2.3 with a subsequent optimization step to fit circles arcs to actin SFs, visible in fluorescent micrographs. The images on which this analysis is based were recorded in the group of Vytaute Starkuviene-Erfle at BioQuant, Heidelberg University by Susanne Reusing and Gintare Garbenciute.

We apply our analysis procedure to fluorescent micrographs of HeLa cells, a human epithelial cell line. The actin CSK, the cell nucleus and the MP were fluorescently labeled (Fig. 3.1a). The cells were cultured on planar 2D substrates with ∇ -shaped and Y-shaped adhesive MPs. The characteristic invaginated actin bundles form at edges spanning non-adhesive regions of the substrate (Fig. 3.1a).

The cell is segmented from the background (Section 2.2) and its outline is calculated. We then apply the RHT (Section 2.3) to find circular arcs along the cell outline. These circular arcs correspond to SFs that are brighter than the surrounding actin CSK, due to their higher density in F-actin. To refine the initially estimated circular arcs, we use an intensity-based optimization process to align them with the SFs.

For this optimization process we need to fit circles to a set of points. One way of doing this is to calculate the perpendicular bisectors of all lines connecting points to which the circle should be fitted (Fig. 3.1b) [168]. The center of the circle is then placed at the point (c_x, c_y) , where the sum of distances to each of the perpendicular bisectors is minimal. We chose the modified least-squares (MLS) method from [168] and included the image intensity I as a weighting factor for the fitting procedure. The cost function to minimize then reads

$$f(c_x, c_y) = \sum_{i=1}^{n-1} \sum_{j=i+1}^n I_i I_j \left(X_{ij}^2 + Y_{ij}^2 \right) \left(c_x X_{ij} + c_y Y_{ij} - 0.5 \left(X_{ij}^{(2)} + Y_{ij}^{(2)} \right)^2 \right), \quad (3.1)$$

with $X_{ij} = x_i - x_j$ and $X_{ij}^{(2)} = x_i^2 - x_j^2$. The weighting of the intensity and the term $\left(X_{ij}^2 + Y_{ij}^2 \right)$ are different from [168, equation (6)] and ensure that bright pixels with a large pairwise distance are considered with a higher weight than in the original equation.

In a small band around the initial estimation of the circular arc by the RHT, we collect pixel coordinates and the corresponding intensities to optimize the arc in an iterative scheme. At each iteration, a new center of the arc is calculated by minimizing Eq. (3.1)

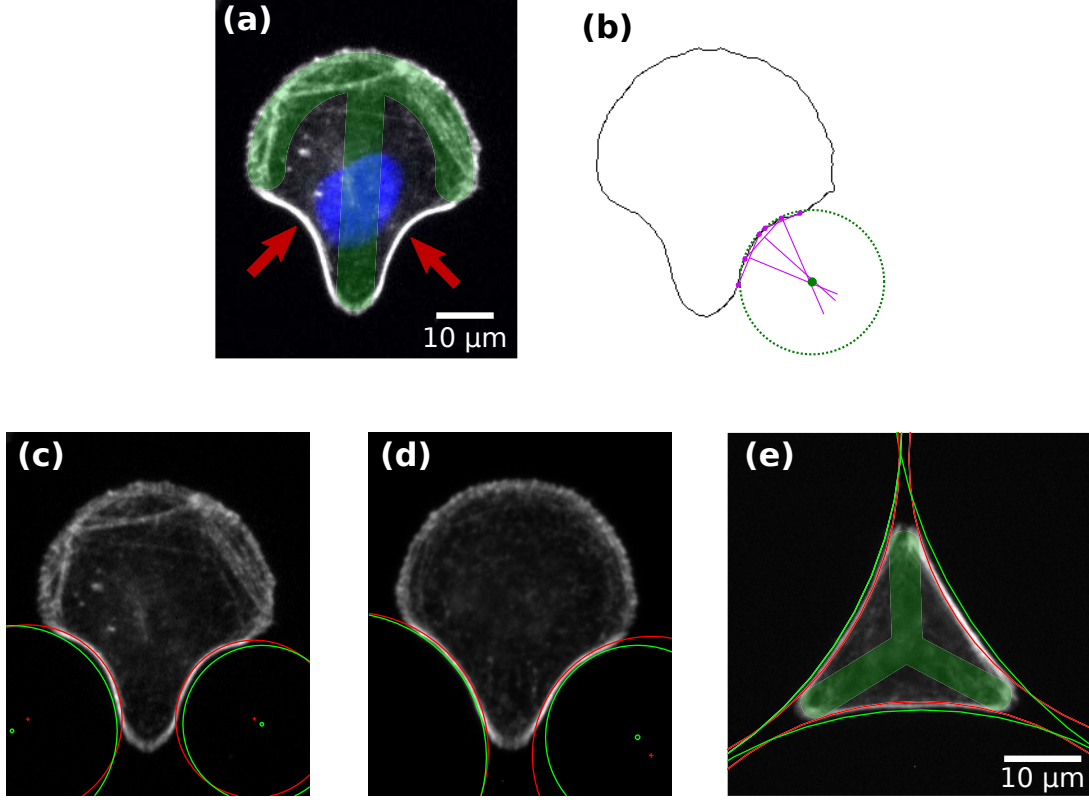


Figure 3.1.: Automated fitting of circles to invaginated actin arcs. **(a)** Micrograph of a cell on a ∇ -shaped MP with labeling of actin (grayscale), the MP (green) and the cell nucleus (blue). Invaginated SF form at the edges spanning nonadhesive parts of the substrate (red arrows). **(b)** Segmented cell outline with a fitted circle. Lines connecting points at the boundary and the corresponding perpendicular bisectors (violet) can be used to determine the circle center (see main text). **(c)** and **(d)** Samples of circles estimated by the RHT (green) and fitted circles after a further optimization step (red). **(e)** Circles fitted to a cell adhering to a Y-shaped MP.

and the corresponding radius is then given by

$$R = \frac{1}{\sum_{i=1}^n I_i} \sum_{i=1}^n I_i \sqrt{(x_i - c_x)^2 + (y_i - c_y)^2}. \quad (3.2)$$

Along this newly determined circular arc, pixel coordinates and intensities are collected within a narrow band and the minimization process is repeated.

By applying the RHT and the subsequent optimization step, circles can be fitted fully automated to all circular arcs (Fig. 3.1c-e).

The detection method outlined above relies on a robust estimation of the initial circle parameters by the randomized Hough transform (RHT). The postprocessing step, to fit

circles to the fluorescent images, yields a more precise estimation of the circle parameters and makes the procedure more robust to false-positives of the RHT. During the optimization process duplicate multiple detections of circles at the same actin arc are being merged onto the same parameter set (Fig. 3.2a).

If the arc approaches a straight line or the arc length becomes too small, i.e. the radius of curvature is much larger than the spanning distance, the automated detection by the RHT is not very reliable anymore. In this case the accumulator array contains too few votes for a given parameter set or the votes are spread out too far. This leads to false-negatives and an incomplete detection of all circular arcs in the image (Fig. 3.2b).

The Y-shaped MP shown in Fig. 3.2b provides a smaller adhesive area of only $\approx 75\%$ of the ∇ -MP area also and the cell nucleus covers a significantly larger fraction of the cell area ($\approx 33\%$) compared to the ∇ -shaped MP ($\approx 15\%$). This might limit the contraction of the SFs and could cause the large arc radii visible in Fig. 3.2b. When the aim is to investigate invaginated SFs, the MP size is usually chosen in such a way that the arcs are not straight lines, but show a visible curvature and the fitting method outlined above will provide robust results.

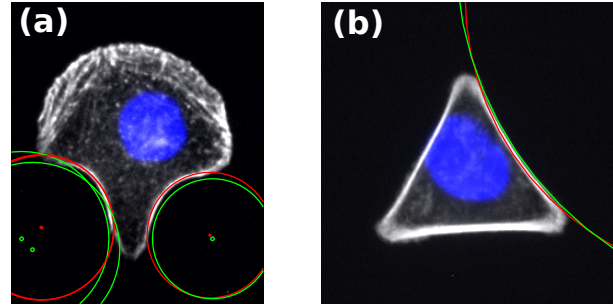


Figure 3.2.: (a) False-positives of the RHT (two green circles at bottom left) are being merged to the same parameter set (red) during optimization. (b) Short arc length leads to false-negatives of RHT and detection of only one arc.

3.1.1. Results

In Fig. 3.3, arc parameters extracted by the automated fitting method discussed above, are shown. The variability in spanning distance is due to slight variations in cell shape. We performed a least squares fit to the tension-elasticity model

$$R = l_f \left(\frac{2R}{\alpha d} \arcsin \left(\frac{d}{2R} \right) - 1 \right), \quad (3.3)$$

where we chose the rest-length parameter $\alpha = L_0/d = 1$. This means that a relaxed fiber represents the shortest connection between adhesion points. The parameter to be estimated is the length scale $l_f = EA/\sigma$, which defines the ratio between rigidity of the fibers and the surface tension. In Fig. 3.3 the corresponding fit with $l_f = 189.2 \mu\text{m}$ is shown. Compared to previously reported values of $l_f \approx 1 \text{ mm}$ [21], the fitted l_f for cells on the ∇ -shaped MP is lower, which points to weaker SFs in the cells we analyzed. Bischofs et al. [21] used fibroblasts that are known to form very strong SFs [169], while our analysis was done for epithelial HeLa cells, so this prediction is reasonable.

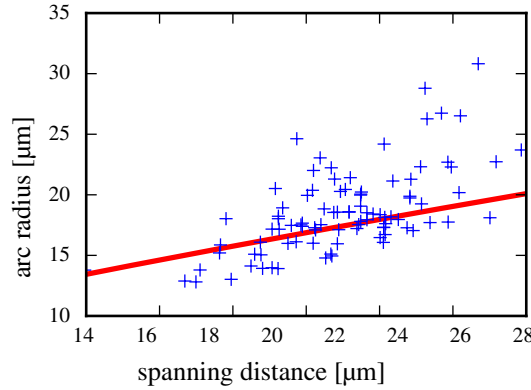


Figure 3.3.: Plot of arc radius vs. spanning distance for an analysis of HeLa cells adhering on a medium-sized ∇ -shaped MP. Red line is a fit to the tension-elasticity model.

3.1.2. Discussion

We presented a method to automatically detect invaginated circular arcs in two-dimensional images of fluorescently labeled cells. We used the RHT and included a post-processing step by fitting the detected circles to the fluorescent image. Our method is robust for typical arc lengths and radii of curvature found within cells on MP substrates. Here, it allows for fast analysis of large datasets to test the relationship of arc radius and spanning distance. Up to a certain extent the optimization method used for post processing can deal with false-positives, for example, by mapping multiple detections onto the same parameter set.

False negatives are more difficult to treat and missing arcs cannot easily be fitted in post processing. Here, possible improvements would be alternative circle detection methods that are also able to deal with short arc lengths and large radii of curvature. At this scales however, it is already a hard task for a human expert to distinguish circular arcs from

straight lines and automated procedures might fail as well.

Including prior information, like the number of circular arcs to be expected, might be an option to increase the robustness of the detection by the RHT. For simple MP substrates, where only one specific cell shape is possible, this would be an improvement. For MP networks or patterned substrates that allow for more diverse cell shapes this prior information would limit the flexibility of the RHT and might not be the best choice.

3.2. Analysis of circular arcs in 3D

Planar substrates are being extensively used for cell experiments and provide many advantages in terms of sample preparation and imaging. Restricting the cell to a 2D environment, however, might be a strong simplification, because the ECM often has a 3D structure, which leads to different behavior of cells cultured in 2D compared to 3D environments.

Fibroblasts, who live in connective tissue inside a fibrous 3D ECM, are a prime example of a cell type that shows differences in behavior depending on the ECM geometry. On a planar substrate fibroblasts assume a flat, strongly spread shape, which is comparable to a fried egg. They also form SFs throughout the cell, which contribute to force generation. In 3D, the situation is different and a more elongated phenotype is found, which shows lower numbers of SFs that are more peripherally located [169].

While there are numerous methods to fabricate 3D ECMs, as discussed in Section 1.2.2, also a variety of challenges exist that arise from the usage of such substrates. Just as in 2D, the shape of cells in 3D matrices will have a high variability and, e.g., the task of relating findings about cell mechanics from one cell to the next is difficult.

Similar to 2D MP techniques, 3D microscavolds can be fabricated to normalize cell shape by providing precisely defined adhesion sites. Such structures can be produced by direct laser writing [49].

Imaging of 3D structures poses greater challenges than in 2D, because the maximum achievable resolution along the z-direction is limited to approximately three times the resolution in the xy-direction. Here, SIM can be used to achieve resolutions below the diffraction limit of confocal microscopes and increase the axial resolution.

The design of suitable image processing workflows is also less straight forward than it would be with 2D substrates, because the third dimension adds considerable complexity in the segmentation of objects and detection of features such as lines or curved structures.

In this chapter we will discuss image analysis methods to extract circular arcs from

images of cells in 3D microscaffolds. Parameters of the arcs, such as radius and spanning distance, will be compared to a computational model based on a triangulated network of contractile cables [122].

The fabrication of the microscaffolds, cell culturing and imaging were performed by Benjamin Richter and Kai Weißenbruch from the group of Martin Bastmeyer, Karlsruhe Institute of Technology. The computational model was developed by Christoph Brand in the Schwarz group, Heidelberg University.

3.2.1. Cell shape in 3D microscaffolds

Before we discuss image analysis techniques for cells adhering in 3D geometries, we will give some examples for the microscaffolds used in the cell experiments.

To provide a stable adhesion geometry and to allow cells to extend into the z-direction, microscaffolds were created that consist of 4 to 5 pillars of identical height, which were arranged around a central pillar of lesser height (Fig. 3.4a). Thus, cells can adapt the shape of an inverted pyramid (Fig. 3.4b). In such structures, the spanning distance of free edges is limited to discrete values between adhesion sites in the xy-plane or between a site at one of the larger pillars and the central one. To allow for more variability in the spanning distances, asymmetric scaffolds can be used, in which one of the pillars is displaced (Fig. 3.4c). Variability in the spanning distances allows to investigate if the relation of increasing arc radius with increasing spanning distance, as predicted by the tension-elasticity model, still holds for cells in 3D geometries.

3T3 fibroblasts adhering in such pyramidal scaffolds still form peripheral SFs between adhesion sites, but internal SFs were less prominent and could only be observed rarely. Due to the lower central pillar, the cell shape is asymmetric w.r.t. the z-axis. Just as in 2D, SFs that form between adhesion sites bent inwards and have the shape of circular arcs. Due to the extension in z-direction of the adhesive cubes, mainly three characteristic orientations of the SFs could be observed:

- Arcs that lie in the xy-plane, parallel to the base of the scaffold and orthogonal to the pillars.
- Arcs that have anchoring points in the xy-plane, but lie in a plane that is tilted around the axis connecting the anchoring points.
- Arcs that span between the outer adhesion sites and the lower central pillar.

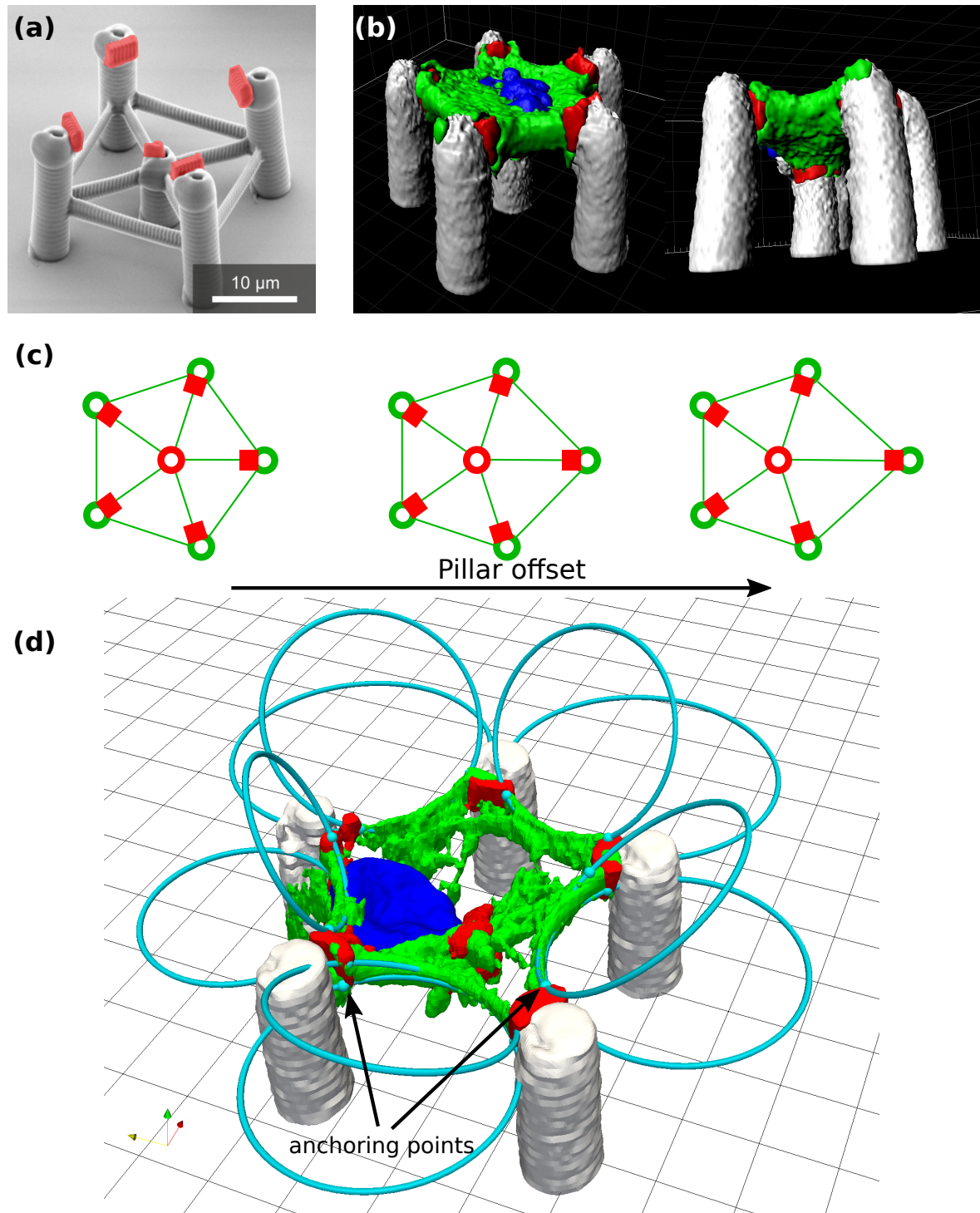


Figure 3.4.: 3D microscavolds for normalizing cell shape in 3D. **(a)** Electron microscopy image of a scaffold with four pillars arranged around a central, lower pillar. Fibronectin coated adhesion sites are colored in red. **(b)** Rendering of a pentagonal structure with a 3T3 fibroblast adhering inside, reconstructed from a 3D image. Outer envelope of the actin CSK (green), nucleus (blue) and adhesion sites (red) are shown. Courtesy of Benjamin Richter and Kai Weißenbruch, Bastmeyer group (KIT). *(Continued on next page)*

Figure 3.4 (continued): (c) Modification of pentagonal structures by displacing one pillar in order to increase spanning distance between adhesion sites. **(d)** Reconstruction of SFs of a 3T3 fibroblast inside a pentagonal scaffold. Circles (cyan) were fitted to invaginated actin arcs. Anchoring points of arcs to adhesion sites are symbolized by spheres. Rectangular grid has a spacing of 5 μm .

Fig. 3.4d shows a reconstruction of a cell in a pentagonal scaffold with circles fitted to the SFs. The underlying image data was obtained by confocal microscopy. The actin CSK (green) was segmented with the software Imaris (Bitplane AG, Zürich) in such a way that only the brightest features, i.e. SFs, remain. Between the adhesive cubes (red) stripe-like structures span, which are in fact formed by one SF in the xy-plane and one that is tilted. Due to the lower resolution in z-direction, both fibers are smeared out into one structure. By carefully examining image stacks in z-direction it is nevertheless possible to mark points where the fibers are attached to the adhesion sites and fit circles in the xy-plane as well as the tilted plane. The approach for circle fitting will be explained in Section 3.2.2.

Arcs that span between the outer and the central adhesion sites were more difficult to detect in the images due a lower arc intensity and lesser resolution in z-direction. In fact, for 36 arcs in xy-plane and tilted planes, which could be fitted to various cells in a regular pentagonal structure, we could only clearly estimate 3 arcs that span between the outer and inner adhesion sites. Also image stacks obtained by SIM showed only very few of those arcs. For this reason, we did not include such arcs into our analysis.

To estimate radii of curvature and spanning distance of the circular arcs, we had access to micrographs obtained by laser scanning confocal microscopy with varying resolution in the xy-plane. One of the pillars was moved with an offset between 0 μm and 7.5 μm to extend the range of possible spanning distances. We were able to fit 189 arcs to the micrographs and extracted the corresponding parameters. We distinguished between arcs that lie in the xy-plane and arcs that had a tilted plane, as can be seen in Fig. 3.5.

As in Section 3.1.1, we fitted the tension-elasticity model

$$R = l_f \left(\frac{2R}{\alpha d} \arcsin \left(\frac{d}{2R} \right) - 1 \right) \quad (3.4)$$

to the extracted arc radii and spanning distances and chose $\alpha = L_0/d = 1$ to estimate the length scale $l_f = EA/\sigma$. The best fit for the measured values of d and R to Eq. (3.4) is given for $l_f = 37.4 \mu\text{m}$. Fits of the tension-elasticity model to fibroblasts on 2D substrates yield values of $l_f \approx 1 \text{ mm}$, which is significantly higher [21]. In the same paper, the

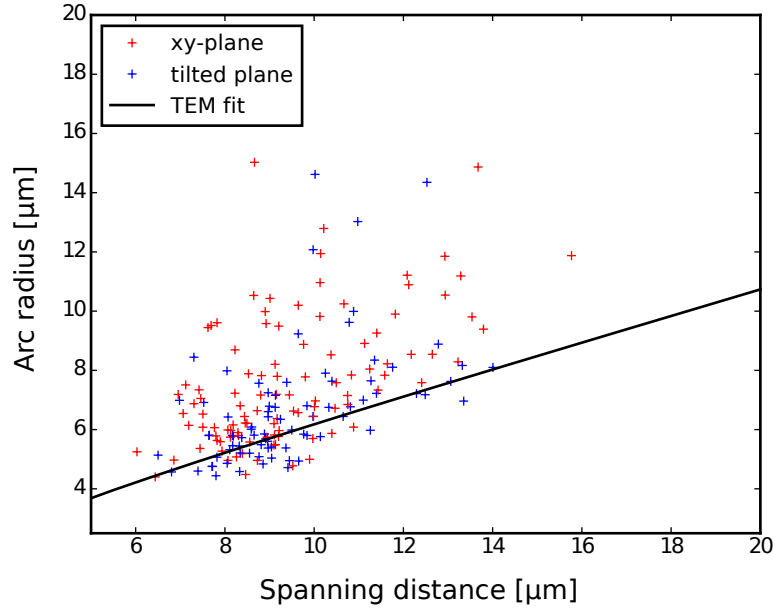


Figure 3.5.: Plot of arc radius versus spanning distance for 189 circular arcs extracted from cells in pentagonal scaffolds. Arcs that lie in the xy-plane and in the tilted plane are shown as red or blue crosses, respectively. Black line represents a fit to the tension-elasticity model (Eq. (3.4)) with fixed parameter $\alpha = 1$. The fitted parameter is $l_f = 37.4 \mu\text{m}$.

authors showed that a chemical reduction of acto-myosin contractility results in values of $l_f \approx 70 \mu\text{m}$. Cells in 3D environments form less, or less bright, SFs and our estimation of a lower l_f quantifies this observation and suggests that the analyzed SFs are weaker than their 2D counterparts. In our experiments and the experiments of [21] fibroblasts were used, but the different cell lines (3T3 versus BRL) could explain some of this difference. Nevertheless, we hypothesize that the 3D adhesion geometry is the dominant effect.

3.2.2. Fitting of actin arcs in 3D

To estimate arc parameters, such as radius of curvature, center, and spanning distance, we developed a software tool that allows for manual selection of two anchoring points and additional points along the arc. Circles are then fitted to these points by a least squares method.

Experiments with cells in 3D microscaffolds are more complicated compared to 2D substrates and the total number of cells suitable for analysis is significantly lower. Therefore, we opted for manual annotation of the arcs, because an automated detection procedure in 3D is a challenging task and not necessary for our purpose. Also scenarios such

as high-throughput screens are not in the focus of this project and so there is decreased need for automation.

The parameter estimation of the circular arcs runs in multiple steps. The first step is to find a plane in 3D space in which the arc lies. This is achieved by annotation of two anchoring points of the arc in the volume image and a third point that lies somewhere on the arc. The plane spanned by these three points is now extracted from the original image and presented to the user for further annotation. We do not only return the plane of the arc, but a volume image centered around the plane. In this image, slices along the z-axis represent parallel planes to the original one. Thus, the user can refine the selection of the arc plane, in case the original annotations were slightly imprecise.

Given the initial user annotations

$$\begin{aligned}\mathbf{p}_1 &\hat{=} \text{1st anchoring point} \\ \mathbf{p}_2 &\hat{=} \text{2nd anchoring point} \\ \mathbf{p}_3 &\hat{=} \text{point along arc,}\end{aligned}$$

we define a unit-vector $\hat{\mathbf{a}}$ pointing from \mathbf{p}_1 to \mathbf{p}_2 , the plane normal $\hat{\mathbf{c}}$, and a unit-vector $\hat{\mathbf{b}}$ orthogonal to $\hat{\mathbf{a}}$ and $\hat{\mathbf{c}}$ as

$$\begin{aligned}\hat{\mathbf{a}} &= \frac{\mathbf{p}_2 - \mathbf{p}_1}{|\mathbf{p}_2 - \mathbf{p}_1|} \\ \hat{\mathbf{c}} &= \frac{(\mathbf{p}_2 - \mathbf{p}_3) \times (\mathbf{p}_1 - \mathbf{p}_3)}{|\mathbf{p}_2 - \mathbf{p}_3| |\mathbf{p}_1 - \mathbf{p}_3|} \\ \hat{\mathbf{b}} &= \hat{\mathbf{c}} \times \hat{\mathbf{a}}.\end{aligned}\tag{3.5}$$

These three vectors will form the coordinate axes of the extracted volume image presented to the user for further annotations.

A rotation matrix R that transforms the original image coordinate system $(\hat{\mathbf{e}}_x, \hat{\mathbf{e}}_y, \hat{\mathbf{e}}_z)$ is given by

$$R = \begin{bmatrix} a_1 & b_1 & c_1 \\ a_2 & b_2 & c_2 \\ a_3 & b_3 & c_3 \end{bmatrix}.\tag{3.6}$$

The center \mathbf{p}_c of the extracted volume is defined as a point between the original annotations

$$\mathbf{p}_c = \frac{\mathbf{p}_1 + \mathbf{p}_2}{4} + \frac{\mathbf{p}_3}{2}.\tag{3.7}$$

In a second step, the user again selects anchoring points, now in the plane in which the

arc lies, and additional points along the arc. With the two anchoring points and about 10 additional annotated points along the arcs, a circle is fitted by a modified least squares method (MLS) [168].

As a last step, the annotated points and the circle parameters are transformed back into the original coordinate system and saved for further analysis.

3.2.3. Combining experimental results with theoretical modeling

To gain further insight into the mechanical properties of cells adhering in 3D microscavolds, we combined the procedure of extracting parameters of the circular arcs that form between adhesion sites with a computational model for cell shape. In this model, a triangulated network of active cables represents the cell membrane with the underlying actin cortex and peripheral SFs.

The adhesion points of the modeled cell were fixed according to the regular pentagonal scaffold. From an initial shape, which is generated by connecting adhesion points by straight lines, elastic energies and active tensions were optimized to obtain an equilibrium shape [122].

A least squares fit of the tension-elasticity model (Eq. (3.4)) to arc radii extracted only from cells adhering in the regular pentagonal scaffolds yields $l_f \approx 46 \mu\text{m}$, which justifies the parameter choices of the model. The rest-length parameter was $a = 1$ and the length scale was chosen to be $l_f = 50 \mu\text{m}$.

From the experiments, radii of curvature of circular arcs in the xy-plane and in a tilted plane were estimated as $R_{xy,exp} = (7.3 \pm 1.4) \mu\text{m}$ and, $R_{tilted,exp} = (5.7 \pm 0.9) \mu\text{m}$. The corresponding radii of the computational model are $R_{xy,sim} = 7.7 \mu\text{m}$ and $R_{tilted,sim} = 5.9 \mu\text{m}$ and show very good agreement with the experimentally measured parameters.

A comparison between a cell shape predicted by the model and a segmented cell from experimental data is shown in Fig. 3.6. The shape of the invaginated regions of the model closely resemble the actin structures found by segmenting experimental data (Fig. 3.6a,b). Interestingly, the elastic tension acting on the links of the triangulated mesh is highest in the same regions where SFs are located in the experiments (Fig. 3.6c). The highest values can be found along arcs that lie in the tilted plane, followed by the xy-plane and lastly between the connection of the outer to the inner adhesion sites. By this, the model can quantitatively explain the localization of SFs in the experiments and it becomes clear that the lower number and lower intensity of SFs between the outer and the inner adhesion sites can be explained by lower elastic tension and thereby less need for reinforcement.

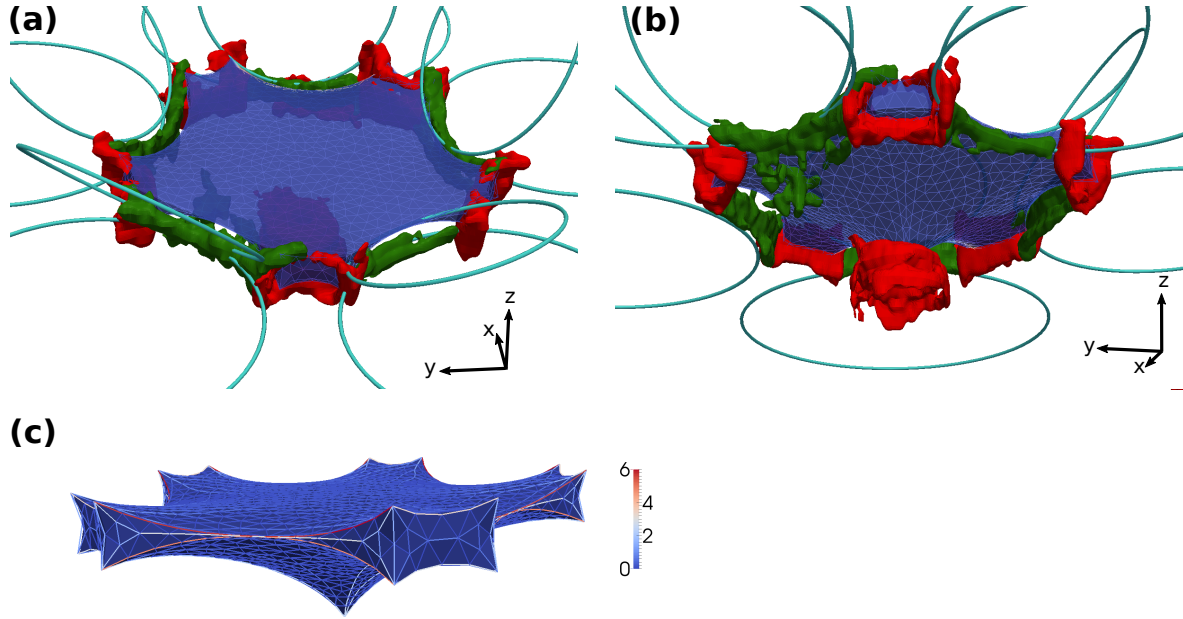


Figure 3.6.: Comparison between a segmentation of the actin CSK (green) and the shape of a cell obtained by computational modeling (blue). **(a)** View from above. Adhesive regions of the micro scaffold are shown in red. Circles fitted to actin arcs are shown in cyan and were used for parameter estimation of the model (cf. main text). **(b)** View from below. Micro scaffolds are not shown. **(c)** Cell shape predicted by computational model with elastic tension on the links of the triangulated network in color code.

3.2.4. Conclusion

In this section we extended the analysis of peripheral, circular actin arcs between adhesion sites into 3D. We presented a method to fit circles to such SFs of arbitrary orientation by extracting the plane in which the arc lies from a volume image. In this plane, circles were fitted in a semi-automated way by estimating the center and radius from user annotations by a least-squares method.

Our collaboration partner, the Bastmeyer group at KIT, recorded volume images of 3T3 fibroblast cells adhering in 3D micro scaffolds, which were fabricated by direct laser writing. Utilizing the precisely defined adhesion geometry of such scaffolds, we could extract radii of curvature and spanning distances from peripheral SFs with our custom written software. From those arc parameters we could determine the relevant length scale l_f of the tension-elasticity model and could quantify that SFs forming in 3D environments are weaker than corresponding fibers in 2D.

Furthermore, we combined the analysis of experimental data with a computational model developed by Christoph Brand [122]. This model yields excellent agreement be-

tween measured and simulated arc radii and also explains that circular arcs form predominantly in the xy-plane and a tilted plane due to condensation of stress in this regions.

In future work on this topic one could combine dynamic experiments with advanced computational modeling to gain further insights into cellular mechanics in 3D. By laser-cutting of SFs or controlled detachment of the cell from one of the adhesion sites, in combination with live-cell imaging, one could study the retraction dynamics of the tensed fibers. In combination with a refined computational model, for example based on finite-elements, forces in the fibers can be estimated.

3.3. Analysis of stress fiber microstructure

In Sections 3.1 and 3.2 we fitted circles to arc-like peripheral SF and could explain the positive correlation between arc radius R and spanning distance d with the tension-elasticity model. By fitting an implicit relation between R and d , a length scale $l_f = EA/\sigma$, i.e. the ratio of fiber rigidity and surface tension, can be estimated. The tension-elasticity model ignores the SF microstructure and for more detailed modeling approaches it would be desirable to connect stochastic models of motor activity with predictions for fiber and cell mechanics.

The force generating units in SFs are bipolar myosin II minifilaments that consist of 2x14 myosin molecules with a total of 58 motor heads [170]. They can generate forces in the pN range by performing steps on actin filaments, which combine into nN forces that SFs exert on adhesion sites. These minifilaments have a length of approximately 300 nm [170] and therefore are very close to the diffraction limit, resolvable with confocal microscopes. Recently it has been demonstrated that the N-terminal of the myosin head and the C-terminal of the myosin tail can be labeled with different fluorophores [171]. In combination with super-resolution techniques, such as structured illumination microscopy, the location of the minifilaments centers as well as the tails can be determined with high precision (Fig. 3.7a). By this, the location and orientation of individual minifilaments can be measured and related to SF architecture (Fig. 3.7b).

In this section, we present a workflow to detect the location of myosin minifilaments and extract intensity profiles along SFs that can serve as input for more detailed models of SF contractility. The experiments were conducted by Kai Weißenbruch from the group of Martin Bastmeyer (KIT). Two-dimensional microdot substrates, manufactured by microcontact printing, were used to allow the formation of free spanning SFs. For imaging, structured illumination microscopy was used.

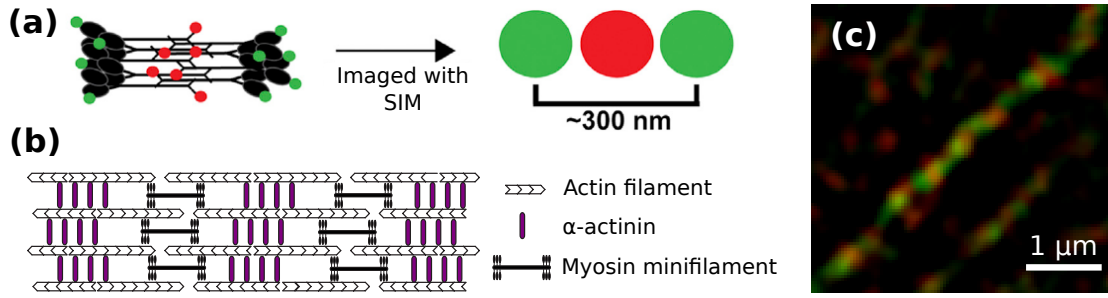


Figure 3.7.: (a) Sketch of fluorescent labeling of myosin heads (green) and tails (red). Structured illumination microscopy allows to resolve groups of heads or tails. Adapted from [171]. (b) Simplified SF microstructure with myosin minifilaments as force generating elements and α -actinin crosslinkers. Adapted from [172]. (c) Crop of a fluorescent micrograph obtained by SIM illustrates the regular organization of myosin heads and tails along a SF at the image diagonal. Image courtesy of Kai Weißenbruch (KIT).

3.3.1. Localization of myosin II minifilaments

The image data available for this project contains different combinations of channels with fluorescent labeling of myosin heads, myosin tails, α -actinin, DNA, actin and the fibronectin microdots. Of all those labelings up to four channels could be imaged in a single setup and labels for actin as well as the microdot pattern were present in all micrographs.

As we want to explore the microstructure of SFs, we start by detecting individual SFs. For this, the methods of automated detection of circular arcs presented in Section 3.1 can be used, but here we were also interested in straight, non-peripheral SFs, which cannot be easily estimated with such a method. We therefore used the software tool FilamentSensor [147] to detect filamentous structures in the actin channel. This software uses several line-enhancing pre-filters and algorithms originally developed for detection of fingerprints and was provided by Benjamin Eltzner and Florian Rehfeldt (University of Göttingen). Manual setting of filter parameters is needed, but after this, filaments can be detected in an automated way for multiple images.

In further post-processing steps, the chain of coordinates along the detected filaments was fitted to the brightest region of the fiber in order to correct for slight inaccuracies caused by the FilamentSensor.

Using those processed chains of coordinates, we extracted intensity profiles from the various channels for further analysis. Localization of myosin tails could be achieved by detecting peaks along an intensity profile.

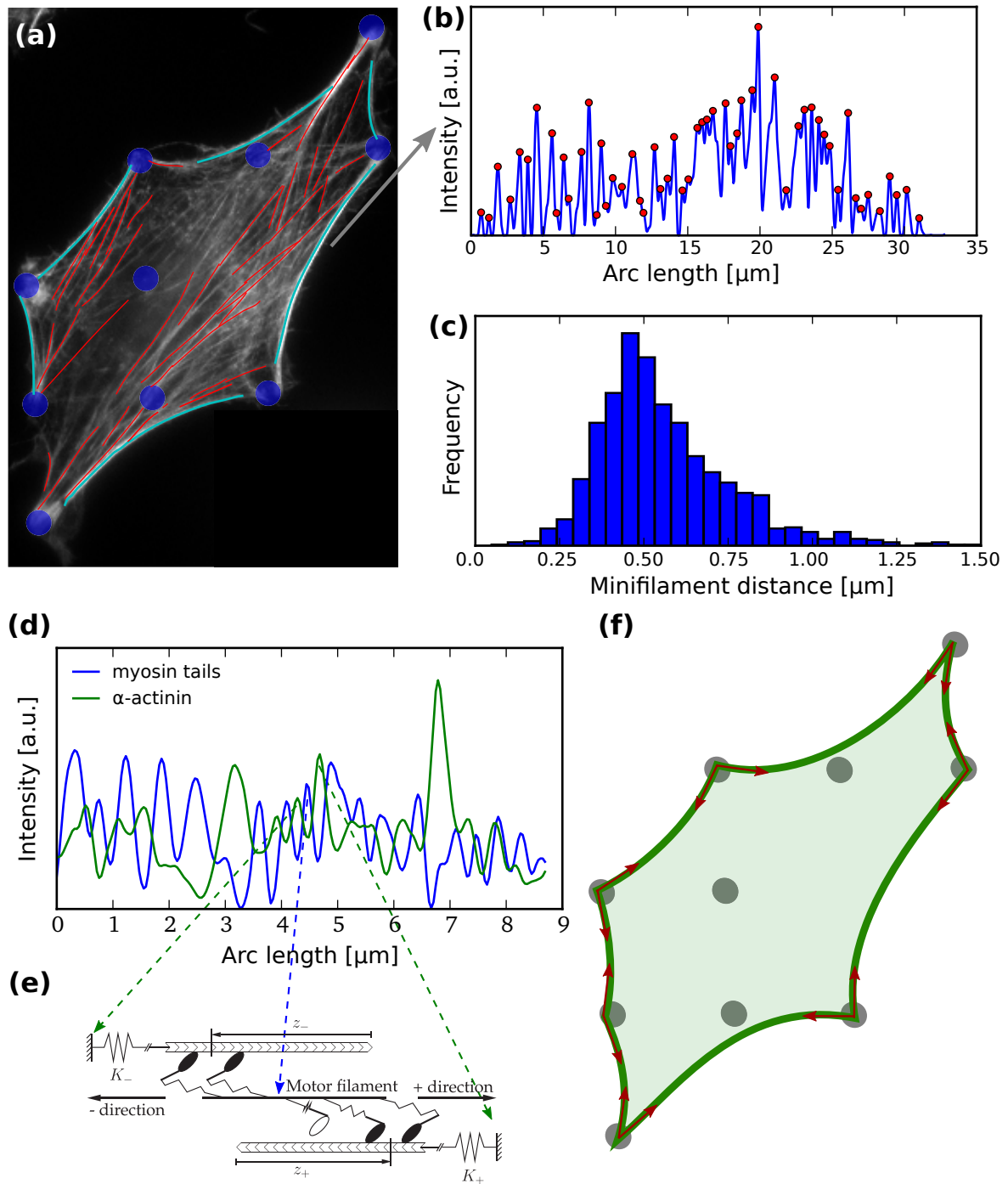


Figure 3.8.: (a) Fluorescent micrograph of a 3T3 fibroblast (actin channel is shown) adhering on a dot micropattern (sketched in blue). Stress fibers detected with the FilamentSensor are overlaid. Red fibers have been excluded from the analysis. (b) Intensity profile along one SF of the channel with staining of myosin tails. Peaks correspond to extracted positions of myosin tails. (c) Histogram of distances between individual myosin minifilaments, measured as the myosin tail-tail distance. Data is aggregated from 8 cells with a total of 78 SFs. (Continued on next page.)

Figure 3.8 (continued): (d) Intensity profile along a SF with staining of the myosin tails (blue) and α -actinin (green) shows alternating pattern of peaks. (e) Locations of peaks can be used to translate a microscopic model of for one minifilament to the scale of the complete SF. Figure from [173]. (f) Whole-filament model can be used to estimate force distribution on the cellular level (red arrows).

3.3.2. Results and outlook

In Fig. 3.8 we present results of the analysis method outlined above applied to micrographs of 3T3 fibroblasts adhering on a microdot substrate. We limited the initial analysis to peripheral SFs as they usually show the highest intensity and we expect them to be the most contractile fibers and have a high concentration of myosin minifilaments (Fig. 3.8a). By extracting intensity profiles along the fibers of the image channel with staining of the myosin tails, we could estimate the centers of the minifilaments by locating peaks in the profile (Fig. 3.8b). We found that the distribution of the minifilament center-to-center distances is strongly peaked at ≈ 456 nm (Fig. 3.8c).

The results presented above are a proof of concept for the workflow and can be used for future modeling efforts. By localizing α -actinin crosslinkers, all the main components of the SF can be extracted from images (Fig. 3.8d). This allows to assemble microscopic models of minifilament, e.g. based on stochastic simulations [173], into a whole-fiber model with detailed microstructure (Fig. 3.8e). Such filament models can be combined to compute the cellular stress distribution of a cell adhering to a microdot substrate (Fig. 3.8f) and could be combined with traction force measurements [174] that have been applied previously to MP substrates [123, 175].

Intracellular dynamics of the actin cytoskeleton

So far, we only investigated static recordings of the CSK. This is appropriate for the analysis of a cell in a quasi steady state that can be achieved for example by adhesive islands on which individual cells adhere in such a way that fluctuations in shape are minimized. In homeostatic epithelial tissue for example, one can also assume that changes to the cells surrounding happen on longer timescales and the ECM stays in a steady state [176]. Although the changes in cell shape are minor in such a steady state, the CSK undergoes constant turnover and thus enables cells to quickly adapt to changes in the extracellular environment that might occur e.g. due to wounding of the tissue layer, where proliferation and cell migration rates increase [177].

In order to investigate how specific components of the CSK are regulated and how this relates to their mechanical properties, precise control of the involved pathways are necessary, such as the RhoA regulatory pathway that controls acto-myosin contractility (Section 1.4.5, Fig. 1.10c).

One very elegant way of manipulating intracellular signaling pathways is optogenetics. It is a technique that combines genetic modifications of some of the regulatory proteins and stimulation with light to control specific functions in cells [178]. Optogenetics was first developed in the field of neuroscience to control membrane channels in neurons by light [179, 180], but since has become widely used also in other fields of research, e.g. as a method to precisely modulate cellular signaling [181].

Recent development of proteins that switch between two conformational states upon stimulation with light have made it possible to manipulate cellular signaling pathways with high spatiotemporal precision [182]. Specifically tailored versions of such proteins

can be attached to the cell membrane and under stimulation with light, they recruit GEFs, which promote the transition of RhoA to its active GTP-bound state. This then sets the downstream effects of acto-myosin contractility in motion.

By using such photoactivatable constructs, cellular contractility can be controlled locally in regions of high SFs density. Snapshots of timelapse recordings with fluorescent staining of actin or myosin II show an increase in intensity within the activation region (marked as red boxes in Fig. 4.1), which is correlated with increased local contractility. The activation was carried out over a period of 15 minutes followed by a relaxation period of 15 minutes.

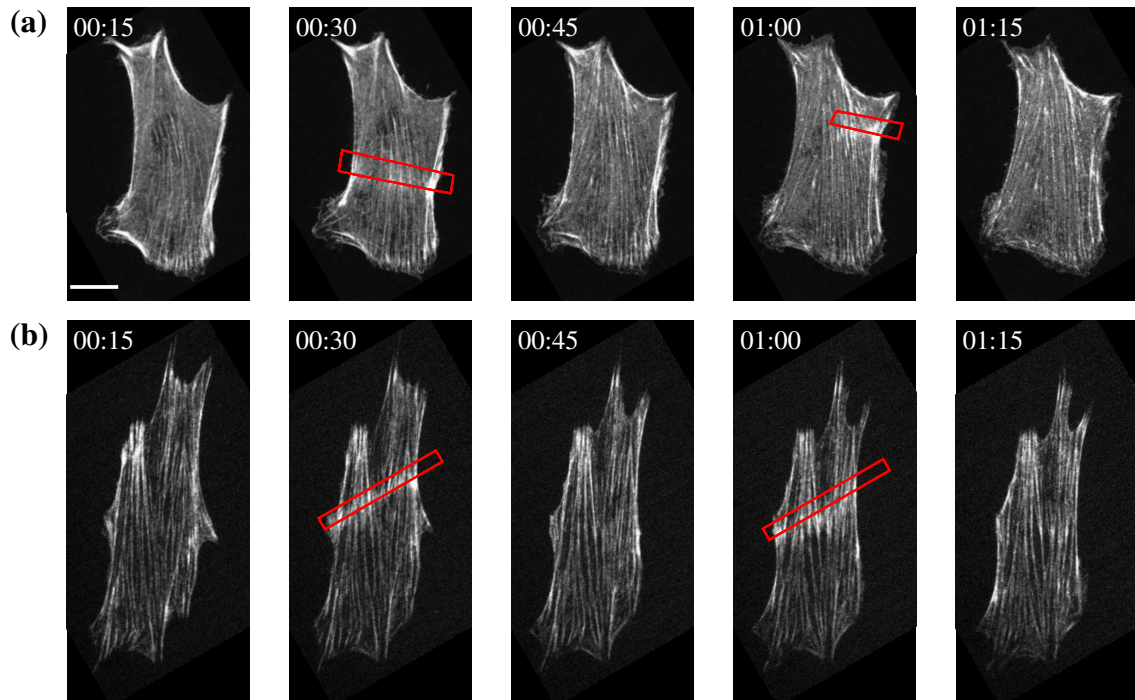


Figure 4.1.: Snapshots of timelapse recordings of 3T3 fibroblasts with (a) fluorescent staining of actin and (b) of myosin. Red boxes mark regions of photoactivation of RhoA leading to locally increased actin and myosin intensities and higher cellular contractility. Multiple activations in different regions of the cell are possible. Time is given in minutes, scale bar has a length of 10 μm .

In this chapter we measure cytoskeletal flow fields, induced by photoactivation, with an optical flow method. By this, we can investigate how SFs and their mechanical properties are involved cellular contraction and relaxation dynamics. The results presented in this chapter are based on collaborative work with Patrick Oakes, Margaret Gardel, Elizabeth Wagner and Michael Glotzer from the University of Chicago and Christoph Brand and Dimitri Probst from the Schwarz group. A manuscript with additional results has been

submitted and is currently under revision [183].

4.1. Validation of the optical flow method

The OF method introduced in Section 2.5 was developed and tested with the aim to apply it to natural images such as movie sequences. To check the applicability of the algorithm implemented in [167] to biological data, we created artificial test data for which the ground truth was known and used the algorithm on this data.

By observing timelapse recordings of cells in which RhoA was locally activated we noted that the CSK flow was predominantly converging to the region of activation, which is in agreement with the increased myosin concentration in this region. To check whether the OF method outlined in Section 2.5 can detect and precisely estimate such patterns, we define a velocity field that converges towards the center of a square region

$$\begin{pmatrix} u(x, y) \\ v(x, y) \end{pmatrix} = v_0 \Pi\left(\frac{t}{2T} - \frac{1}{2}\right) \text{sign}\left(\frac{T}{2} - t\right) \begin{pmatrix} \text{sign}(x) \\ 0 \end{pmatrix} \quad (4.1)$$

Here v_0 is a constant defining the speed of the velocity field, and after a period T of constant flow the direction of the flow is inverted. This mimics the backflow that is also observed in experimental time lapse recordings. $\Pi(t)$ is the rectangle function.

To generate an image sequence that represents movement according to the velocity field, random spot positions were drawn and propagated in the field. From the distribution of spots, images were generated that were used for validating the OF method. We found that the number of spots had only minor influence on the reconstruction accuracy. This results most likely from the spatial and temporal smoothness constraints imposed on the reconstructed velocity field. To make the synthetic data comparable to the experimental recordings, we chose a number of $N_{\text{spots}} = 500$ for an image size of 500px by 500px (cf. Fig. 4.2a). Gaussian smoothing was applied to the synthetic images and Gaussian white noise with variance σ^2 was added before the OF algorithm was applied. The size of the synthetic images and the velocities were chosen to match experimental image sizes as well as the temporal sampling interval of 20 seconds with velocities estimated on the order of ≈ 10 nm/s. With a pixel size of approximately 100 nm, a displacement of approximately 2 px can be expected.

We found that for a large range of the noise variance the OF method could reconstruct the underlying velocity field with high precision. Only for very high values of $\sigma^2 = 0.05$ and $\sigma^2 = 0.1$ deviations from the ground truth were found (Fig. 4.2b). For $\sigma^2 = 0.01$ we

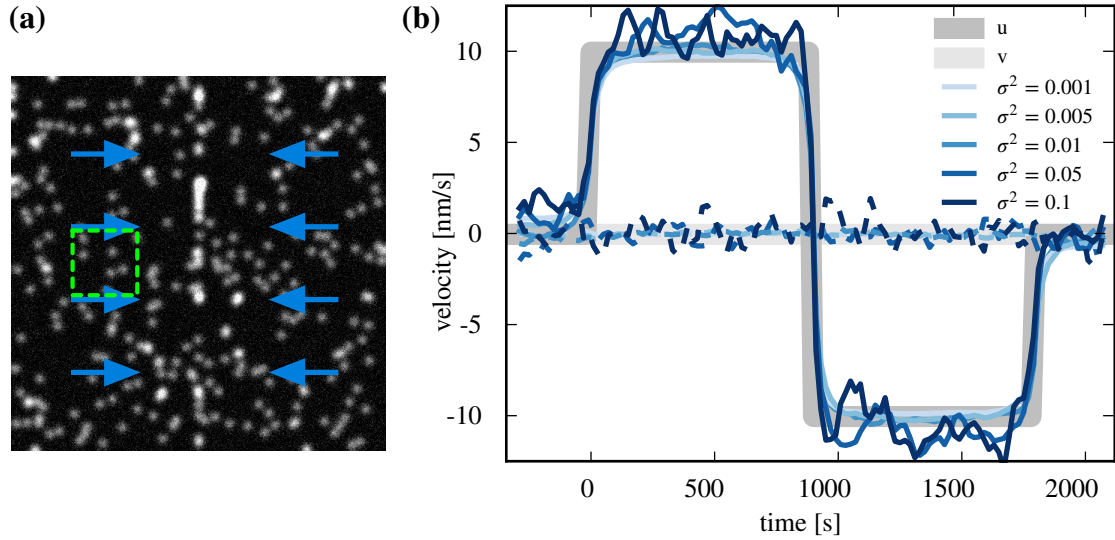


Figure 4.2.: Validation of the OF method. **(a)** Test data of random speckles, which move in a flow field parallel to the x-axis that converges towards the center of the rectangular image (blue arrows). Reconstructed velocity fields by the OF method are averaged inside the green box. **(b)** Comparison of the ground truth velocity inside the box (bold gray lines) and the velocity in x-direction (colored, solid lines) and in y-direction (dashed lines) for different strengths of Gaussian white noise added to the images.

estimated a signal-to-noise ratio (SNR) of the synthetic images of $\text{SNR}_{\sigma^2=0.01} \approx 4$, where we defined the SNR as:

$$\text{SNR} = \frac{\mu_{\text{Data}}}{\sigma_{\text{BG}}}, \quad (4.2)$$

with μ_{Data} the mean intensity of the relevant objects in the image and σ_{BG} the standard deviation of the background. For a sample image taken from an experimental time lapse sequence, the SNR was estimated as $\text{SNR}_{\text{epx}} \approx 5.3$, which is of the same size as $\text{SNR}_{\sigma^2=0.005} \approx 5.4$ for the synthetic images.

With the OF method we are therefore able to reconstruct an underlying velocity field with high precision from the experimental time lapse recordings provided by our collaboration partners.

4.2. Correlating cytoskeletal flow and stress fiber orientation

Christoph Brand from the Schwarz group developed a computational model based on a triangulated network of cables to simulate the effect of locally enhanced contractility

[122]. In the triangulated network, links were modeled as a combination of a cable-Maxwell element (series connection of a viscous element and an elastic spring) and an active contracting element, mimicking a crosslinked actin network. SFs were embedded in the network and modeled in the same fashion, but with different parameters. To simulate local activation, the tension of the contractile elements was increased inside the activation region. If the actively contracting elements were placed in both, the network links and the SFs, lateral contractions towards the activation region could be observed. In contrast to this, purely longitudinal contraction was observed if the active elements were only distributed in the SFs.

In the time lapse recordings of real cells only the second case of longitudinal contraction could be noted. These modeling results and experimental observations indicate that SFs are indeed one dimensional contractile elements that are embedded in a passive (or much less contractile) acto-myosin network [183].

To quantify the longitudinal contraction along SFs predicted by the computational model, we developed a method to correlate flow direction and local orientation of the actin CSK. For this, the structure tensor \mathbf{J} (Eq. (2.11)) was used to estimate the local orientation ϑ_{actin} and the coherency c from the time lapse recordings. To visualize correlations between flow direction and local orientation, we defined a correlation measure ρ

$$\rho(x, y) = C_0^1 \left(\frac{|\mathbf{v}(x, y)| - |\mathbf{v}|_{\min}}{|\mathbf{v}|_{\max} - |\mathbf{v}|_{\min}} \right) c(x, y) \cos \left(2(\vartheta_{\mathbf{v}}(x, y) - \vartheta_{\text{actin}}(x, y)) \right), \quad (4.3)$$

where

$$C_a^b(x) = \begin{cases} a & x < a \\ x & a \leq x \leq b \\ b & x > b \end{cases} \quad (4.4)$$

clips its argument between a and b . $|\mathbf{v}(x, y)|$ is the magnitude of the velocity, $|\mathbf{v}|_{\min}$ and $|\mathbf{v}|_{\max}$ minimal and maximal velocities considered for plotting (here determined by the 10th and 95th percentiles of $|\mathbf{v}(x, y)|$) and $\vartheta_{\mathbf{v}}(x, y)$ is the direction of flow. ρ ranges between -1 for a flow orthogonal to the orientation of the actin CSK and 1 for parallel flow direction and actin orientation. For visualization, ρ was color-coded and overlaid over the snapshots of the timelapse sequence.

4.3. Results

Our experimental collaboration partners conducted experiments with staining actin, myosin and α -actinin. By means of actin and myosin staining, SFs and smaller filamentous structures become visible and, under α -actinin staining, characteristic striation patterns emerge that visualize the sarcomeres of the SFs [70].

In Fig. 4.3a snapshots of a timelapse recording of a cell with actin staining are shown. RhoA is photoactivated near the cell periphery (blue ellipse), which leads to the flow pattern shown in green. Before the activation ($t=00:07$ min) there is initial CSK flow normal to the SFs in the lower part of the cell, which is due to initial contraction of the cell and also caused by retrograde flow of depolymerized actin monomers away from the cell edge. Upon photoactivation ($t=00:13$ min) the CSK flow pattern changes direction towards the activation region, because now myosin motors are recruited to the activation region leading to active contractility of the SFs. The sketch in Fig. 4.3b displays how SFs contraction leads to an increased tension. Notice that the viscous elements of the modeled SFs are not shown for simplicity. During activation, the SFs in the lower part of the cell are being tensed and at the end of the activation period ($t=00:27$ min) only normal flow w.r.t. the SFs in the lower part of the cell is visible. This indicates that the SFs is now under high tension and is pulling the lower part of the cell inside as it is straightening under the influence of increased myosin activity. After the photoactivation is turned off ($t=00:33$ min) a strong backflow is visible that is tangential to the direction of the SFs and again some orthogonal movement can be seen in the lower part of the cell due to smaller fibers that are being dragged along as the large fibers relax.

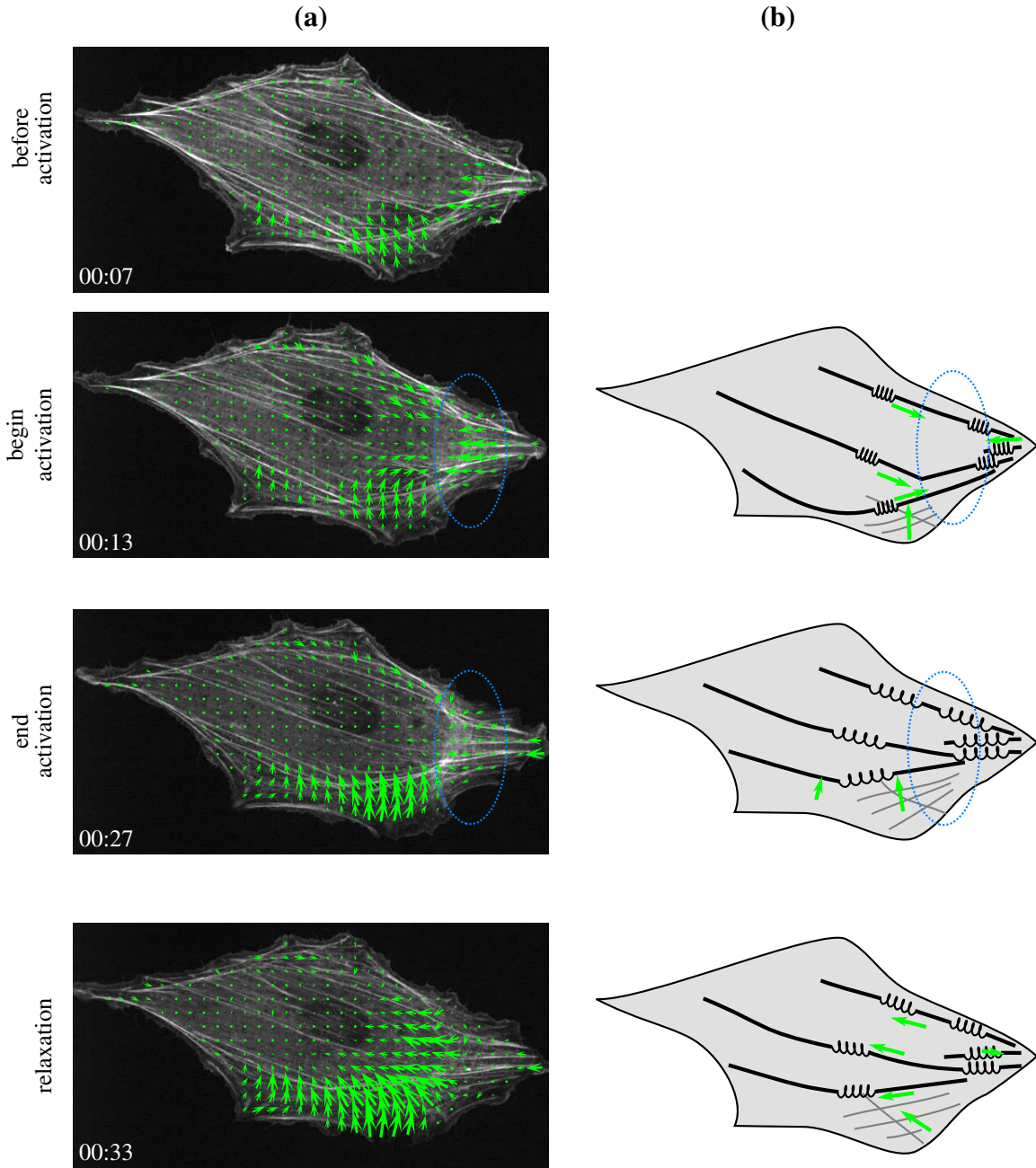


Figure 4.3.: (a) Snapshots of time lapse recordings of a 3T3 cell with fluorescent staining of actin with an overlay of the calculated CSK flow (green). Time points were chosen before photoactivation of RhoA, at the start of the activation period (activation region marked by blue ellipse), at the end of the 15 minute activation period and during the relaxation of the cell. (b) Cartoons with strongly simplified layout of the actin SFs. Due to contraction towards the activation region, SFs get stretched and tension builds up, which is released after the photoactivation is turned off.

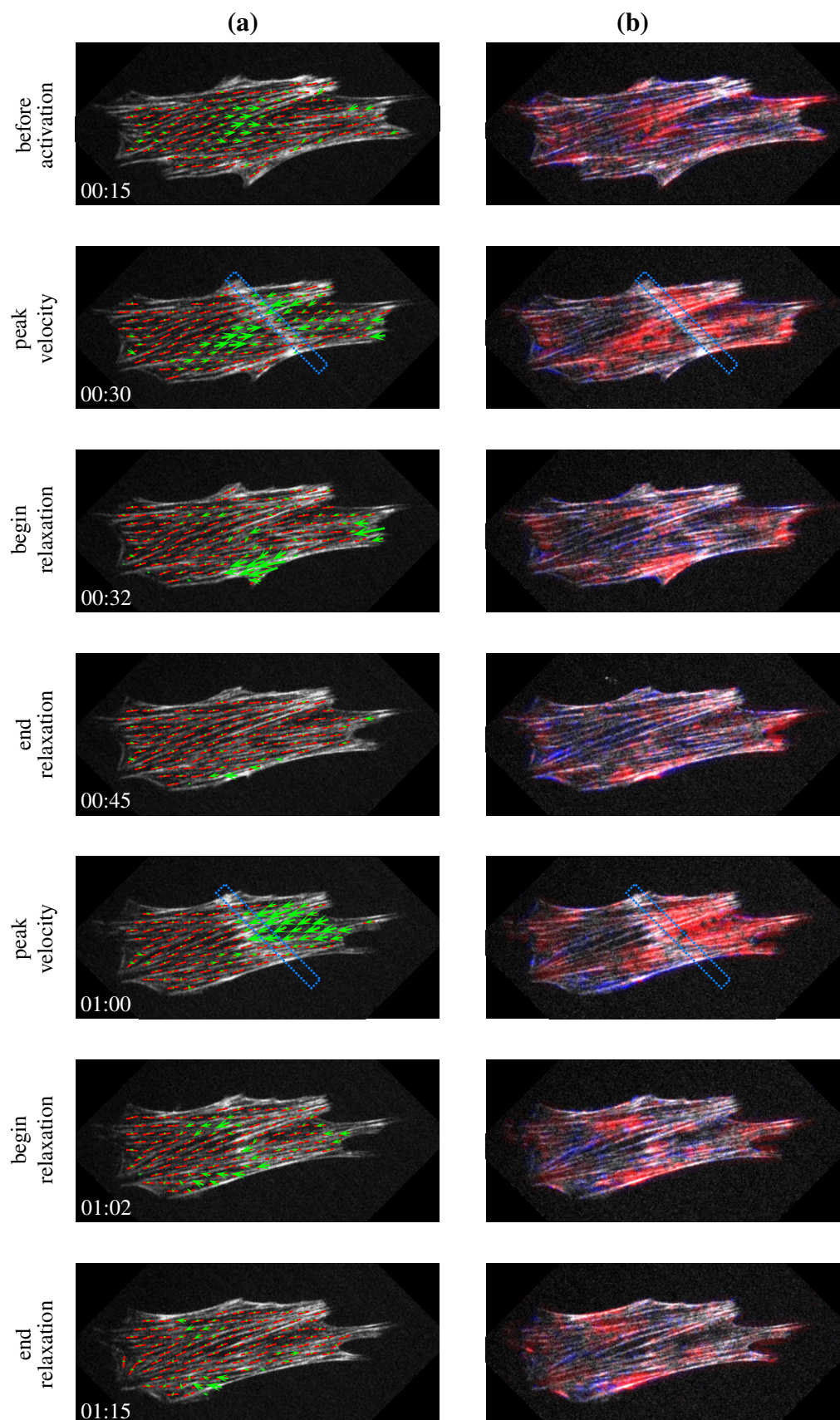


Figure 4.4 (previous page): (a) Snapshots of time lapse recordings of a 3T3 cell with fluorescent staining of myosin and an overlay of the CSK orientation (red bars) as well as the calculated CSK flow (green). Characteristic periods of the experiment are selected: Shortly before photoactivation of RhoA begins (00:15), when the maximum velocity is established (00:30), shortly after the activation has stopped (00:32) and after 15 minutes of relaxation (00:45). A second activation period starts subsequently. (b) Overlay of the correlation ρ (Eq. (4.3)) between flow direction and CSK orientation, which is weighted by the magnitude of the flow velocity and the coherency c extracted from the structure tensor. Red color symbolizes parallel alignment of flow direction and CSK orientation, blue color orthogonal alignment.

In Fig. 4.4 the correlation between SF orientation and CSK flow direction is even more evident. Here, a more linear cell is shown with SFs oriented along the cell's long axis and activation is carried out in the cell center, normal to the SFs. From the CSK flow fields in Fig. 4.4a it is evident that flow direction and SFs orientation coincide. This can also be seen in panel Fig. 4.4b, where the correlation measure R (Eq. (4.3)) between flow direction and SFs orientation is shown in color code (red: parallel, blue: orthogonal).

To quantify flow velocities during activation and relaxation, lines were placed along the SFs and kymographs were extracted from the fluorescent images as well as the CSK flow field, which was projected onto those lines. A kymograph is a representation of a dynamic process in a 2D image. It can be generated by a line scan through an image (Fig. 4.5a) and subsequent stacking of such line scans for multiple frames of an image sequence (Fig. 4.5b). In Fig. 4.5b a kymograph of the fluorescent intensity of myosin is shown with the temporal axis in horizontal orientation and the spatial axis in vertical direction. During photoactivation (orange boxes) of RhoA, movement towards the activation region can be observed that changes direction during the relaxation periods. The corresponding CSK flow field projected onto the kymograph line is shown in Fig. 4.5c. Flow direction is presented in color code with red color representing flow upwards along the spatial axis and blue downwards flow. Again it is clearly visible that there is contraction towards the activation region and a reversal for this effect during relaxation, which is indicated by a color change. Note, that the relaxation flow velocity is lower than the contraction flow as can also be seen in Fig. 4.4.

For further quantification, we placed multiple kymograph lines along the SFs in the cell and averaged the CSK flow velocity over all kymographs, separately for every experimental period (pre-activation, activation, relaxation) (Fig. 4.5d). Here it is again evident that the flow changes direction between activation and relaxation with an average flow velocity during activation of 3 nm/s. Notice that individual flow velocities can reach values

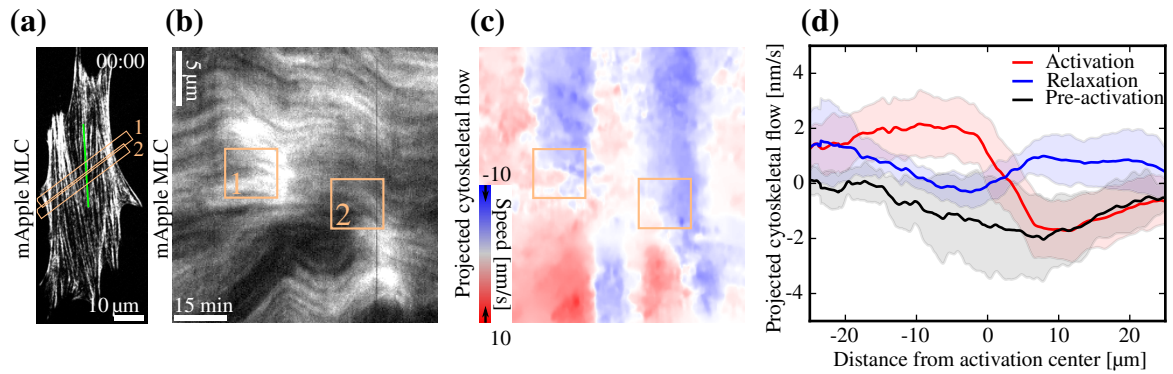


Figure 4.5.: Quantification of CSK flow velocity via kymographs. **(a)** Kymograph line (green) is placed along a SF. Activation regions (orange) cover the SF. **(b)** Kymograph generated from fluorescent image with time along the horizontal axis and space along the vertical axis shows flow towards the activation region and backflow during relaxation. **(c)** Cytoskeletal flow velocity projected onto the kymograph line with red color indicating flow upwards and blue indicating flow downwards. Flow points towards the region of activation and reverses direction during relaxation. **(d)** Projected flow velocity averaged over multiple kymographs with pre-activation, activation, and relaxation periods shown separately. Sign reversal of relaxation flow compared to activation flow is evident. Figure reproduced from [183].

up to $\approx 10 \text{ nm/s}$.

Furthermore, experiments were performed with fluorescent staining of the protein zyxin that is known to be responsible for retaining the mechanical integrity of SFs [184]. We observed that zyxin accumulated near the focal adhesions linked to contracting SFs and also at sites of compression within the activation region. This leads to the picture that zyxin is important for maintaining the connection between the focal adhesion and the SF and for repairing SF that are under compression. Another indication for this effect could be observed in cells that were manipulated to be depleted of zyxin. Here, the CSK flow pattern was identical to the previously discussed case during activation, but the backflow vanished entirely (Fig. 4.6a). By reintroducing zyxin into the cells, the backflow could be reestablished (Fig. 4.6b).

An estimation for the changes in the mechanical properties of SFs in zyxin-depleted cells could be achieved by the help of a 1D continuum model developed by Dimitri Probst [183]. This model was set up as a continuous version of the discrete network model mentioned above and can be considered as a continuous version of the parallel connection of Maxwell elements and active components responsible for contractility. This model was fitted to kymographs extracted from wild type and zyxin-depleted cells and it could be shown that the elastic modulus had to be increased by several orders of magnitude to fit

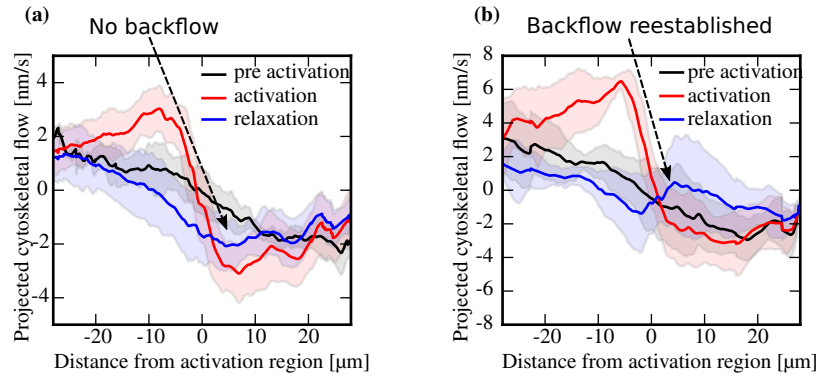


Figure 4.6.: (a) Cytoskeletal flow profile for zyxin-depleted cell shows no significant backflow. (b) In a cell with reintroduced zyxin the wild type flow pattern is reestablished.

the kymographs. At the same time the viscosity was lowered by one to two orders of magnitude. This indicates that without zyxin SFs are becoming stiffer and more viscous, which corresponds to the removal of the elastic element in the Maxwell model. Fits of the mechanical model to cells with reintroduced zyxin yielded parameters of the same size as for the wild type cell [183].

4.4. Conclusion

In this chapter we presented methods to investigate intracellular CSK dynamics and applied them to cells that were locally photoactivated, which causes an increased activity of acto-myosin complexes and thereby a contraction of the cell. We could show that SFs are one-dimensional contractile elements that are embedded into a passive actin mesh, which is not influenced by photoactivation of RhoA. This leads to CSK flow parallel to the SFs orientation.

We hypothesized that elastic elements in the SFs are being stretched during photoactivation of RhoA, which then causes a backflow once the light source is switched off. This hypothesis is supported mathematical models in which a ramped increase of contractility during activation and a slow decrease in the relaxation phase is sufficient to explain the experimental findings.

In a combined effort of experiments, computational models and image analysis, this work also highlights the repair and maintenance properties of zyxin for the mechanical integrity of SFs and its importance for keeping the elastic properties of SFs.

Analysis of the microtubule cytoskeleton

In earlier studies using MP substrates it was found that interaction between MTs and SFs is characteristically different from interactions with the actin cortex. MTs are deflected by SFs that span over non-adhesive parts of the substrate (Fig. 5.1a) [35] or are guided by internal SFs (Fig. 5.1b) [97]. At the cell cortex MT growth stops, most probably due to interactions with the densely crosslinked actin cortex [35]. In the following we discuss further experimental evidence for those phenomena and quantify the resulting organization of the MT network using MP substrates.

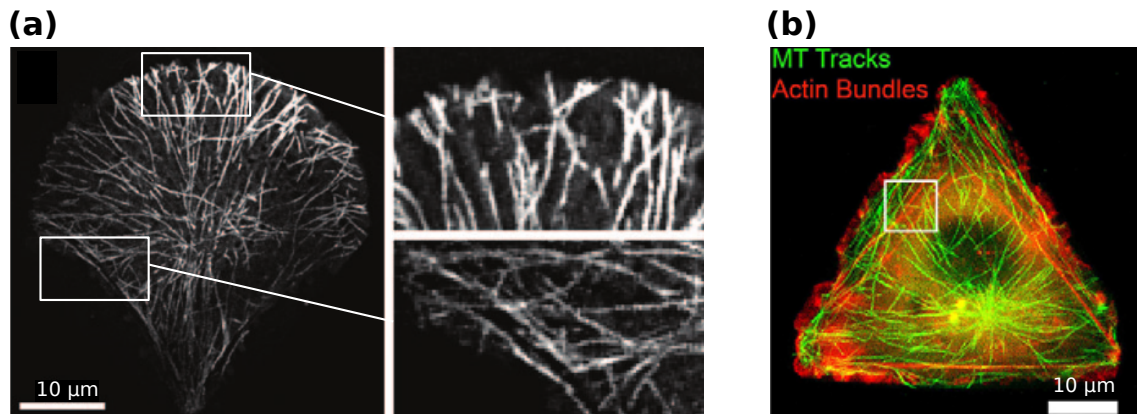


Figure 5.1.: (a) Tracks of growing MTs inside a cell on a ∇ -shaped MP. Growth is stopped at the convex boundaries (upper inset) and deflection can be observed at concave boundaries. Taken from [35]. (b) MT guidance at intracellular SFs of a cell adhering on a triangular micropattern. Taken from [97].

All cell culturing procedures were done in the group of Vytaute Starkuviene-Erfle by Susanne Reusing at BioQuant, Heidelberg University. For imaging, we used the mi-

croscopes of the group of Holger Erfle at the ViroQuant-CellNetworks RNAi Screening Facility and thank Manuel Gunkel for giving an introduction on how to operate the microscope.

5.1. Experiments

HeLa cells were cultured on coverslips with adhesive MPs of four different shapes (●, ▴, H, Y) in three different sizes (small, medium, large). The different sizes should lead to average cell sizes of $700\text{ }\mu\text{m}^2$, $1100\text{ }\mu\text{m}^2$ and $1600\text{ }\mu\text{m}^2$ respectively [185]. After 4 h of incubation time cells were fixated on the coverslip and fibronectin, tubulin and DNA were fluorescently stained to visualize the micropattern, microtubules and the cell nucleus. The dyes used for staining were Cy3, Alexa 647 and Hoechst 33342 that have emission wavelengths in the yellow-green, red and blue part of the visible spectrum.

For imaging we selected cells that were in interphase (i.e. non-dividing), adhered individually on a micropattern and were spread out to the full extend allowed by the pattern geometry. Although the micropatterned substrates enforce spatial boundary conditions on the cells and enable shape normalization, many cells had to be discarded. This is due to non-occupied micropatterns, incomplete adhesion, multiple cells populating the same micropattern, mitotic (dividing) cells or apoptotic (dying) cells. The micropattern shape as well as its size influence the yield and HeLa cells tend to favor medium or large-sized micropatterns, while the least well-adhering cells were found on the Y-shaped pattern. Cells on the ●-pattern were not considered for further analysis, because here no SFs are present that span over non-adhesive parts of the surface.

From a block of 12×12 micropatterns we found approximately 15 cells suitable for later analysis ($\approx 10\%$ yield), which is consistent with the yield we found in Chapter 6 using the same substrates.

According to the resolution limit for confocal microscopes (Section 1.1) we assume a maximally achievable lateral resolution of $d_{\text{lateral}} \approx 200\text{ nm}$ and $d_{\text{axial}} \approx 600\text{ nm}$ in the axial direction. In our imaging setup the voxelsize of the confocal stack was set to $120\text{ nm} \times 120\text{ nm} \times 250\text{ nm}$. The sampling frequency does not reach the theoretical resolution limit, but is reasonably close.

The images were deconvoluted using the software package Huygens (Scientific Volume Imaging) to minimize the effects of the extended PSF and to improve image resolution. For further analysis, the slice from the Z-stack that showed the highest contrast of the MT network was selected in order to have the most important structural features present in a

single image. Usually the plane of this image was close to the coverslip.

5.2. Analysis

The purpose of our study was to investigate the organization of the MT network inside a cell with a predefined shape. The diameter of MTs, of approximately 25 nm, is below the resolution limit of conventional microscopes and one would need super-resolution techniques like STED or PALM to fully resolve individual MTs [186]. In practical approaches it has been shown that individual MTs can be extracted even from fluorescent images recorded with conventional microscopes if they are sparse and not intersect other MTs [187, 188]. Another approach is to use a fluorescent marker for the plus-end binding protein EB1 and reconstruct the track of a growing MT from time lapse recordings [35]. We only had access to static images of the MT network and could not segment individual filaments due to the high density of the MTs.

To investigate the cell-wide organization of the MT network, we extracted the local orientation of the MTs from the structure tensor, as introduced in Section 2.4. We chose width of the Gaussian derivative kernel as $\sigma = 1 \text{ px} = 120 \text{ nm}$ and correspondingly the width of the windowing function as 2σ .

Order parameter

Spread in a distribution of angles can be quantified by the circular variance (Eq. (2.18)). Another way of to measure such a spread is to define an order parameter S equivalent to the one used in the theory of liquid crystals (Chapter 9):

$$S = \langle 2 \cos(\bar{\vartheta} - \vartheta_i)^2 - 1 \rangle . \quad (5.1)$$

Here, $\bar{\vartheta}$ is the average angle obtained by calculating the circular mean (Eq. (2.17)), ϑ_i are the samples of the distribution of angles and $\langle \dots \rangle$ denotes the arithmetic mean. The order parameter S ranges from $S = -1$ (purely orthogonal orientation w.r.t. $\bar{\vartheta}$) over $S = 0$ (isotropic distribution of ϑ_i) to $S = 1$ (parallel or anti-parallel alignment of the ϑ_i with $\bar{\vartheta}$).

For angular variables distributed over the interval $[0, 2\pi)$ Eq. (5.1) cannot distinguish between parallel and anti-parallel orientations, but for angles in the interval $[0, \pi)$ it is a reasonable definition.

5.3. Results and discussion

After image registration with the procedure outlined in Section 2.1, the MT network was extracted by segmenting the tubulin channel of the slice with the highest contrast using a K-Means-based algorithm (Section 2.2). From the segmented images we extracted the local orientation of the MT network from the structure tensor.

To obtain an average orientation field of the MT network, the fields of all recorded cells for each MP type were averaged with the structure tensor coherency c (Eq. (2.15)) as a weight for the averaging procedure. The local orientation ϑ extracted from the structure tensor is defined in the interval $\vartheta \in [0, \pi)$. The circular mean defined in (Eq. (2.17)) assumes 2π periodicity and to account for the π periodicity of our data we need to calculate the circular mean of 2ϑ and divide the result by 2 to obtain the average orientation field.

Fig. 5.2 shows the experimental orientation fields of three different MPs (∇ -shaped, H-shaped, Y-shaped) for a representative single cell (a), as an average over all single orientation fields (b) and the order parameter calculated according to Eq. (5.1) (c).

By examining the individual images and the corresponding orientation fields (Fig. 5.2a), it becomes evident that the cell's nucleus covers a large fraction of the total cell area and therefore has a strong influence on the organization of the MT network. Although MTs can slightly deform the nucleus during interphase [189], they usually cannot penetrate the nuclear envelope and will thereby be aligned or deflected during growth. Due to these deformations inside the region covered by the nucleus, the MT orientation is very irregular. The presence of the nucleus translates into non-smooth averaged orientation fields with a low order parameter S in the center of the cell (Fig. 5.2b).

The centrosome is located close to the nucleus, near the cell centroid [35] and its position can usually be estimated by finding the brightest spot in the tubulin image if no staining is available. Near the centrosome, we expect local radial ordering of the MTs, but in the single cell images the alignment is not easy to extract. Due to the very high local MT density, the local orientation is not well defined.

These two systemic effect would still be an issue if the number of cells would be increased, because nucleus and centrosome are always located close to the cell center. A larger MP size or cells with a smaller nucleus relative to their total size might decrease the zone of non-smooth orientation fields near the cell center, but it cannot be made arbitrary small.

Between the nuclear envelope and the convex, adhesive edges of the cell we find a radial configuration of the MT network in single cell images and averaged orientation

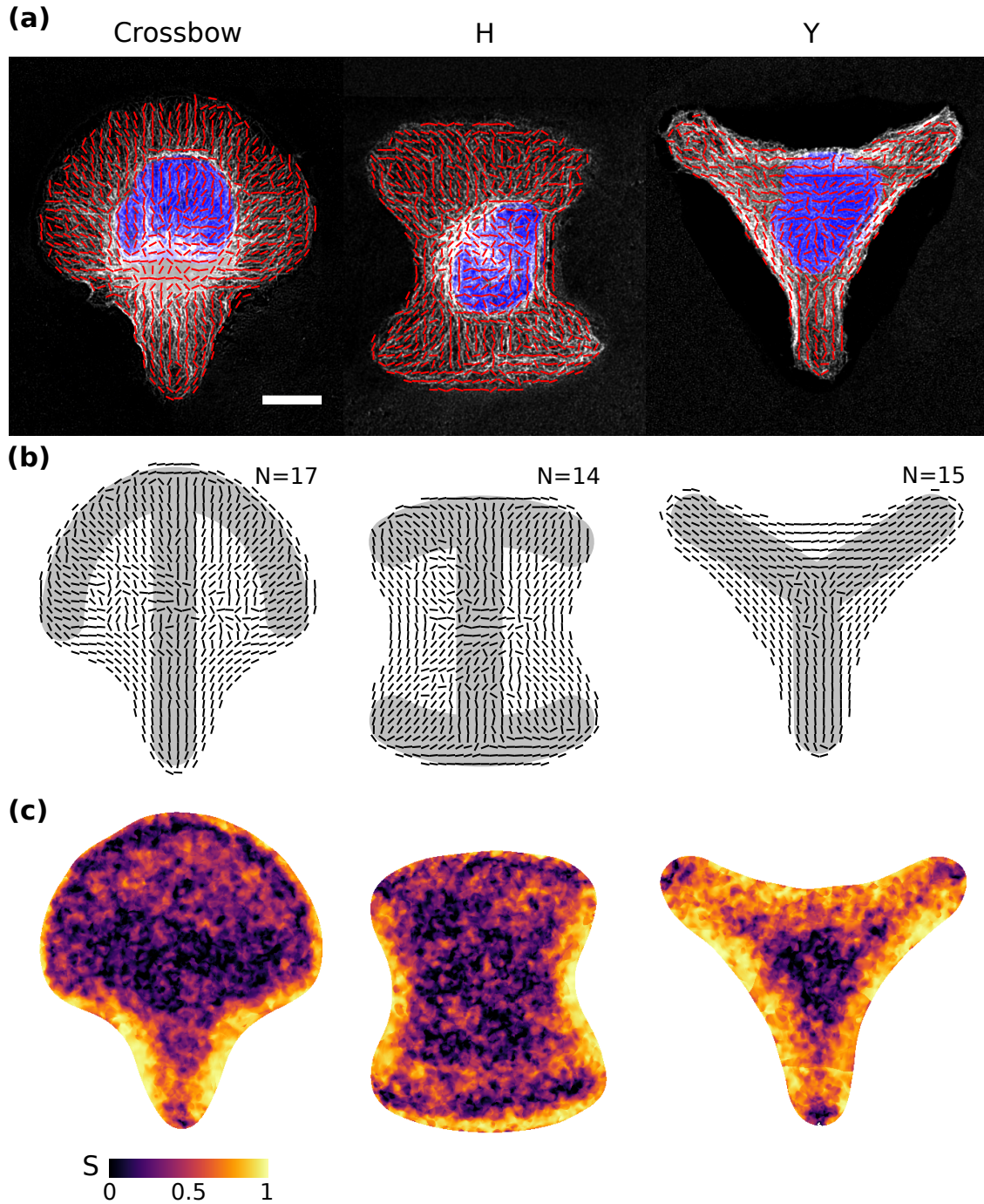


Figure 5.2.: Analysis of the MT network inside a cell with predefined shape. **(a)** Fluorescent micrographs of the MT network (gray-scale) with the corresponding local orientation (red bars) and the nucleus (blue). Plots show individual cells on three different MP geometries (∇ large, H medium, Y medium) **(b)** Averaged orientation field with MP geometry in the background (gray). **(c)** Order parameter of the orientation fields according to Eq. (5.1).

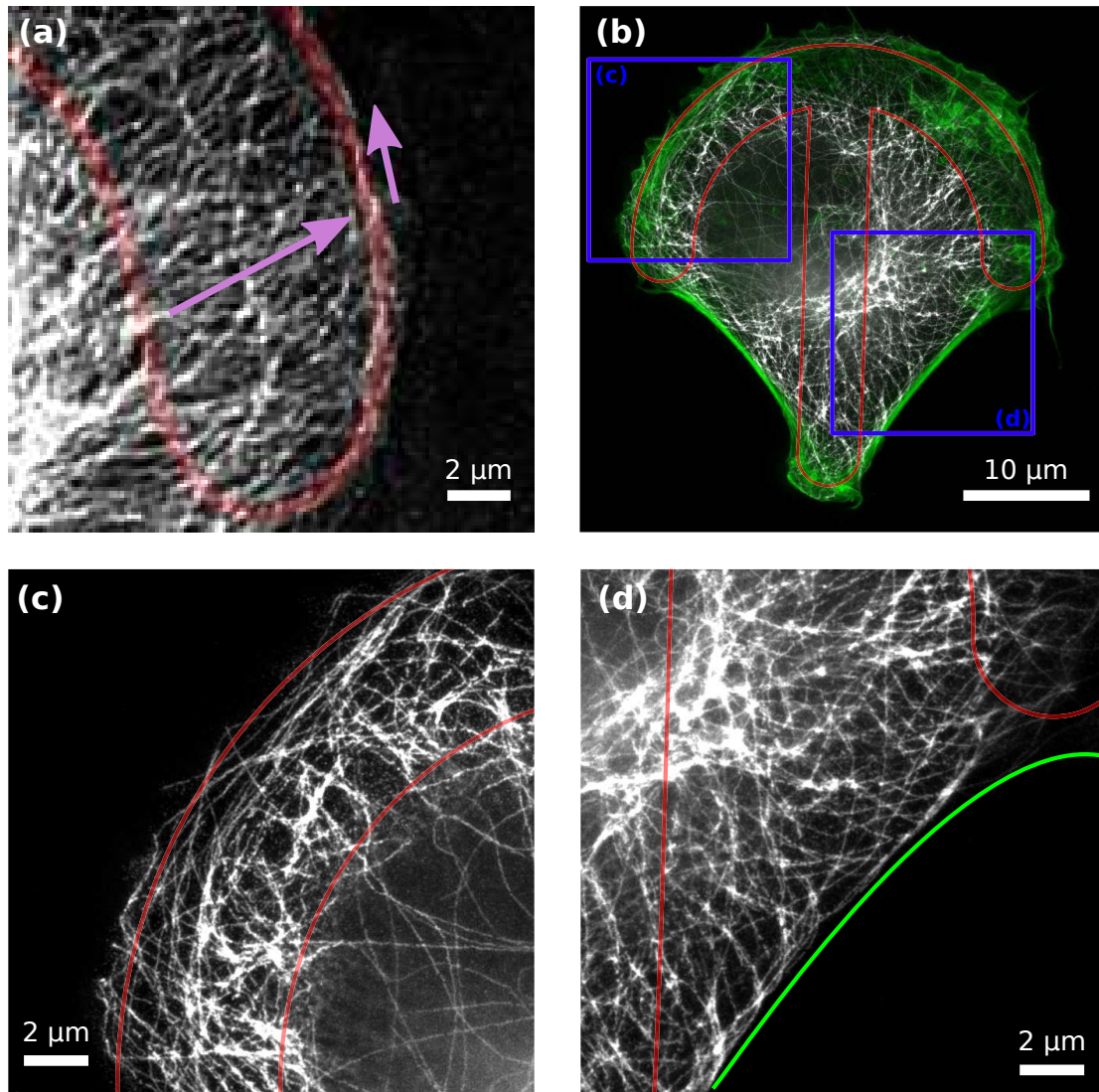
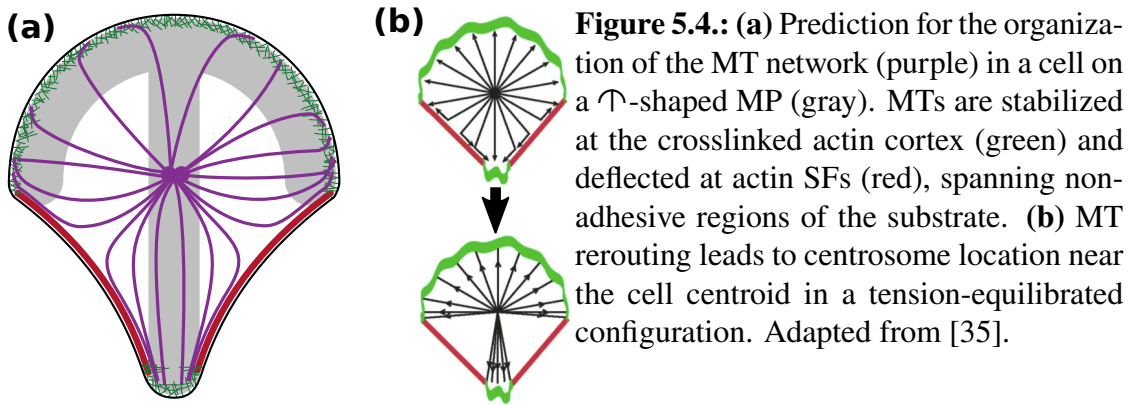


Figure 5.3.: Coordination of the MT network at the cell boundary. **(a)** Confocal image of MTs that grow radially towards the cell boundary (large arrow) and align tangentially at the cell cortex, very close to edge (small arrow) of the MP (outline in red). **(b)** STED image of the MT network (grayscale) and the actin CSK (green). MP was not imaged and position is estimated. **(c)** Zoom into the convex boundary of the cell in (b) also shows tangential alignment of the MT network close to the boundary of the cell. **(d)** Zoom into the concave boundary of the cell shows deflection and tangential alignment of MTs at the SF (sketched in green).

fields. Near the cell cortex, very close to the membrane, a deviation from the radial configuration can be found in some cells and MTs tend to align tangentially with the boundary (Fig. 5.3a). To investigate this effect further, we had access to one image of a cell on a ∇ -shaped MP imaged by STED microscopy (Fig. 5.3b). The images was

recorded by Johann Engelhardt in the group of Stefan Hell (DKFZ, Heidelberg). In this super-resolution image, actin and tubulin were stained and the position of the adhesive MP had to be inferred from the shape of the actin CSK. Near the convex parts of the cell boundary, we again observe local tangential alignment and radial orientation of the MT network in the central part of the cell (Fig. 5.3c). The effect of MT deflection and bending at the concave boundaries is very obvious in the super-resolution image (Fig. 5.3d).

At the concave boundaries of the cells, where actin SF form, we find tangential orientation on the level of individual cells and in the averaged orientation fields. The region of tangential alignment in the averaged orientation fields extends further inwards than one would expect from a local deflection of growing MTs. The two main reasons for this discrepancy are the variation of the radii of curvature of the actin arcs and a localization of the nucleus close to the actin arcs. Variability in the localization of the actin arcs will distribute the band of local tangential alignment over a larger region in the averaged fields. If the nucleus is positioned close to the membrane, its alignment properties mentioned earlier will also broaden the region of tangential orientation.



Our experimental findings and previous observations [35] lead to a prediction of the organization of the MT network in cells on MP substrates as it is shown in Fig. 5.4a. Compared to the earlier findings, we also found local tangential anchoring at the convex boundaries near the cell cortex. Outside of this band of $\approx 2\mu\text{m}$ at the convex edges, the MT network orients radially w.r.t. the cell center. The tangential alignment might be caused by more detailed interactions between MTs and the actin cortex than a simple capping of growing MTs. Similar crosslinking proteins or molecular motors as for the interaction between SFs and MTs could influence the orientation of the MT network near the dendritic actin network of the cell cortex. The effect of such interactions might be different due to the different organization of the actin CSK and in the super-resolution image it is visible that only a fraction of the MTs show tangential alignment with the

cell outline. A functional role of the deflection of MTs at the concave boundaries is that it allows to retain a centered position of the MTOC, even if the cell is forced into an asymmetric shape due to the MP (Fig. 5.4b).

The sketch shown in Fig. 5.4a is an idealized version of the organization of the MT network for an averaged cell. Differences to our experimental results can be explained by the influence of the nucleus at the cell center and natural variability of the cells, which leads to invaginated arcs with different radii of curvature at the non-adhesive boundaries.

In future work, the image analysis method outlined above could be applied to larger numbers of super-resolution images to estimate the MT orientation. Alternatively, individual MTs could be tracked to analyze their shape in more detail. Furthermore, it would be interesting to study how the effects like the suppression of motor activity or depletion of crosslinking proteins influence the coordination of MTs and actin at the boundaries. Approaches for this have been discussed in [97].

Analysis of intracellular integrin accumulation in cells on micropatterns

Micropatterned substrates not only reduce CSK variability by cell shape normalization, but also induce more regular arrangements of the intracellular compartments. The centrosome, the Golgi complex and the nucleus localize close to the cell's centroid as was discussed in Section 1.2.1. The normalization properties of MP substrates make it possible to calculate characteristic vesicle density maps for a given cell shape and [190] and study the influence of cytoskeletal disruption due to different chemical compounds in a standardized way [191, 192].

In this section we present an image analysis method to study the spatial distribution intracellular vesicles. Conventional screening approaches are usually conducted on substrates with homogeneous coating of ECM proteins. This leads to high a variability in cell shape and differentiating between individual cells might be difficult. Due to this effects, image analysis and determination of screening hits is often limited to the perinuclear region [193, 194]. With these methods, changes in the spatial distribution are difficult to assess and the variability in cell shape requires very high cell numbers to perform meaningful analysis. The methods we present utilize the normalization properties of MP substrate to obtain significant results with fewer cells.

We will apply the developed techniques to a proof-of-principle screen with small interfering RNA (siRNA) mediated knockdown of genes that influence integrin endocytosis. As was discussed in Section 1.5, integrins are important transmembrane molecules and are involved in numerous cellular signaling processes and diseases such as cancer. This

makes them especially interesting to study from a molecular biological as well as a clinical point of view, but also a better understanding of their involvement in FA regulation and cell migration is attractive to the biophysics community.

The work presented here was done in collaboration with the groups of Vytaute Starkuviene-Erfle and Holger Erfle at BioQuant, Heidelberg University. The experiments were conducted by Susanne Reusing and Gintare Garbenciute and imaging was performed by Manuel Gunkel. The image analysis methods were developed in collaboration with Philipp Albert from the Schwarz group.

6.1. Spatial distribution maps for intracellular compartments

The normalization of cell shape on micropatterned substrates allows to align multiple cells and compute average density maps of intracellular vesicles by locating individual endomembrane positions [190]. Based on individual positions, statistical tests can be applied to identify changes in the distributions [195]. To be able to extract positional information, images with high spatial resolution, i.e. high magnification, have to be obtained, which limits the field of view to only a few or even single cells. In large-scale screens usually lower magnifications are used in order to capture a larger fraction of the coverslip in a single image. Therefore, the localization of individual endomembrane is a difficult task and measurements of spatial fluorescent intensity profiles provides a good trade-off between imaging effort and precision of the analysis.

We developed a framework in which a stack of prealigned micrographs of cells adhering on a micropattern can be analyzed by defining radial bins that adapt to the shape of the cell and allow us to compute average intensity profiles of fluorescently labeled endomembranes. For the generation of the bins, we used the centroid of the average cell shape as the origin. We defined a fraction of the radius from the centroid to cell outline to be covered by circular bins (here: 25%) and split the rest of the radius into a predefined number of bins (Fig. 6.1a). The distance r of the bin from the cell center is defined as an azimuthal average over the distance of the bin center to the cell centroid.

An advantage of using bins that adapt to the shape of the cell is that they have the potential to capture processes that are under the influence of cellular morphology with higher precision. One example is the distribution of endomembranes that are localized close to the outline of the cell. Here, a circular bin geometry, like in Fig. 6.1b, would

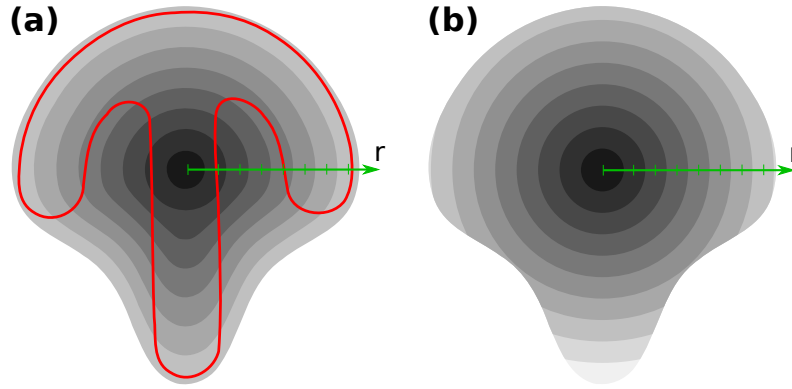


Figure 6.1.: Definition of radial bins for a cell on a \mathcal{T} -shaped MP (red). **(a)** Bins with continuous adaptation to cell shape. **(b)** Concentric circular bins with equidistant spacing.

split up such a distribution into 5 different bins. This might lead to an overlay with effects that are located more in the center of the cell. An adaptive bin-shape can capture such a distribution in a single bin located around the outline of the cell and will therefore allow for a more precise quantification.

6.1.1. Assessment of statistical significance

To address statistical significant differences between experimental conditions, i.e. negative control and siRNA mediated knockdown, we used the non-parametric k-sample Anderson-Darling test [196] and its implementation in the kSamples package [197] of the statistics software R. The null hypothesis of this test is that all the samples to be compared have been drawn according to a common unspecified probability distribution. At a significance level $p < 0.05$ we reject this null hypothesis and assume the alternative hypothesis that the samples arose from different distributions. The choice of this test is based on the observation that the binned intensity distributions as well as the distribution of mean cellular intensity were skewed to higher intensity values and the commonly used Student T-test assumes that the samples follow the normal distribution. To assess if the average intensity of one of the distributions is higher or lower than the other one, the median values of each distribution will be compared.

6.2. Experimental procedure

The RNAi mediated knockdown of gene expression was conducted by transfecting HeLa cells, a human, endothelial, cancer cell line, with 5 different siRNAs. The expression of

Dynamin-2 (encoded in the DNM2 gene), Kinesin family member 15 (KIF15 gene), Disabled homolog 2 (DAB2 gene), Clathrin heavy chain 1 (CLTC gene) and Caveolin-1 (CAV1 gene) was inhibited. As a control measurement, cells were transfected with the AllStars negative control siRNA that has no homology to any known mammalian gene [198]. CLTC, DNM2 and DAB2 are known for their importance in the formation of clathrin coated pits that develop into membrane buds and their fission into vesicles [110]. Caveolin is involved in a clathrin-independent endocytotic pathway by forming invaginations of the plasma membrane. Here, DNM2 is also important for the fission of those invaginations into vesicles [110]. KIF15 is a MT plus-end directed motor and involved in the recycling of intracellular integrin to the cell membrane [194].

For the proof-of-principle screen, CYTOO starter chips [185] with four different micropatterns (●, ∩, H and Y-shaped) were used similar to the experiments for the organization of the MT network in Chapter 5. We selected the medium sized micropattern with a reference cell size of 1100 μm , because this pattern size had the highest yield of cells suitable for analysis.

The experiments were conducted with HeLa cells, because of their good response to RNAi [194]. After transfection with different siRNAs, the cells were seeded onto the MP substrate to allow for attachment and normalization of shape as well as integrin endocytosis. Non-internalized membrane bound integrin was washed away before fixating the cells, such that only intracellular integrin will be fluorescently labeled.

After imaging, cells suitable for further analysis were selected based on the criteria that they were adhered individually on a micropattern, were non-mitotic and had spread out to the full extend allowed by the micropattern geometry. In some cases cells with a very low average intensity had to be removed, because they were almost indistinguishable from the background intensity level. This is most likely caused by dysfunctional endocytosis of some cells, which is common for cancer cells [199].

The experiments were performed on different days with potential variations in fluorescent staining efficacy or changes to the microscope settings. For this reason we performed background estimation for each experiment separately by computing the average background intensity over all cells selected for analysis.

6.2.1. Validation of the experimental setup

To validate our analysis method and also the experimental procedure, we checked for overlap in the normalized intensity distributions of the control experiments. For this, the fluorescent micrographs of stained integrin $\alpha 2$ were divided into bins that follow the

shape of an averaged cell (Fig. 6.1a). To make sure that the spatial distribution was not superimposed by variations in absolute intensity levels, due to variability in the experimental conditions, the total fluorescent intensity of each cell was normalized to 1 before averaging.

While the absolute intensity distributions for varied for different experiments, the normalized intensity distributions agree (Fig. 6.2). For all four MPs used, the k-sample Anderson-Darling test for each bin separately and we found no statistical significant difference between the control experiments.

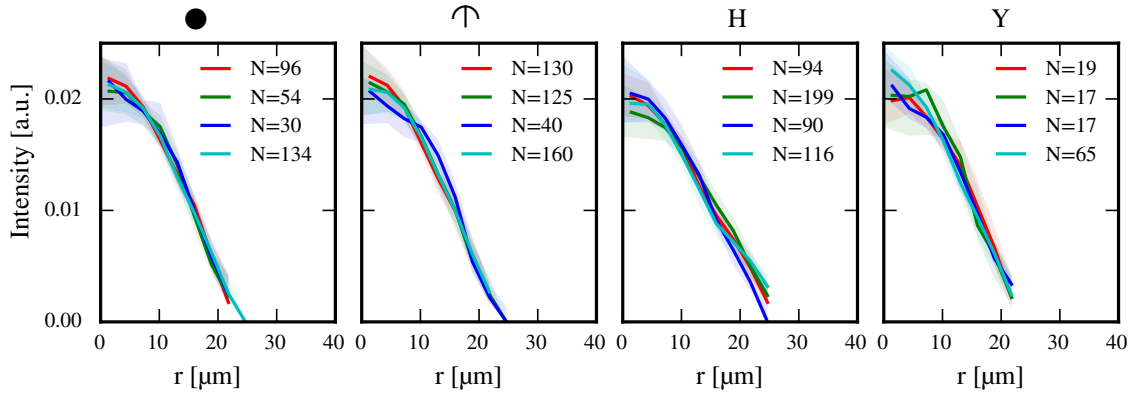


Figure 6.2.: Comparison of normalized intensity distributions for experiments with the AllStars negative control siRNA for all four MPs. Bins were created as in Fig. 6.1a, centered at the cell centroid. Horizontal axis represents the average distance of the bin center from the cell centroid. Intensity distribution of each cell was normalized before averaging. Colored curves correspond to different dates. Bold lines are median values, shaded regions represent 25% and 75% percentiles. N is the number of cells.

6.3. Influence of knockdown on cell-wide integrin accumulation

As a first step to assess the influence of the siRNA mediated knockdown, we checked for differences fluorescence intensity on the level of a complete cell. We found statistically significant differences in the distribution of cell-wide mean intensity for the majority of MP and knockdown combinations.

In the following, we will focus on two knockdowns on two MPs to illustrate the effect RNAi. In Fig. 6.3 box plots of the distribution of the averaged cellular intensity are shown for the the ●-shaped MP and the ⊥-shaped MP with knockdowns of the DNM2 gene and the CAV1 gene. The distributions are tested against the AllStars negative control

siRNA (CTRL) and, except for a knockdown of CAV1 on the ●-shaped MP, we found no statistically significant differences in the distributions. Evaluating based on the median values, we found that DNM2 knockdown decreases intracellular integrin accumulation and CAV1 knockdown increases the amount of internalized integrin in the ∇ -shaped MP.

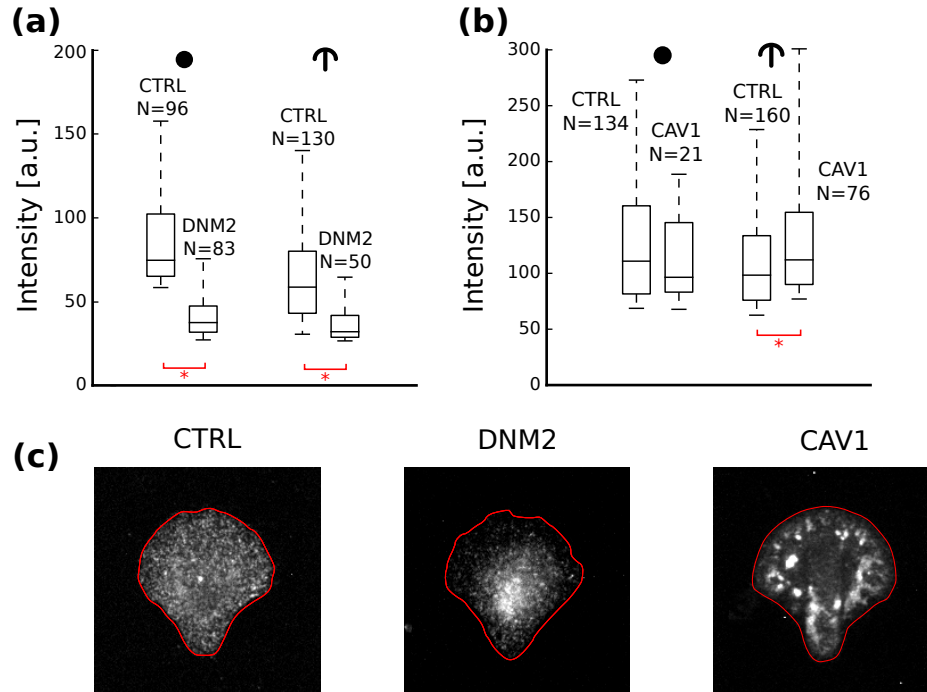


Figure 6.3.: (a) Box plots of the mean cellular intensity for cells on the ●-shaped MP and on the ▽-shaped MP. Comparison is for the AllStars negative control siRNA (CTRL) and a knockdown of the DNM2 gene. Boxes extend from the 25% percentile to the 75% percentile with the median marked by a vertical line. Whiskers (dashed) represent 5% and 95% percentiles. Statistical significance is marked by an asterisk. (b) Same comparison as in (a), but for a knockdown of the CAV1 gene. (c) Typical examples of cells from the control experiments and the two knockdowns with outline of the segmented cell (red).

In Fig. 6.3c typical examples of cells of the different experimental conditions are shown and one can clearly see the effect of the knockdowns. For a DNM2 knockdown intracellular integrin is located more pericentral, while for the CAV1 knockdown larger clusters form, which are located peripherally.

6.4. Changes in the spatial distribution of internalized integrin

From observing the different phenotypes shown in Fig. 6.3c, we expect not only changes in the absolute levels of accumulated intracellular integrin, but also differences the spatial distributions. Just as the for comparison of the different control experiments, we calculated spatial intensity distributions by the method outlined above and used bins that adapt to the shape of the cell. The mean intensity of each cell was normalized to 1 before the averaging procedure.

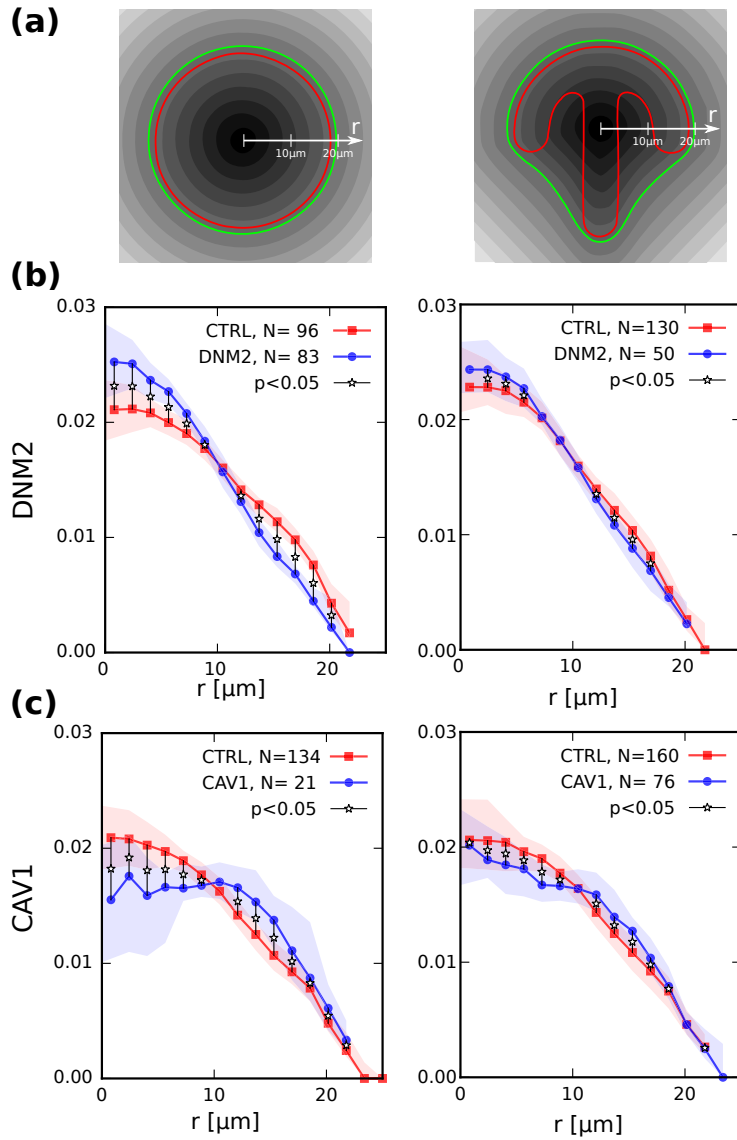


Figure 6.4.: Spatial intensity distributions of internalized integrin. (a) Radial bins for the ●-MP and the ∇-MP. (b) Median values of binned intensity distributions for the knockdown of DNM2 (blue) are compared to control measurements with AllStars negative control RNAi (CTRL, red). Shaded areas represent 25 and 75 percentiles. Statistically significant differences in the binned distribution are marked with an asterisk. (c) Comparison of the intensity distributions for CAV1 knockdown to control measurements.

Fig. 6.4 shows this binned intensity distributions for the cells on the ●-MP and the ∇

-MP. For DNM2 knockdown (Fig. 6.4b), we found that the normalized intensity distributions are increased in the pericentral region and are decreased in the peripheral regions, compared to the control experiments. This indicates that DNM2 not only inhibits the accumulation of integrin in the cell, but it also shifts the distribution more to the cell center. Except for a region of $r \approx 10 \mu\text{m}$, where the two curves intersect, the binned distributions are significantly different at the 0.05 level. The distributions within each bin were tested separately. A knockdown of CAV1 induces the reverse effect. Here, we observed a lower normalized intensity of the knockdown experiments in the pericentral region and higher values in the peripheral region (Fig. 6.4c).

The observed effect can be caused by a combination of the lower expression levels due to RNAi and the MP geometry. On the ∇ -MP both changes in the distribution are less pronounced. This is an interesting point to investigate in further studies, by comparing concave micropatterns, such as the ∇ , with counterparts that provide a completely filled adhesion geometry where the cell does not span over nonadhesive parts of the surface.

6.5. Conclusion

In this chapter we presented methods for the analysis of small intracellular compartments. The usage of MP substrates intracellular organization and allows us to study how such compartments distribute spatially and to assess changes in the distributions with statistical tests. As a proof-of-principle, we applied the method to various knockdowns of genes that influence the endocytosis of integrin and showed the differences of a knockdown of Dynamin-2, compared to a knockdown of Caveolin-1. Our method can be directly applied to low resolution images and differences in the distributions due to siRNA mediated knockdown can be assessed with less effort than in previous screens.

Part II.

Modeling

Modeling of the microtubule network

Although imaging and image analysis are very powerful tools for biophysical research, they are sometimes limited by the sheer effort it takes to perform experiments. Due to biology's high complexity, the study of changes in cell behavior upon variation of the experimental conditions is often a very hard task. Here, theoretical models and computer simulations significantly extend the toolbox available to researchers. By systematically reducing the complexity during model formulation, the most basic mechanisms that underlie experimental findings can be figured out. This then helps to design new experiments to investigate the influence of those basic mechanism in real systems.

In this second part of the thesis we continue to investigate the organization of the MT network inside cells with predefined shape. This time we use computational modeling. Our model assumptions are based on the experimental study of the MT network in Chapter 5. There, we found support for earlier experimental observations of how the MT network interacts with the actin CSK [35] and made novel observations of MT behavior close to the cell cortex. A reminder of the predicted layout is given in Fig. 7.1.

The underlying hypothesis for all of the following models is, that the organization of the MT network is mainly determined by interactions with the actin CSK at the cell boundaries. Based on our experimental findings, we expect qualitatively different behavior at the convex and concave parts of the cell due to the different organization of the actin CSK. At the convex part of the boundary we hypothesize that the growth of MTs is halted, for example due to capping of the plus ends [200]. There, also a local deflection of the MTs can occur, which leads to tangential alignment of the MTs in the immediate vicinity of the cell boundary. Invaginated SFs that contribute to concave regions of the cell outline will lead to different arrangement of the MTs. Here, deflection or guidance towards the adhesive parts of the substrate occurs, which is mediated by steric interactions or by molecular

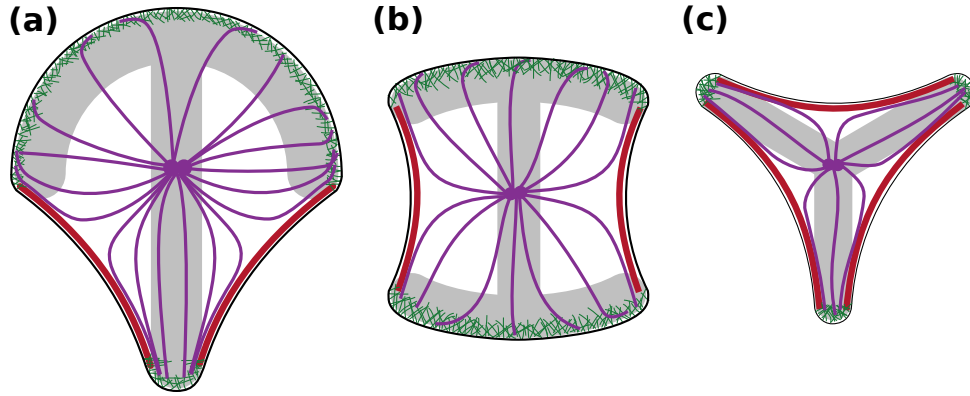


Figure 7.1.: Predictions of the layout of the MT network (purple) in cells on MPs (gray). MTs are stabilized at the actin cortex (green) with local tangential alignment at the convex boundaries and are deflected at the SFs (red). (a) \top -shaped MP, (b) H-shaped MP, (c) Y-shaped MP.

motors and crosslinkers acting behind the MT tip [97].

Neglecting CSK crosstalk away from the cell periphery is certainly a strong assumption and multiple experimental studies suggest that MTs are deformed when they grow inside the actin CSK [90, 91] (Section 1.4.4). These interactions will lead to short wavelength deformations of the MTs on the order of $\approx 3 \mu\text{m}$ and have been quantified by an effective filament persistence length of $l_p^{\text{eff}} \approx 30 \mu\text{m}$. This is two orders of magnitude lower than the persistence length of MTs if they are only subject to thermal fluctuations and can certainly not be neglected. Growing MTs are likely to be bent either during growth by interactions with the other components of the CSK or by the activity of molecular motors inside the CSK, which induces the aforementioned short wavelength deformations [91].

Recently, Frey [201] developed a model for MT growth inside a fixed actin mesh with biologically motivated interaction rules [95, 202]. One result was that the mesh geometry proved to be irrelevant for the deformations of MTs and the detailed interactions could be incorporated into a reduced effective persistence length. The reduced effective persistence length could be linked to the density of the AFs, i.e. the mesh size, and biologically plausible mesh size led to a reduced effective persistence length of the MTs of $l_p^{\text{eff}} \approx 30 \mu\text{m}$, which agrees with *in vitro* experiments.

Another assumption we make is that the cell nucleus does not influence the organization of the MT network. Obviously this assumption is hard to justify, but if we consider our models as effective descriptions, valid for an average of many cells, we can nevertheless use them to make predictions for the organization of the MT network. By utilizing MP substrates for normalization of cell shape and internal structure, comparison between

experiments and model predictions becomes feasible.

The second part of this thesis is organized as follows. First, we will give an overview of established models for the cytoskeleton. As a preliminary for the discussion of the models we propose, we discuss how to compare modeling outcomes to either experimental results or to other models. In Chapter 8 we introduce two computational models that are based on the simulation of individual growing filaments and we introduce boundary interactions based on experimental findings. In Chapter 9 we model MT organization in terms of an effective continuum theory for liquid crystals, in which we define a free energy functional and minimize it with the finite element method to find the corresponding minimum energy configuration. All of the models will be compared to the experimental findings and also to each other.

The results of the modeling part, in combination with the findings presented in Chapter 5, and the model for MT interaction with AF developed by Felix Frey from the Schwarz group, will be published in a combined paper.

7.1. Models for cytoskeletal organization

Due to the high complexity of the CSK, a thoroughly theoretical description of it as a whole is an extremely difficult, if not impossible task. Even if all the molecular interactions and reaction networks relevant for the CSK would be known, which is the case only for the simplest organisms like yeast [203], one would still have to bridge length and time scales ranging from a few nanometers and nanoseconds for the polymerization dynamics of the CSK filaments up to micrometers and hours for the evolution of the filament networks [204].

For all the mentioned length and time scales detailed models exist, ranging from molecular dynamics simulations of the MT structure [205], over models for molecular motor activity [206, 207], descriptions of polymer mechanics, and models for crosslinked polymer networks [208], to continuum descriptions, such as the active gel theory [209].

Simple models for the semiflexible cytoskeletal filaments start with the wormlike chain (WLC) model [210] (cf. Section 8.1), with mechanical properties, such as elasticity and the force extension curve can be described. Such WLC models can also be combined to bundles to study their mechanical properties [211].

There are numerous models to investigate the mechanical properties of crosslinked polymer networks [208] and the simplest numerical approaches for generating such networks are Mikado models, where filaments are distributed randomly and crosslinked at

their intersection [212, 213]. Such simple approaches can be extended by modeling the individual filaments as WLCs and use Monte Carlo methods to find network configurations that minimize the free energy [214].

Alternative approaches for dynamic simulations of discrete CSK components are often based on Langevin-type equations, where the velocities of filament segments or other CSK components are proportional to incident forces, such as viscous drag, thermal forces, bending and twisting torques and others [215]. Bending elasticity of the semiflexible polymers can be modeled with WLC Hamiltonian. One modeling framework that implements Langevin dynamics for cytoskeletal filaments is Cytosim [216]. Its underlying principles will be discussed in more detail in Section 8.2. Models of this type have been used to study the formation of MT vortices [217] or interaction of AFs [218].

Experimental studies for cytoskeletal organization often start from simplified extracts of the CSK, like mixtures of MTs [219] or AFs [220] with molecular motors, but self-organization effects can also be observed *in vivo* [221]. Also steric interactions of filament can influence cytoskeletal organization [222].

For continuum descriptions, the mixture and of filaments and molecular motors that constitute the CSK can be seen as a viscoelastic material that is driven out of equilibrium by ATP hydrolysis [223]. In the active gel framework [209, 223–225], a hydrodynamic theory of a polar liquid crystal is extended by active contributions due to ATP consumption. Linear relations between the fluxes mechanical stress, rate of change of the polarization, and rate of ATP consumption and their generalized forces are sought. These are the velocity gradient, the orientation field and the free energy gained by ATP hydrolysis [224].

The active gel theory has been used to understand the pattern formation of asters and vortices [226] or to investigate changes in the actin CSK in response to differences in substrate stiffness [227]. The contractile effects of the active gel theory can mainly be found in acto-myosin–systems, but elements of this theory have been used to study the alignment of MTs in the mitotic spindle [228]. Recently it was shown *in vitro* that MT networks can exhibit contractile behavior as well, and active gel theory has been applied to such systems [229].

One of the underlying principles of the description of active gels is the theory of liquid crystals [230]. It enters the description through the free energy functional of the polarization field. We will use the theory of nematic liquid crystals in Chapter 9 for modeling the MT network. There, we will also discuss the free energy functional in more detail.

Apart from effects like the orientation of CSK filaments and contractility of filament-

motor–mixtures, it is of interest of how the CSK influences intracellular organization. Here, especially the positioning of the centrosome and its MT aster has been studied by discrete models of polymerizing filaments and motor interactions [231], in terms of a continuum theory [232], or a combination of both [233].

Although crosstalk between cytoskeletal components is an established concept, not many models consider explicit interactions between cytoskeletal filaments. There are some studies dealing with MT-actin coordination in neuronal growth cones [234] or in plant cells [202] or mechanical properties of MTs connected to AFs [235]. Recently, deflection processes of MTs growing in a static network of AFs were studied [201], which were motivated by recent experimental findings of MTs interacting with actin bundles by engineered crosslinking proteins [94]

7.2. Boundary definition and analysis of the proposed models

Before the different approaches for modeling the MT network are discussed in the next chapter, we will make some preliminary definitions of how to compare their outcome to experimental results and also to one another.

As was shown in Fig. 7.1, we expect growing MTs to be deflected at invaginated actin arcs and to be anchored in convex regions of the cell boundary. From the cell outline Γ we can compute the convex hull $C(\Gamma)$ and define the convex parts Γ_1 and concave parts Γ_2 of the boundary by

$$\Gamma_1 = C(\Gamma) \cap \Gamma \quad (7.1)$$

$$\Gamma_2 = \Gamma \setminus \Gamma_1 . \quad (7.2)$$

For the two regions we expect qualitatively different interactions between growing MTs and the actin CSK. We will therefore treat Γ_1 and Γ_2 differently in all of the models (Fig. 7.2).

The outline of the cell used as the simulation domain can be extracted from experimental images by averaging over multiple cells and using the shape of such a cell as a reference. Alternatively, computational models, such as the cellular Potts model [119], can be used to predict the shape of adherent cells on MP substrates. The subsequent models can then predict the layout of the MT for a given geometry.

In the experimental analysis we determined the average orientation field as the relevant

quantity describing the organization of the MT network. To be able to compare the computational models for MT growth inside a cell with predefined shape, we need to calculate the average orientation field from a simulation of an ensemble of filaments. In contrast to the local orientation extracted from the structure tensor (Eq. (2.14)), which contains no directionality information, individual filaments are defined by a starting and ending point and thereby also the growth direction is set. Ultimately, all our computational models should be compared to the experimental findings. In order to make this comparison reasonable, we drop the directionality of the simulated individual filaments and consider only their orientation.

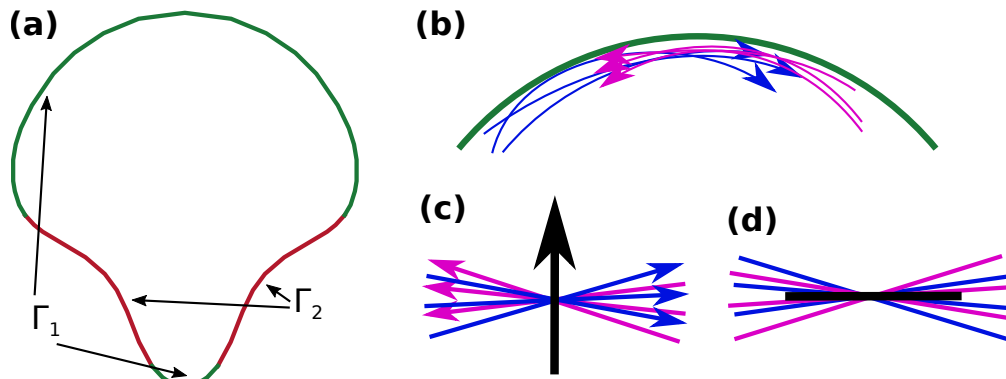


Figure 7.2.: (a) Boundary definition for a \mathcal{T} -shaped MP, split into convex parts Γ_1 (green) and concave parts Γ_2 (red). (b) Sketch of filaments oriented mostly anti-parallel towards each other. (c) Set of anti-parallel vectors (blue, magenta) and averaged vector (black) pointing approximately normal to the individual vector orientations. (d) Bars with same orientation as in (b), but without directionality. Average orientation is approximately parallel to the original bars.

For most scenarios it will not make a difference if one takes an average of vectors or oriented bars. In one important case however, the difference is significant. If many filaments grow anti-parallel or almost anti-parallel (Fig. 7.2b), an average taken over vectors will be approximately orthogonal to the filaments (Fig. 7.2c). In contrast, the average over oriented bars will be approximately parallel (Fig. 7.2d).

7.2.1. Comparison of simulated orientation fields to the experiments

The experimental results were evaluated on a predefined grid and we will apply the same grid to the simulated orientation fields to calculate the angle difference $\Delta\vartheta_i$ at each grid point i .

Similar to the order parameter defined earlier in Eq. (5.1) to measure the deviation of a population of angles from its average, one can define an order parameter \bar{s} that quantifies the similarity of two orientation fields as

$$\bar{s} = \frac{1}{N} \left(\sum_{i=1}^N 2 \cos^2 \Delta\vartheta_i - 1 \right). \quad (7.3)$$

Where the sum runs over all N grid points.

At this point we will bring forward a part of the comparison of the models to the experimental results, by considering a distribution $p(\Delta\vartheta)$ of angular differences that shows pronounced peaks at $\Delta\vartheta \approx 0$ and at $\Delta\vartheta \approx \pi/2$ (Fig. 7.3a). While the peaks at $\Delta\vartheta \approx 0$ and $\Delta\vartheta \approx \pi$ indicate that the experimental and simulated orientation fields coincide, the peak at $\Delta\vartheta \approx \pi/2$ indicates that a fraction of the population is oriented perpendicular to each other.

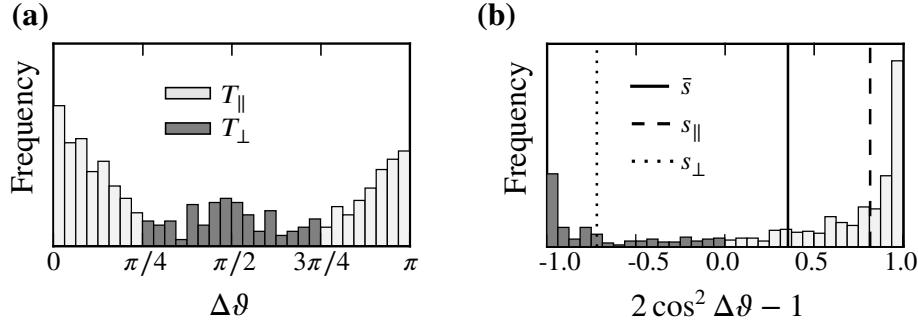


Figure 7.3.: (a) Histogram of the angular difference $\Delta\vartheta$ between an experimental MT orientation field and a simulated one. Set of more parallel angles $T_{||}$ (light gray) and set of more orthogonal angles T_{\perp} (dark gray) are shown. (b) Histogram of $2 \cos^2 \Delta\vartheta - 1$ for the same dataset. The distribution is bimodal with prominent peaks at ± 1 . Averages of the distribution are shown as \bar{s} for the full set T (solid line), $s_{||}$ for the set of more parallel angles $T_{||}$ (dashed line) and s_{\perp} for the set of more orthogonal angles T_{\perp} (dotted line).

The two peaks in $p(\Delta\vartheta)$ lead to a bimodal distribution of $s(\Delta\vartheta) = 2 \cos^2 \Delta\vartheta - 1$ with peaks at $s \approx \pm 1$ (Fig. 7.3b). The mean of a bimodal distribution as a single readout is not very meaningful and in this case, one cannot distinguish between two random orientation fields from two, with equally distributed parallel and orthogonal alignment. Both cases will yield $\bar{s} = 0$. We therefore split the set $T = \{\Delta\vartheta_i\}$ into two subsets

$$\begin{aligned} T_{||} &= \{\Delta\vartheta_i \mid \Delta\vartheta_i \leq \pi/4 \text{ or } \Delta\vartheta_i \geq 3\pi/4\} \\ T_{\perp} &= \{\Delta\vartheta_i \mid \pi/4 < \Delta\vartheta_i < 3\pi/4\}. \end{aligned} \quad (7.4)$$

Now,

$$s_{\parallel} = \frac{1}{N_{\parallel}} \left(\sum_{\Delta\vartheta_i \in T_{\parallel}} 2 \cos^2 \Delta\vartheta_i - 1 \right) \quad (7.5)$$

$$s_{\perp} = \frac{1}{N_{\perp}} \left(\sum_{\Delta\vartheta_i \in T_{\perp}} 2 \cos^2 \Delta\vartheta_i - 1 \right) \quad (7.6)$$

represent the order parameters of the more parallel or more orthogonal sets. N_{\parallel} and N_{\perp} are the number of elements in the corresponding sets.

The best agreement between two orientation fields would be a distribution of $s(\Delta\vartheta)$ that is strongly peaked at 1. Therefore, model parameters that yield a high value of \bar{s} will also provide good agreement with the experimental results. For low values of \bar{s} one should still check if this is caused by a bimodal distribution $s(\Delta\vartheta)$, i.e. $s_{\parallel} \approx 1$, $s_{\perp} \approx -1$, or by a flat distribution with $s_{\parallel} \approx 0.5$ and $s_{\perp} \approx -0.5$.

We do not expect perfect agreement between experimental and simulated orientation fields and a good match would be given for $\bar{s} \gtrsim 0.5$, $s_{\parallel} > 0.5$ and $s_{\perp} > -0.5$. In this case, the distribution $s(\Delta\vartheta)$ would be peaked to the right and T_{\perp} would be approximately flat.

Filament based models

Models of discrete filaments represent the most intuitive way of theoretically studying the CSK. Various levels of complexity are possible, ranging from random assemblies of rigid rods, also known as Mikado models, over the generation of filament configurations by simple stochastic processes, to large-scale simulations of dynamic, interacting, semi-flexible polymers. In this chapter we pursue two modeling approaches to investigate the organization of the MT network in cells with predefined shape. First, we generate MT growth trajectories by the stochastic simulation of a persistent random walk and in the second approach, we use the software Cytosim to set up a Brownian dynamics simulation of growing and shrinking MTs that interact with the cell boundaries.

8.1. Persistent random walk model

The WLC is a commonly used model to study semiflexible polymers. It can be defined via a Hamiltonian for the bending energy

$$\mathcal{H}_{\text{bend}} = \frac{\kappa}{2} \int_0^L \left| \frac{d\tau}{d\xi} \right|^2 d\xi. \quad (8.1)$$

The following discussion of the WLC follows [208]. If we restrict the WLC to a plane, the derivative of the integrand of Eq. (8.1) becomes $(\partial\vartheta/\partial\xi)^2$ with the angle ϑ of the chain. A discretized version of the integral is then $\sum_i (\Delta\vartheta_i)^2 / \Delta\xi$ and now $\Delta\vartheta_i = \vartheta_i - \vartheta_{i-1}$. We can assume that the $\Delta\vartheta_i$ are uncorrelated, because different thermal forces act on different parts of the filament. We use the equipartition theorem, from which follows

$$\langle (\Delta\vartheta_i)^2 \rangle = \frac{\Delta\xi k_B T}{\kappa}. \quad (8.2)$$

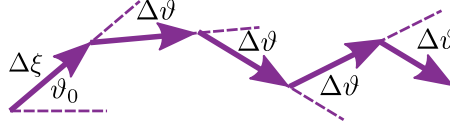


Figure 8.1.: Generation of growth trajectories by a persistent random walk. Line segments of length $\Delta\xi$ are joined according to the angular increment $\Delta\vartheta_i \sim \mathcal{N}(0, \sigma^2)$, which is drawn from a normal distribution. With the variance defined as $\sigma^2 = 2\Delta\xi/l_p$, a trajectory with a persistence length of l_p is generated.

Recalling the definition of the persistence length, now in 2D

$$l_p = \frac{2\kappa}{k_B T}, \quad (8.3)$$

we arrive at

$$\langle (\Delta\vartheta_i)^2 \rangle = \frac{2\Delta\xi}{l_p}. \quad (8.4)$$

This result states that the variance of the angle difference $\Delta\vartheta_i$ between two neighboring segments can be defined in terms of the segment length and persistence length.

By this result, we can now sample a WLC by a process by joining line segments of length $\Delta\xi$ and draw the angular increments $\Delta\vartheta_i$ from a normal distribution $\mathcal{N}(0, \sigma^2)$ with mean zero and variance $\sigma^2 = 2\Delta\xi/l_p$ (Fig. 8.1). The angle ϑ_n of line segment n is then given by

$$\vartheta = \vartheta_0 + \sum_{i=1}^{n-1} \Delta\vartheta_i, \quad (8.5)$$

$$\text{where } \Delta\vartheta_i \sim \mathcal{N}(0, 2\Delta\xi/l_p)$$

This process is a persistent random walk (PRW), which has a long tradition in biophysics, especially in the description of cellular motility [236, 237]. The outlined simulation procedure has also been used in [91, 201]. The PRW growth algorithm can easily be modified by stochastic switching between a state of growth and shrinkage to simulate the dynamic behavior of MTs.

We extend the PRW simulation to arbitrary, two dimensional environments with outlines described by polygons. Now, at each simulation step a check is performed if the filament tip intersects with the polygonal outline and what boundary interactions should be applied.

8.1.1. Boundary interactions

In experimental observations, MT growth stops at the convex parts of the boundary [35], which can be implemented in the PRW model by simply stopping the growth algorithm once a filament intersects a convex boundary. The PRW model does not include dynamic bending, because all the vertices of the chain are fixed in space. Therefore, bending of rigid fibers at the concave boundaries cannot be investigated. An indirect way of introducing deflection at the concave boundaries is to switch the MT to the shrinking state if it makes contact to such a boundary. The implications of such an interaction are discussed in the next section.

8.1.2. Partial versus complete depolymerization at concave boundaries

Upon contact with a concave boundary there are basically two options on how to proceed: Completely depolymerizing the MT by taking it out of the simulation and initializing a new filament or switching to a shrinking state with a non-zero rescue rate ω_r that allows the return to the growing state. The switching between states is simulated by a Poisson process with rate λ , for which the waiting time distribution for an event to occur is exponential [238]

$$p(t) = \lambda e^{-\lambda t} . \quad (8.6)$$

With rescue rate ω_r the expected waiting time before an rescue event is then simply given by $\langle \tau_- \rangle = 1/\omega_r$. With the shrinking velocity v_- one can estimate the average length lost due to a catastrophe at the concave boundary as

$$\langle l_- \rangle = \frac{1}{\omega_r} v_- . \quad (8.7)$$

With a depolymerization rate of $v_- \approx 0.26 \mu\text{m/s}$ and a rescue rate of $\omega_r \approx 0.064 \text{ s}^{-1}$ that were chosen according to *in vivo* measurements [239], we find an average length loss of $\langle l_- \rangle \approx 4 \mu\text{m}$. A full list of model parameters will be given in Appendix A.1.

There is a difference between complete depolymerization of the MTs compared to partial shrinking in the sense that the concave regions tend to locally deplete the filament density locally if the rescue rate ω_r is zero or close to zero. In Fig. 8.2a, b snapshots of a simulation of MTs are shown, with a reduced effective persistence length of $l_p = 30 \mu\text{m}$ and $l_p = 120 \mu\text{m}$, growing inside an outline that corresponds to the shape of a cell adhering on a ∇ -shaped MP.

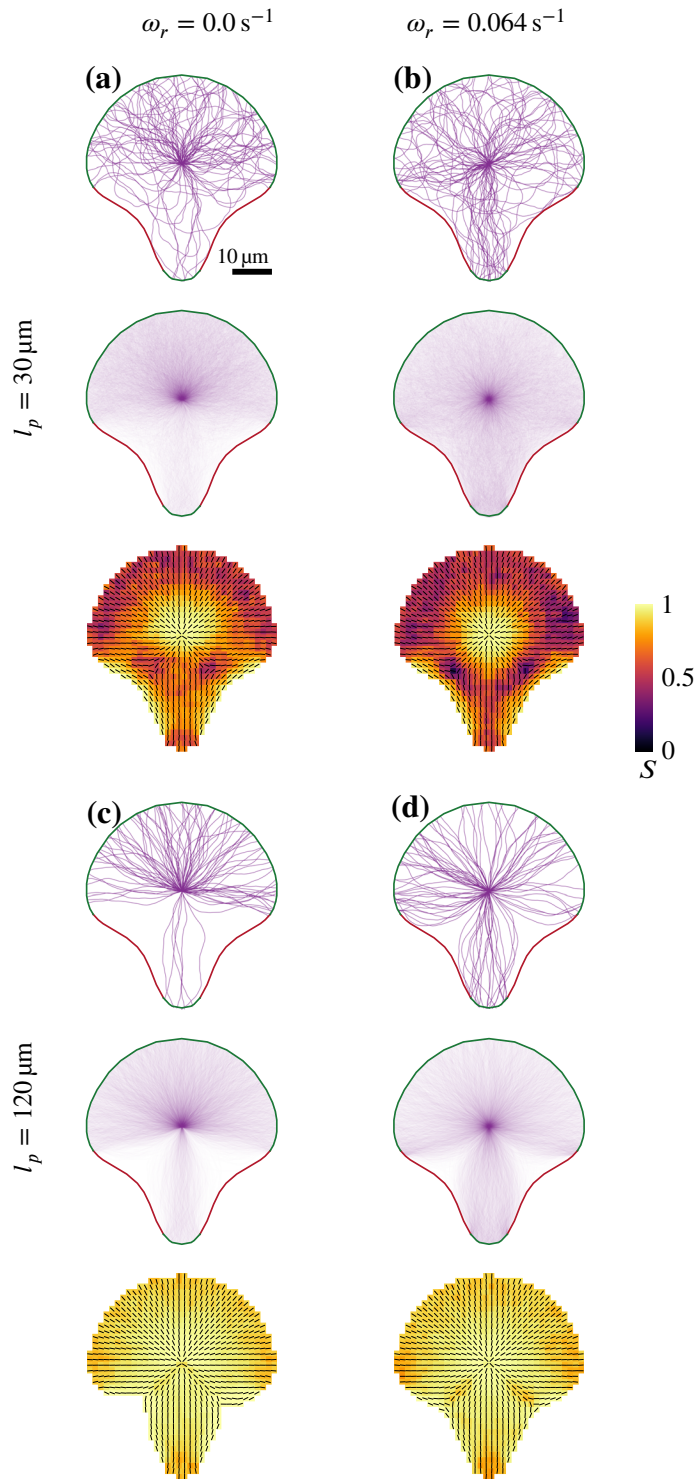


Figure 8.2.: Comparison between complete and partial depolymerization of MTs contacting concave arcs (red). The cell outline is that of a cell adhering on a ∇ -shaped MP. **(a)** Rescue rate $\omega_r = 0.0 \text{ s}^{-1}$ leads to complete depolymerization upon contact with the concave boundaries. Simulation snapshot of 100 MTs (top), averaged MT localization for 100 simulations with 100 MTs each (center) and averaged local orientation field with order parameter s in color code (bottom) are shown. **(b)** Same as (a), but with a nonzero rescue rate, leading to higher filament density close to the concave boundaries, but also to lower order parameters. **(c)** and **(d)** Same catastrophe rate as in (a) and (b), but higher persistence length of $l_p = 120 \mu\text{m}$ leads to straighter filaments and an increase of the depleted regions near the concave boundaries.

We compare a zero rescue rate, leading to complete depolymerization and a lower filament density around the concave parts of the boundary (Fig. 8.2a, top), to a rescue rate that is of the same order as found in experiments. With $\omega_r > 0$, filaments can approach the concave parts of the surface much closer, because upon contact they only lose approximately $4\text{ }\mu\text{m}$ of filament length (Fig. 8.2 b, top). This becomes even more clear if one compares the density maps of 100 simulations with 100 MTs per simulation (Fig. 8.2a and b, center).

In the lower part of each panel of Fig. 8.2 the average orientation field and the corresponding order parameter field, calculated as described in Section 5.2, are shown. For $l_p = 30\text{ }\mu\text{m}$ the two orientation fields are almost identical, but in the order parameter field two “defects” (cf. Chapter 9) with $S \approx 0$ form close to the concave arcs. Due to the non-zero rescue rate, filaments can grow closer to the concave boundary and follow more irregular trajectories. For complete depolymerization, only those filaments are selected that grow more or less directly from the MTOC towards the convex boundaries.

With a higher effective filament persistence length of $l_p = 120\text{ }\mu\text{m}$ the area of filament depletion becomes larger, but interestingly we find “effective bending” at the concave boundaries for a nonzero catastrophe rate (Fig. 8.2 d, top).

The occurrence of catastrophes at the concave boundaries can be motivated by force-induced catastrophes if MT polymerize against rigid walls [240]. However, along concave boundaries we expect MTs to be deflected and so such force-dependent catastrophes should be rare. The process of catastrophes and subsequent rescue events can be seen as an indirect mechanical interaction, that cannot be simulated with the simple PRW algorithm outlined above. Due to these events growth trajectories show similarities with beams being bent at the concave boundaries. In more detailed models, filament mechanics can be considered directly and such a model will be discussed in Section 8.2.

8.1.3. Orientation fields on various micropatterns

Our implementation of the PRW model enables us to simulate the MT network in cells with arbitrary shape. In Fig. 8.3 we present simulation results for four different MPs: ∇ -shaped, H-shaped, Y-shaped and \uparrow -shaped. For the first three patterns the outline was determined by analyzing experimental cell shapes (cf. Section 7.2), while for the arrow-shaped MP the outline was obtained by drawing circular arcs to the non-adhesive boundaries. For all MPs the MTOC was placed at the cell centroid which is in agreement with experimental findings [35]. Again, we simulated 100 MTs per cell and averaged over 100 different simulations. The parameters were chosen as ($l_p = 30 \mu\text{m}$, $\omega_r = 0.064 \text{ s}^{-1}$).

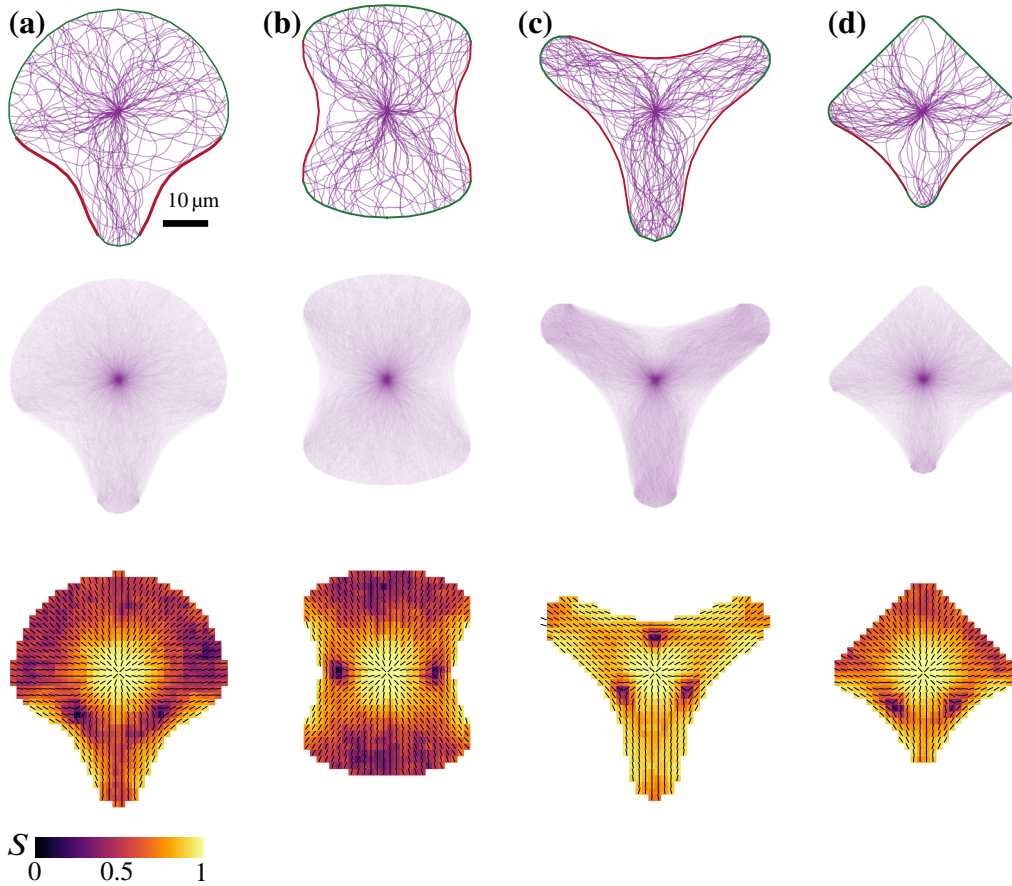


Figure 8.3.: Organization of the MT network in cells with different shape, predicted by the PRW model. **(a)** For a cell on a ∇ -shaped MP, **(b)** on a H-shaped MP, **(c)** on a Y-shaped MP and **(d)** on a \uparrow -shaped MP. Plots show one realization of the MT network layout (upper row), the average MT density calculated from 100 simulations (central row), and the averaged orientation field as well as the order parameter field (lower row).

The density of filaments (Fig. 8.3, center row) shows the characteristic depletion of

filaments in the region between the MTOC and the center of the concave arcs that was also noticed earlier. Also the formation of "defects" in the order parameter field can be observed for all MPs near the circular arcs.

8.1.4. Comparison to experimental results

To find a parameter set that has the highest overlap with the experimental results, we varied the model parameters according to

PRW model	Parameters	Description
	$l_p \in [30 \mu\text{m}, 3000 \mu\text{m}]$	Persistence length
	$\omega_r \in \{0.0 \text{ s}^{-1}, 0.064 \text{ s}^{-1}\}$	MT rescue rate after catastrophe at concave boundaries

The maximum overlap between the simulated and experimental orientation fields was found for $l_p = 30 \mu\text{m}$ and $\omega_r = 0.064 \text{ s}^{-1}$ (cf. Table 8.1 for the corresponding order parameters). Interestingly, this is the same MT persistence length that was measured as the effective persistence length for MTs *in vivo* [91]. For the rescue rate ω_r only two values were chosen to either simulate complete depolymerization of MTs undergoing catastrophic shrinking or rescue with a rate comparable to *in vivo* measurements. Here, the more realistic scenario of MT rescue indeed yields larger agreement with the experimental results, but only by a small margin ($\bar{s} = 0.40$ for $\omega_r = 0.0 \text{ s}^{-1}$). The trend of higher overlap for $\omega_r > 0$ is maintained for higher l_p although \bar{s} decreases (not shown).

MP \ Model	PRW		
	\bar{s}	s_{\parallel}	s_{\perp}
\Uparrow	0.41	0.79	-0.68
H	0.46	0.79	-0.71
Y	0.72	0.86	-0.55

Table 8.1.: Average order parameters s , s_{\parallel} and s_{\perp} for the comparison of orientation fields obtained by experimental analysis and from the PRW model.

As shown in Fig. 8.2, $\omega_r > 0$ also decreases the depletion of MTs near the concave boundaries for higher values of l_p , which we think is a closer resemblance of the MT organization in the real cell.

For the same parameter set, ($l_p = 30 \mu\text{m}$ and $\omega_r = 0.064 \text{ s}^{-1}$), the simulated orientation fields for the H-shaped and Y-shaped MPs yield similar or higher overlap with the experimental results, with excellent agreement for the Y-shaped MP (cf. Table 8.1). The

resulting network configuration of a single run and the corresponding densities are the same as have already been shown in Fig. 8.3a-c.

8.2. Brownian dynamics: Cytosim

Simulating filaments by a PRW is very intuitive and although we included the dynamic instability of MTs, fiber mechanics as a central component for a realistic description is missing. In the PRW model, vertices of the filaments are fixed in space and forces that might act on the tip of the filament do not have any influence on the shape of the rest of the fiber.

A common way of describing a stochastic process under the influence of external forces, e.g. mechanical deformation, is to formulate the problem in terms of a Langevin equation. Originally, it was set up as an alternative approach to Einsteins description of Brownian motion by considering Newton's second law and modeling the specific impulse as a viscous drag plus random fluctuations [241]

$$dv = v(t + dt) - v(t) = -\gamma v(t) dt + \sqrt{\beta^2 dt} \mathcal{N}_t^{t+dt}(0, 1) . \quad (8.8)$$

Here $v(t)$ is the velocity at time t , γ is the Stokes drag coefficient, $\beta^2 dt$ can be interpreted as the variance of the random fluctuations and $\mathcal{N}_t^{t+dt}(0, 1)$ is a normally distributed random variable in the interval t to $t + dt$.

Biological system reside almost exclusively in the regime of low Reynolds numbers [242] and therefore inertia can be neglected, which leads to the Smoluchowski limit, where Langevin's description of Brownian motion corresponds to Einstein's [241]. In this limit we can set $dv = 0$ and if we also include other external forces to Eq. (8.8) we can write down an equation of motion as [216]

$$d\mathbf{x} = \mu F(\mathbf{x}, t) dt + dB(t) . \quad (8.9)$$

Now \mathbf{x} contains the coordinates of multiple objects, μ is a matrix of mobility coefficients, all interaction forces are incorporated into F and $dB(t)$ determines random fluctuations leading to Brownian motion. The case of overdamped Langevin dynamics is often called Brownian dynamics.

Software packages with which system can be simulated based on the Langevin equation include the very flexible ESPResSo framework [243] or Smoldyn [244] and ReaDDy [245] for particle based simulations.

In the context of simulations of the CSK, fiber mechanics plays an important role and a software package that implements this in combination with Brownian dynamics is Cytosim [216]. With this software various components like particles, organelles, filaments and molecular motors can easily be combined into a detailed simulation of the CSK. Cytosim has been used for example for the investigation of spindle positioning in *C. elegans* [246] and in *Xenopus* [247] and simulations of AF interactions in spatially constrained systems [218].

The development of Cytosim has been ongoing for more than ten years, it is thoroughly tested and simulations can be easily set up via a configuration file. This is why we decided to use this readily available software package to implement a more detailed simulation of the intracellular MT network.

As before filaments are considered to be non-interacting and could also be simulated individually. Steric effects can be included in the simulation as has been shown in [218] and could also be used to study actin-MT interaction in the cell interior, but due to the very high computational costs they are omitted here.

MT growth starts at the MTOC with the plus-ends growing towards the cell boundary. The MTOC is modeled as a bead with a non-zero radius that could be moving in general. Such a setup can be used to investigate centrosome centering by systematically varying the relevant parameters [231]. Here we chose to constrain the MTOC to a fixed position at the cell centroid, where it has the highest probability to be located, because a motile centrosome would add more degrees of freedom and we are mainly interested in the averaged coordination of the MT network due to boundary interactions. In a recent study, in which Cytosim was used, it has been shown that cytoplasmic dynein leads to a centering of the MTOC in various cellular geometries [231]. A similar distribution of dynein motors in our model also leads to centrosome centering in the MP geometries under study (results not shown).

8.2.1. Boundary interactions

To treat the stop of MT growth upon contact with the convex, adhesive boundaries we implemented a Capper class in Cytosim. It introduces an intermediate state of halted growth to the Fiber class, which originally could only switch between a growing and a shrinking state. The biological mechanism of capping is thought to be the same as discussed earlier, but now the flexibility of Cytosim allows to additionally investigate unbinding at the convex boundaries. Upon unbinding from the cell cortex, MTs switch to a shrinking state as it is to be expected if the corresponding plus-end stabilizing proteins

dissociate. We introduce a binding rate ω_a^+ to the concave, adhesive parts of the cell boundary and a corresponding unbinding rate ω_a^- and will vary both rates systematically to investigate their influence on the coordination of the MT network.

In Cytosim, a specific growing force can be associated to the nucleation of filaments and so mechanical deformations become possible if growing fibers make contact with the cell boundary. The default interaction scheme in Cytosim is non-frictional gliding along the boundaries, but also active, motor-mediated sliding could be implemented. At the concave parts of the cell outline we use the default gliding interaction scheme without any active components to keep the model parameters to a reasonable level. A table with all parameters used for the Cytosim simulations are given in Appendix A.4.

8.2.2. Binding and unbinding at the cell cortex

Before we discuss the MT orientation fields in different cell geometries we will investigate how binding and unbinding rates at the cell cortex influence the organization of the MT network. We configured the Cytosim simulations in such a way that capping proteins are placed along the convex boundaries of the cell outline and varied the binding and unbinding rates ω_a^+ and ω_a^- . An unbinding event is considered if the effect of the stabilizing proteins at the cell cortex is lost and the MT switches to the shrinking state [200].

For very low binding rates, the behavior at the convex and concave boundaries is approximately equal: Filaments are being bent upon contact with the cell borders, are being deflected at the concave parts and are being aligned tangentially to convex parts of the boundary. A lower persistence length facilitates close alignment with the boundaries, but also stiffer filaments can accumulate at the convex parts if the binding rate is low (Fig. 8.4b).

With an increased binding rate, it is more likely that filaments are stabilized upon first contact with the convex boundary and thereby align approximately normal to it. As a consequence, the local filament density in this region decreases, compared to a situation of many tangential growing filaments (Fig. 8.4c). A decrease in filament density also occurs at the concave boundaries if the fibers become stiffer and the bending extends over the length of the whole filament and it pivots around the MTOC, away from the concave edges (Fig. 8.4d).

To quantify these observations, an order parameter for the fiber density ρ can be defined by comparing the average density in the cell interior ρ_i near the MTOC to the average

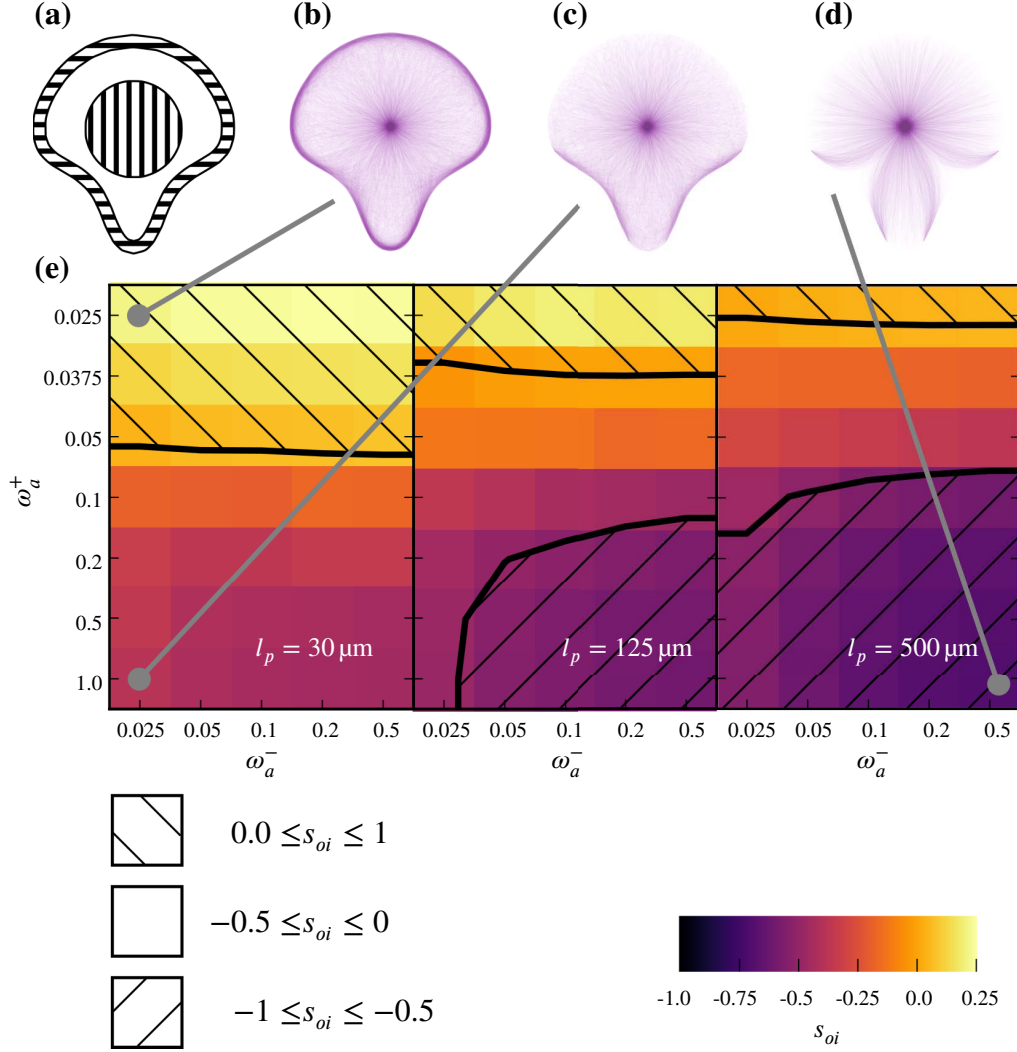


Figure 8.4.: Definition of the the order parameter s_{oi} and excerpt of the phase diagram for variations of the binding rate ω_a^+ , the unbinding rate ω_a^- and the MTs persistence length l_p for simulations of the MT network in a ∇ -shaped cell. **(a)** Outer region (horizontal stripes) and inner region (vertical stripes) for measuring MT density. Both regions have the same area. **(b)** Characteristic density profile for the region $s_{oi} > 0$ in parameter space where $\rho_o > \rho_i$. **(c)** $-0.5 \leq s_{oi} \leq 0$. **(d)** $-0.5 > s_{oi}$. **(e)** For three different values of $l_p \in \{30 \mu\text{m}, 125 \mu\text{m}, 500 \mu\text{m}\}$ cuts through the phase space are shown. ω_a^+ is varied along the vertical axis and ω_a^- along the horizontal axis. Regions of increased MT density at the outer rim ($0.0 \leq s_{oi} \leq 1$), balanced density ($-0.5 \leq s_{oi} \leq 0$) and low density ($-1 \leq s_{oi} \leq -0.5$) are marked in the phase space cuts (cf. also Fig. 8.5 for individual realizations of the MT network). For high binding rates and large persistence lengths the MT density at the cell boundaries decreases. The influence of the unbinding rate can most clearly be seen for intermediate values of l_p and for the transition from a balanced to a centered MT distribution.

density in a band around the outer part of the cell, ρ_o

$$s_{oi} = \frac{\rho_o - \rho_i}{\rho_o + \rho_i}. \quad (8.10)$$

The width of the outer band was chosen as $\delta_o = 3 \mu\text{m}$ and the radius of a circle around the cell centroid was chosen such that it has the same area as the outer rim (Fig. 8.4a). The order parameter $s_{oi} \in [-1, 1]$, but the two interval limits are hardly ever reached.

$s_{oi} = 1$ would mean that the fiber density is entirely concentrated at the cell periphery, which would only be possible for extremely long fibers that grow completely tangential to the boundary. Additionally, ρ_i has to be very small, compared to ρ_o , which is difficult to achieve as the fibers are always anchored at the MTOC.

$s_{oi} = -1$ can be approached more easily for stiff filaments in combination with high binding rates and very high unbinding rates. Then, MT depolymerization is very often induced upon first contact with the convex boundaries and MTs shrink towards the center. From the experimental images we extracted an order parameter of $s_{oi}(\text{CB exp.}) = -0.40$ for the ∇ -shaped MP. A similar s_{oi} can be obtained for ($l_p = 60 \mu\text{m}$, $\omega_a^+ = 0.2 \text{ s}^{-1}$, $\omega_a^- = 0.025 \text{ s}^{-1}$).

By inspecting the MT density profiles we could clearly separate the phase space into three regions:

$s_{oi} > 0$: High MT density at the boundaries. $\rho_o > \rho_i$ (Fig. 8.4b).

$-0.5 \leq s_{oi} \leq 0$: Higher density at cell centroid, but in general a more balanced configuration also found in experimental results. $\frac{1}{3}\rho_i \leq \rho_o \leq \rho_i$ (Fig. 8.4c).

$-0.5 > s_{oi}$: Strongly centered density profile with depletion at the convex boundaries and for high l_p also at the concave boundaries. $\frac{1}{3}\rho_i > \rho_o$ (Fig. 8.4d).

Fig. 8.4e shows 2D cuts through the 3D parameter space spanned by the binding rate to the capping proteins at the convex boundaries ω_a^+ , the corresponding unbinding rate ω_a^- and the MT persistence length l_p . The persistence length was varied between $30 \mu\text{m}$ and $3000 \mu\text{m}$, which corresponds to values of the reduced effective persistence length observed *in vivo* [91] and the persistence length of MTs *in vitro* [63] under the influence of purely thermal fluctuations. In Fig. 8.4e values for the $l_p \in \{30 \mu\text{m}, 125 \mu\text{m}, 500 \mu\text{m}\}$ are shown. For higher values of l_p the phase diagram is qualitatively similar to $l_p = 500 \mu\text{m}$, except that the phase with $s_{oi} > 0$ vanishes. Regions of different behavior, as discussed above, are marked by diagonal patterns.

The persistence length has the largest influence on separation of the parameter space and a clear shift towards more centered MT density patterns ($s_{oi} \leq -0.5$) can be observed for large l_p . For all values of l_p low values of the binding rate ω_a^+ tend to shift s_{oi} to higher values, which means that a significant part of the MTs are localized at the cell boundaries. The influence of the unbinding rate ω_a^- is less pronounced and influences the phase-regions only for intermediate values of l_p and only in the transition from balanced to more centered density distributions.

8.2.3. Orientation fields on various micropattern geometries

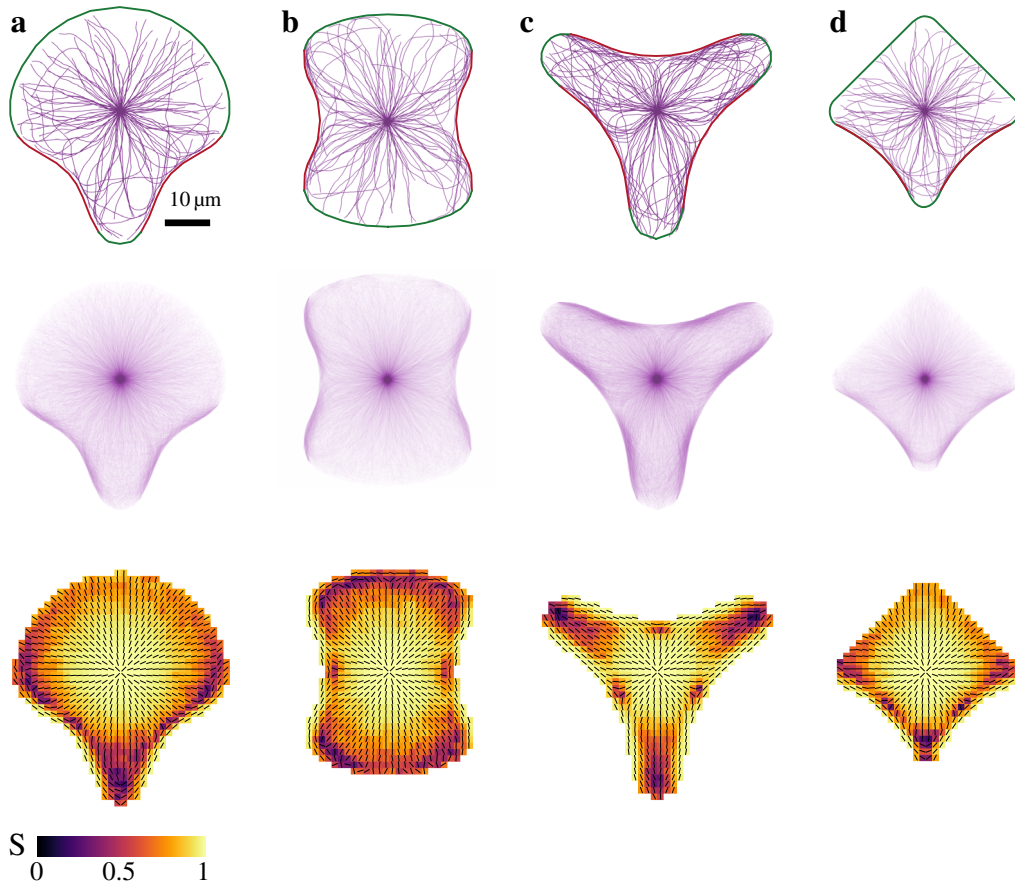


Figure 8.5.: Organization of the MT network in cells with different shape, predicted by Cytosim. Figure layout is the same as in Fig. 8.3 with the top row showing single realizations of the MT network, the center row showing the averaged density and in the bottom row the orientation field and the order parameter are displayed.

Fig. 8.5 shows the same comparison as Fig. 8.3 for four differently shaped cells with a single realization of the MT network displayed in the top row. The MT density is shown

in the center row and the order parameter in combination with the orientation field at the bottom. Compared to the PRW simulations, the order parameter is generally higher in the cell center, which means that there is less variation in filament orientation throughout the different realizations of the MT network.

As in Section 8.1.3, we will discuss the organization of the simulated MT network in cells with different shapes. Taking the ∇ -shaped MP as a reference and considering our discussion of the phase space, we chose ($\omega_a^+ = 0.5 \text{ s}^{-1}$, $\omega_a^- = 0.1 \text{ s}^{-1}$ and $l_p = 30 \mu\text{m}$) for the comparison between the different cell geometries. In Section 8.3 a more detailed comparison between the two filament-based models will be given.

8.2.4. Comparison to the experiments

The comparison to the experimental results will be conducted on the basis of the following range of parameters.

Cytosim	Parameters	Description
	$l_p \in [30 \mu\text{m}, 3000 \mu\text{m}]$	Persistence length
	$\omega_a^+ \in [0.025 \text{ s}^{-1}, 1.0 \text{ s}^{-1}]$	Binding rate to capping protein at convex boundaries
	$\omega_a^- \in [0.025 \text{ s}^{-1}, 0.5 \text{ s}^{-1}]$	Unbinding rate from capping protein; MT goes into shrinking state upon unbinding

With the Cytosim simulation we find high agreement for a cell on a ∇ -shaped MP with the parameter set ($l_p = 125 \mu\text{m}$, $\omega_a^+ = 0.025 \text{ s}^{-1}$, $\omega_a^- = 0.2 \text{ s}^{-1}$) (Table 8.2 and Fig. 8.6a). This parameter set is in the phase of high MT density at the cell periphery (cf. Fig. 8.4). In this phase a substantial number of MTs show tangential alignment at the convex boundaries due to deflection during growth, which is caused by a low binding rate ω_a^+ (Fig. 8.6b).

Model MP	PRW			Cytosim		
	\bar{s}	s_{\parallel}	s_{\perp}	\bar{s}	s_{\parallel}	s_{\perp}
∇	0.41	0.79	-0.68	0.51	0.76	-0.58
H	0.46	0.79	-0.71	0.58	0.80	-0.56
Y	0.72	0.86	-0.55	0.67	0.79	-0.57

Table 8.2.: Average order parameters \bar{s} , s_{\parallel} and s_{\perp} for the comparison of orientation fields obtained by experimental analysis and from the PRW model and Cytosim.

In the experimental orientation fields we also find local tangential alignment close to the convex boundaries which explains the high overlap with the parameter set mentioned

above. Notice that the fitted parameter set is not in the same phase, because the experimentally measured order parameter with $s_{oi}(\text{CB}, \text{exp}) = -0.4$ lies in the region of a balanced MT intensity configuration (Fig. 8.6c,d). This however, is not surprising, because the comparison between Cytosim and the experiments relies solely on the orientation fields and does not consider the intensity distribution. In Cytosim a configuration with some tangential alignment close to the convex boundaries can only be achieved by a higher MT density in this region.

Surprisingly, the persistence length is higher than for the PRW model, but in Cytosim the regions of low fiber density do not decrease as rapidly as in the PRW model and even more rigid MTs can still grow close to the boundaries. In the PRW model bending of filaments at the concave boundaries influences the orientation field only in the immediate vicinity of the outline for low values of l_p (cf. Fig. 8.5a, lower row). In Cytosim this region extends further inwards for higher persistence lengths, which explains the good agreement with the experiments for $l_p = 125 \mu\text{m}$.

For the H-shaped MP the parameter set showing the maximum overlap with the experimental results is identical to the parameter set for the ∇ -shaped MP, but the measured agreement is slightly higher.

For the Y-shaped MP, we found best agreement between experiments and the simulations for $(l_p = 1000 \mu\text{m}, \omega_a^+ = 0.05 \text{ s}^{-1}, \omega_a^- = 0.5 \text{ s}^{-1})$. This result is rather surprising, because for such a high persistence length, there should be almost no MTs near the concave boundaries (Fig. 8.6b, right). In single realizations of the simulated MT network this is almost always the case, but sometimes MTs are bent at the outer edges of the cell and cross the region of low filament density. Due to the averaging procedure there is still a non-zero MT density near the concave boundaries of the Y-shaped MP and therefore also an orientation can be defined here (Fig. 8.6c, right).

Especially for the Y-shaped MP, the experimentally measured MT density differs from the simulated one, due to the high persistence length in the simulations that leads to filament-depleted regions near the concave boundaries (Fig. 8.6c,d; right). In the experiments, the higher MT density at those edges is most likely caused by the influence of the cell nucleus, which causes the MTOC to be located in the vicinity of the stress fibers and compresses MTs between its envelope and the fibers.

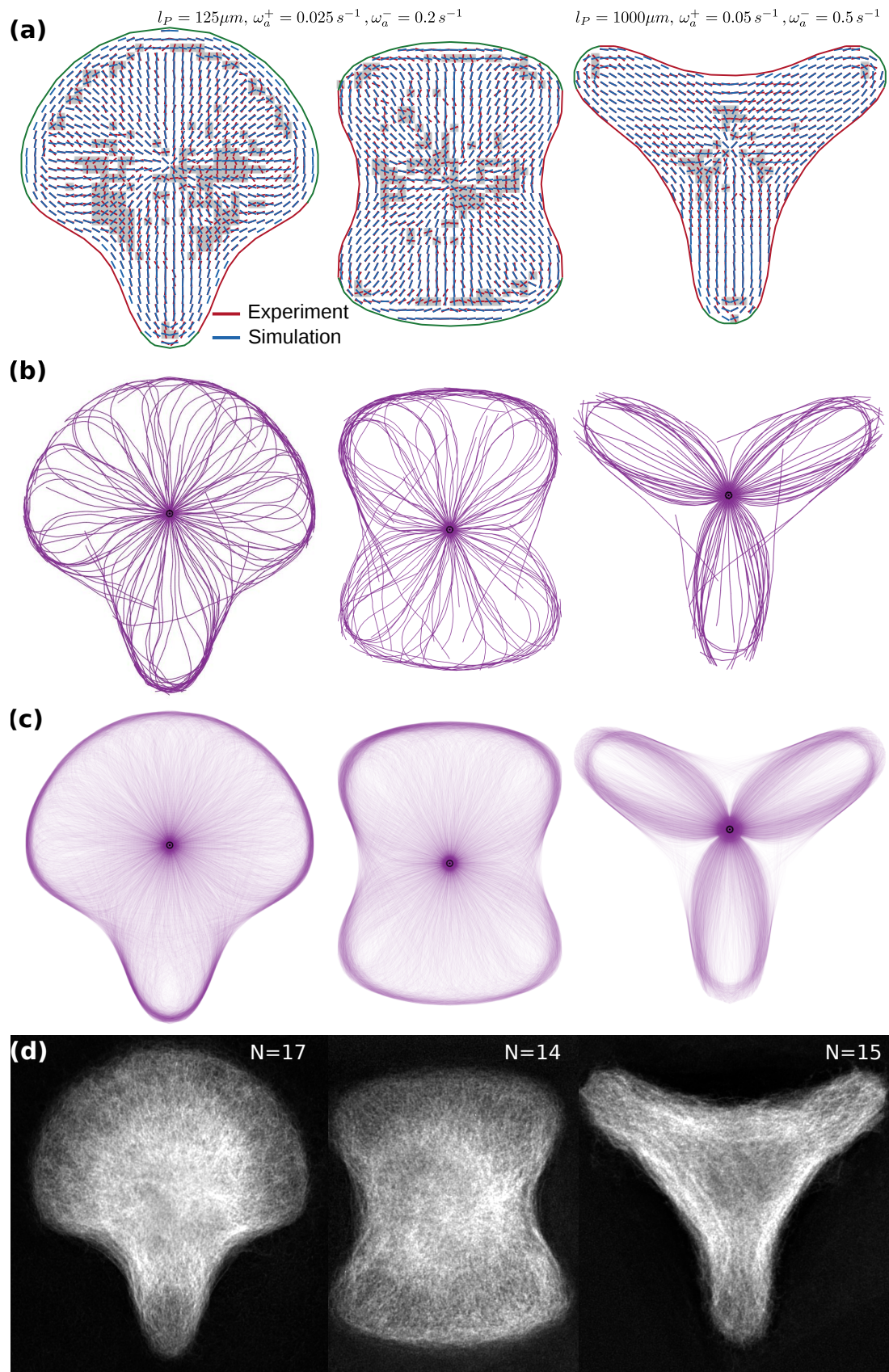


Figure 8.6 (previous page): Comparison between experimental results and Cytosim simulations. **(a)** Experimental orientation fields (red bars) are compared to simulated fields (blue bars). Regions, where alignment deviates by more than $\pi/4$ are marked in dark gray. Concave boundaries (red) and convex boundaries (green) define the simulation domain. Parameter sets for ∇ -shaped MP and H-shaped MP are identical and have been obtained by evaluating the order parameter \bar{s} (Eq. (7.3)). **(b)** Single MT network configuration for 100 MTs. Due to low binding rates ω_a^+ less rigid MTs can bend and grow tangential to the convex boundaries. **(c)** Averaged simulated MT density. Depletion due to high l_p near the concave boundaries can be observed for the Y-shaped MP. **(d)** Experimental MT densities averaged over all imaged cells. Overlap with simulated densities (c) is less pronounced, but for the parameter estimation of the model only the orientation fields were used.

8.3. Comparison of the models

The biggest difference between the two filament-based models lies in the resulting filament density. In the PRW model interactions with the boundaries and “bending” of the filaments is controlled by catastrophes that are induced at the concave parts of the cell. Catastrophes reduce the density at those boundaries and can even lead to completely depleted regions in the simulation domain.

In Cytosim, there is direct mechanical interaction between the filaments and the cell outline, which leads to long range deformation of the filaments for large persistence lengths and local bending with high radii of curvature for lower l_p . This type of interaction causes an increased MT density at the concave boundaries. For dynamic binding and unbinding at the convex parts of the cell, a high MT density can be observed there as well. In the phase diagram in Fig. 8.4e, this corresponds to a transition from a balanced MT density distribution ($-0.5 \leq s_{oi} \leq 0$) to one with high density at the boundaries ($-1 \leq s_{oi} \leq -0.5$). Calculating s_{oi} for the PRW model leads to values of approximately $-0.54 \leq s_{oi} \leq -0.15$, so the phase of high MT density at the boundaries is almost never reached. It is clear that the current PRW cannot yield high MT densities at the convex boundaries, because there, the filament growth is stopped immediately.

To measure agreement between the filament-based models we defined a weighted distance $d(P_{\text{PRW}}, P_{\text{CS}})$, given the parameter sets $P_{\text{PRW}}, P_{\text{CS}}$ of the PRW model and Cytosim.

For all combinations of the parameter sets $P_{\text{PRW}}, P_{\text{CS}}$ of the two models, we computed the set of mutual order parameters D .

We quantify the agreement of the orientation fields by

$$A = Z(\{1 - \bar{s}(P_{\text{PRW}}, P_{\text{CS}})\}), \quad (8.11)$$

and the absolute, spatially averaged, difference between the filament densities fields of the two models $\rho(P_{\text{PRW}})$ and $\rho(P_{\text{CS}})$ as

$$B = Z \left(\left\{ \left\langle |\rho(P_{\text{PRW}}) - \rho(P_{\text{CS}})| \right\rangle \right\} \right). \quad (8.12)$$

The average $\langle \dots \rangle$ is taken over the simulation domain. The two measures span very different ranges and to make them comparable, we calculated the Z-score of each set by subtracting the mean and dividing by the standard deviation. We used $1 - \bar{s}(P_{\text{PRW}}, P_{\text{CS}})$, because $\bar{s}(P_{\text{PRW}}, P_{\text{CS}}) = 1$ will give the best match between the two models in terms of the orientation fields, while $\langle |\rho(P_{\text{PRW}}) - \rho(P_{\text{CS}})| \rangle = 0$ means that the two simulated densities agree.

The set D of distances between the two simulations then reads

$$D = \{ A(P_{\text{PRW}}, P_{\text{CS}}) + B(P_{\text{PRW}}, P_{\text{CS}}), \forall P_{\text{PRW}}, P_{\text{CS}} \}. \quad (8.13)$$

The best model agreement can now be estimated by finding the minimum value of D and thereby the corresponding parameter sets

$$\underset{P'_{\text{PRW}}, P'_{\text{CS}}}{\text{argmin}}(D) = \begin{cases} P'_{\text{CS}} & = (l_p = 1000 \mu\text{m}, \omega_a^+ = 1.0 \text{ s}^{-1}, \omega_a^- = 0.025 \text{ s}^{-1}) \\ P'_{\text{PRW}} & = (l_p = 120 \mu\text{m}, \omega_r = 0.064 \text{ s}^{-1}). \end{cases}$$

In Cytosim, the high binding rate to the convex boundaries of $\omega_a^+ = 1$ agrees with the PRW model assumption that MT growth is stopped of contact with these boundaries is made. Also $\omega_a^- = 0.025 \text{ s}^{-1}$ is the lowest unbinding rate chosen for the parameter scan in Cytosim and corresponds to the situation in the PRW model, where filaments cannot switch to a shrinking state, once they have been stabilized at the convex boundaries.

Interestingly, the persistence lengths of the two models do not agree, but the mechanism of “effective bending” at the concave boundaries in the PRW model yields similar trajectories than the deflection and bending of growing MTs in Cytosim (Fig. 8.7a,b). This can also be found in the direct comparison of the two orientation fields (Fig. 8.7c).

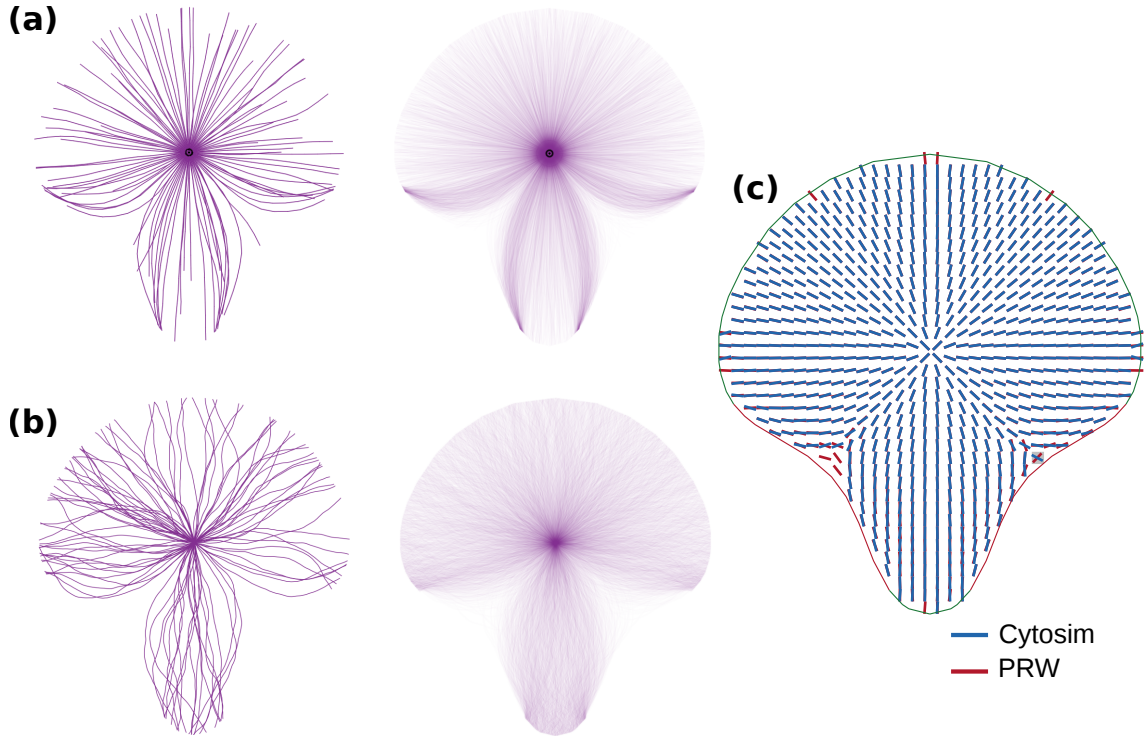


Figure 8.7.: Best match between Cytosim simulations and the PRW model. **(a)** Single realization of the MT network and averaged densities are shown. Parameter set is: ($l_p = 1000\mu\text{m}$, $\omega_a^+ = 1.0\text{s}^{-1}$, $\omega_a^- = 0.025\text{s}^{-1}$). **(b)** PRW model for parameter set: ($l_p = 120\mu\text{m}$, $\omega_r = 0.064\text{s}^{-1}$). **(c)** Orientation fields for Cytosim (blue) and the PRW model (red) show very close agreement.

8.4. Discussion

In this chapter we discussed two modeling approaches to study the organization of the MT network in cells with clearly defined shape.

In the first model we simulated MT growth by a PRW and introduced simple interaction rules at the boundaries of the simulation domain. This model is conceptually simple and easy to implement numerically, but it has the drawback that vertices are fixed in space, once their position has been generated by the algorithm. We could show that a mechanism that induces shrinking of the MTs upon contact with the concave boundaries induces an effective bending of the growth trajectories. Furthermore, we showed that the best agreement between simulated and measured MT orientation fields for parameters with a reduced effective persistence length $l_p = 30\mu\text{m}$ and a rescue rate from the shrinking state of $\omega_r = 0.064\text{s}^{-1}$, which are consistent with earlier experimental estimations [91, 239].

In the second approach we carried out Brownian dynamics simulations of growing MTs with the software Cytosim. With it, we were able to implement more detailed in-

teractions with the boundaries of the simulated cell by introducing rates for stabilization and shrinking of MTs upon contact with the convex parts of the boundary.

These interactions led to three characteristically different configurations of the MT network: High density at the outer boundary of the simulation domain, balanced density between peripheral and centered regions and pronounced density at the cell centroid. We conducted a scan of the parameter space and found that a persistence length on the order of $l_p \approx 60 \mu\text{m}$ with an intermediate binding rate of $\omega_a^+ \approx 0.2 \text{ s}^{-1}$ and very low unbinding rates yielded a similar order parameter in the simulations compared the experimental one. These parameters are robust to some variation and multiple combinations can achieve similar outcomes. For larger l_p , the range of suitable model parameters to achieve similar order parameters as in the experiments becomes smaller, which supports the experimental observations of a lower effective persistence length.

In terms of the orientation field, we could achieve a close match between experiments and simulations by choosing a very low binding rate of the MT tips to the convex parts of the boundary. This leads to deflection and tangential alignment of the simulated fibers that we also observed in our experimental analysis. Although the origin of the tangential alignment in the experimental orientation fields cannot be linked to a single effect, our simulations indicate that MT growth might not be stopped immediately upon contact with the cell cortex, as it was suggested earlier [35]. Rather, there might be some local interactions between MTs and the cell cortex, for example due molecular motors or crosslinking proteins, that cause such an effect. The best matching parameters for the persistence length were found to be on the order of $l_p = 125 \mu\text{m}$, which is more than an order of magnitude lower than one would expect from purely thermal bending.

Our models suggest to further investigate the coordination of MTs and the actin CSK by experimental work. Here, especially MT growth dynamic would be interesting to study. Modifications of motor proteins and crosslinkers by chemical inhibition or by RNAi could provide further insight into the interactions of the MT tips with the cortex of cells adhering to MP substrates. Live cell super-resolution microscopy has recently been shown to be applicable for actin and MTs [248] and could be a way to obtain high precision recordings of MT dynamics.

From a modeling perspective it would be interesting to include more details of cellular architecture into the model. One could include the cell nucleus and investigate how it is positioned depending on the interactions of MTs with the cell boundaries. Cytosim has recently been used to study the positioning of the centrosome [231] and such approaches could be extended by more detailed interactions of the MT network with the cell outline.

Furthermore, it would be interesting to simulate MT based transport on such networks. Predictions of the models could be compared to the effects of RNAi mediated knockdown, which we analyzed earlier.

Liquid crystal model

In the last chapter we simulated ensembles of filaments and calculated orientation fields by averaging the orientation of the individual filaments. In our experimental analysis we did not have access to individual filaments and extracted the orientation of the MT network from the structure tensor, which relies on image gradients. The comparison of the experimental outcomes and the simulation results relies on the MT orientation field, so an alternative approach is to formulate a continuum theory for the orientation field and use it to predict the organization of the MT network

In a general field theory, the state of a system can be described by an order parameter $\langle\phi\rangle$. In the unordered phase $\langle\phi\rangle = 0$ and it becomes non-zero under a phase transition into an ordered state. One way of constructing a field theory is to define the free energy F of the system under study as $F = E - TS$, i.e. the difference of an internal energy E and the temperature T times the entropy S [249].

The free energy can be a complicated functional of the order parameter $\langle\phi\rangle$. A phenomenological approach of deriving an expression for F is to assume that the order parameter is small near the phase transition and expand F in terms of a power series of $\langle\phi\rangle$ [250]. In addition, spatial variations of the order parameter will contribute to F and also expression for this has to be derived.

The order parameter is always related to a symmetry of the system that is broken by it. In a two-dimensional plane, the simplest continuous transformation is given by the group of orthogonal rotations O_2 and can be broken by a vector order parameter $\langle\mathbf{s}\rangle = s(\cos\vartheta, \sin\vartheta)$ [249]. Similar to the classic Ising model, with two-state spins arranged on a lattice, one can define the xy-model with spins $\mathbf{s}_i = s(\cos\vartheta_i, \sin\vartheta_i)$ on lattice sites i . The Hamiltonian of the xy-model is given by $\mathcal{H} = -J \sum_{\langle i,j \rangle} \cos(\vartheta_i - \vartheta_j)$ and is invariant under spatial uniform changes of ϑ . In general, changes of ϑ will not be spatially uniform

and usually will manifest in an increased free energy \mathcal{F} that can be expressed in terms of $\nabla\theta$ for the xy-model [249].

Based on this concepts, our modeling approach will be, to define a suitable order parameter that breaks the system's symmetry and derive a free energy functional that incorporates effects of the phase transition from the unordered into an ordered state as well as spatial variations of the order parameter.

An example for a physical system, where rotational symmetry is broken are nematic liquid crystals (LCs). Here, a tensor order parameter can be defined in term of a unit vector \mathbf{n} as [230, 249]

$$Q_{ij} = S(n_i n_j - \frac{1}{3}\delta_{ij}), \quad (9.1)$$

where \mathbf{n} describes the principle axis of \mathbf{Q} . S now denotes a scalar order parameter. Before we argue that such an order parameter is a suitable choice for modeling the MT orientation field, we will give a brief introduction into concepts for the description of LCs.

9.1. Introduction into liquid crystals

A LC is a mesomorphic phase that has characteristics of both a liquid and a crystal. A crystal has a clearly defined positional order of the molecules, given by the crystal lattice, while a liquid is isotropic above a length scale ξ , where correlations between molecules are lost.

If we consider a medium with no positional order in any direction it could be classified as a liquid, but if the correlation function of finding two molecules in the same orientational configuration is anisotropic, it is not an isotropic liquid anymore, but a nematic LC. If one-dimensional positional order is found in the medium, the phase is called smectic and for two-dimensional order in a three-dimensional medium is defined as a columnar phase [230] (cf. Fig. 9.1).

The simplest building blocks of LCs are elongated molecules that can be rod-like with rotational symmetry along their long axis (uniaxial LC). Alternatively, they could have no axis of rotational symmetry, which would be the case for elongated rectangles (biaxial LC). Other building blocks can be disk-like molecules or rigid polymers [230].

A typical phenomenon in LCs and solids are topological defects in the material. In LCs defects create so called Schlieren textures (Fig. 9.2a), which can be observed by a polarizing microscope [230]. A defect in a LC, also called disclination, represents a discontinuity of the director field that can either be located at one point in 2D or along a line in 3D. The strength m of a defect (or winding number) is defined by observing the

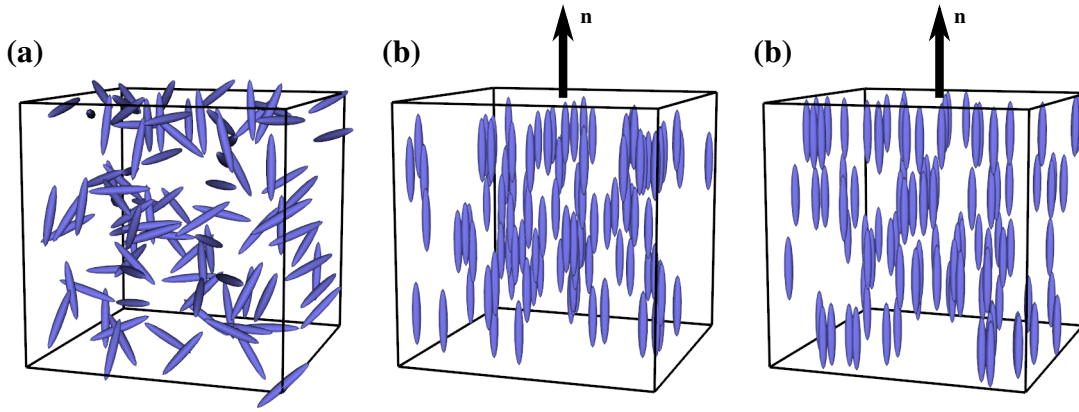


Figure 9.1.: (a) Isotropic configuration of rod-like molecules. (b) Nematic order with macroscopic orientation according to \mathbf{n} , but no positional order. (c) Smectic configuration with orientational order and 1D positional order in the form of layers along the vertical axis.

rotation angle ω of the director on a loop around the defect core. ω is then a multiple of π

$$\omega = 2\pi m, \quad (9.2)$$

where m is integer or half integer [230]. In (Fig. 9.2b-d) defects of strength $m = -1/2$, $m = 1/2$ and $m = 1$ are shown with the corresponding director fields. If two defects can

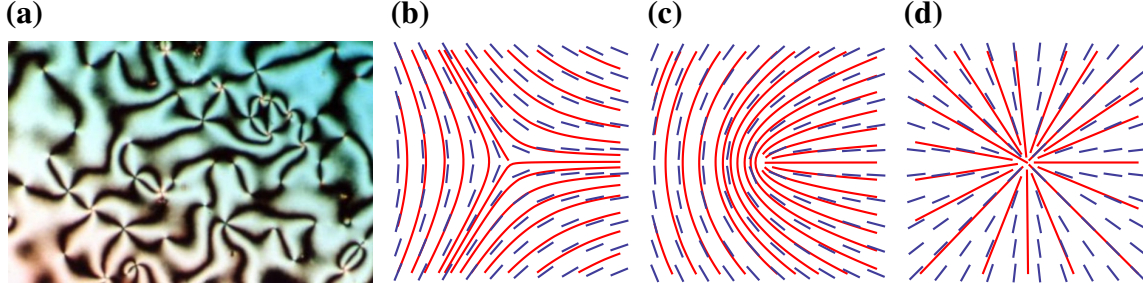


Figure 9.2.: (a) Schlieren texture of a LC observed under a polarizing microscope [251]. (b) Director configuration (blue) and tangential lines (red) of a $m = -1/2$ defect. (c) Of a $m = 1/2$ defect. (d) Of a $m = +1$ defect.

be encircled by one loop their winding numbers add up, i.e. two $m = 1/2$ defects create the same far-field as one $m = 1$ defect [249]. The surface of a sphere has a topological charge of 2, which means that two $m = 1$ or four $m = 1/2$ defects form if it is covered with a nematic medium.

9.2. Applicability of a liquid crystal model to microtubules

In vitro, MT solutions were shown to form a nematic LC like phase [252]. Active gels can be constructed from mixtures of stabilized MTs, polymers that induce attractive interactions due to depletion forces and kinesin motors that induce sliding of MTs [253]. If such active systems are confined on 2D surfaces they show rich dynamics, e.g. by the formation and annihilation of defects in planar geometries [253, 254] or on the surface of a sphere [255], where four $+1/2$ defects form. Such behavior resembles effects found in LC solutions and experimentally underline the active gel theory (Chapter 7).

Brugués and Needleman [228] formulated a model for the mitotic spindle, based on an active LC theory, that yielded excellent agreement between experiment and theory. One of the reasons that this model was successful, and also that MT solutions display liquid-crystal-like behavior, is that the density of MTs in such systems is very high. In fact, it is significantly higher than the density of the MT network during interphase. This high and approximately constant density makes the continuum description applicable and the mitotic spindle can indeed be considered as a liquid-crystal-like object.

Our description of the MT network is a qualitative one, because the MT network has a lower density during interphase and we would need to investigate the system at very large length scales in order to formulate a quantitatively correct continuum description. Also, a static model can only be an approximation to the highly dynamic CSK. Keeping this limitations in mind we argue that a static continuum model based on the theory of LCs is nevertheless suitable to investigate an averaged orientation field of the MT network.

Let us consider a single MT growing inside the cell, influenced by interactions with the actin CSK, intermediate filaments and other intracellular compartments. It grows towards the cell boundary, where it might get deflected or anchored. For a short period of several minutes this MT might be stable and it could influence other MTs growing next to it due to steric effects or mutual interactions due to crosslinkers or motors. Depending on the strength of the interactions a newly growing MT might align with the stable one and follow a similar growth trajectory. At some point the older MT might depolymerize and the newer one could get stabilized or continue growing under the influence of the cell boundaries. Due to the dynamic nature of the CSK it is likely that we can find regions where locally there are nematic interactions of several polymers as described in [256] and one can therefore define a local director field.

Even if one does not assume interactions between MTs that lead to similar effects as

observed in LCs, the nematic order parameter and the corresponding free energy functional can still provide the basis to model the MT orientation field. We will not derive parameters for the LC theory from microscopic MT interactions, but rather use it as a mathematical concept to capture the effects observed experimentally. Nevertheless, effects of liquid-crystal-like behavior can be observed in MT system, but to relate those to the MT network of the cells we studied, further experimental work is necessary.

9.3. Mathematical description of liquid crystals

The first mathematical theories for LCs go back to Oseen, Zocher and Frank [257–259] with the theory of Frank being the most profound [260]. Frank derived the elastic energy of a LC in terms of a director \mathbf{n} and its derivatives and defined four material moduli, k_{11} , k_{22} , k_{33} and k_{24} . Those can be related to three bulk deformation fields, splay, twist, and bend, whose distortion energy is proportional to the corresponding modulus (Fig. 9.3). The fourth moduli, saddle-splay, can be transformed and is usually omitted in a theory for the bulk.



Figure 9.3.: Three bulk deformation modes of a LC: (a) splay, (b) twist, (c) bend. From [261].

De Gennes extended those theories by defining a tensor order parameter [262] and used a Landau expansion of the free energy [263] to investigate transitions from the isotropic to the nematic phase. Furthermore, he studied the influence of electric and magnetic fields and the hydrodynamics of LCs [230].

For the model of the MT orientation field, we will consider only the simple case of a LC in the nematic phase in two dimensions. A general discussion of the three dimensional theory can be found in [264]. In two dimensions we do not have to distinguish between uniaxial and biaxial nematics, because all molecules lie in the plane and we have to consider only orientational order defined by one angle.

To obtain a macroscopic description of a LC we need a to define an order parameter that breaks the orientational symmetry and defines if the state is in a ordered or isotropic phase. As mentioned above, a common choice is to define a symmetric, traceless order

parameter \mathbf{Q} as

$$\mathbf{Q} = S(2\mathbf{n} \otimes \mathbf{n} - \mathbf{I}) . \quad (9.3)$$

The eigenvector $\mathbf{n} = \mathbf{n}(x, y) \in S^1$ defines the macroscopic orientation and \mathbf{Q} is symmetric under the transformation $\mathbf{n} \rightarrow -\mathbf{n}$. s is a scalar order parameter that describes the degree of orientation around \mathbf{n} [265, 266] and \mathbf{I} is the identity matrix.

Our following derivations will follow mainly those of Luo, Majumdar, and Erban [265]. The scalar order parameter is defined as

$$S = \langle 2 \cos^2 \vartheta - 1 \rangle , \quad (9.4)$$

with ϑ the angle between the LC molecules and \mathbf{n} . It ranges from $S = 1$ for perfect alignment between the local molecule axis and \mathbf{n} to $S = -1$ for orthogonal alignment. For an isotropic distribution of molecule orientations $S = 0$. Notice that S is a different quantity as s , which was defined in Eq. (7.3) as an spatial average for the comparison of orientation fields.

Because \mathbf{Q} is symmetric and traceless, in two dimensions it has only two independent components and can therefore be written as

$$\mathbf{Q} = \begin{pmatrix} p & q \\ q & -p \end{pmatrix} . \quad (9.5)$$

If we write the unit vector field \mathbf{n} as

$$\mathbf{n}(x, y) = \begin{pmatrix} \cos \vartheta(x, y) \\ \sin \vartheta(x, y) \end{pmatrix} \quad (9.6)$$

and consider Eq. (9.5), we find that

$$\mathbf{q} = \begin{pmatrix} p \\ q \end{pmatrix} = S \begin{pmatrix} 2 \cos^2(\vartheta) - 1 \\ \cos(\vartheta) \sin(\vartheta) \end{pmatrix} = S \begin{pmatrix} \cos(2\vartheta) \\ \sin(2\vartheta) \end{pmatrix} . \quad (9.7)$$

The eigenvalues of \mathbf{Q} are $\lambda_{1,2} = \pm S$ and by this in combination with the spectral

theorem, we find

$$\text{tr} \mathbf{Q} = \sum_i \lambda_i = 0, \text{ by definition} \quad (9.8)$$

$$\text{tr} \mathbf{Q}^2 = \sum_i \lambda_i^2 = 2S^2 \quad (9.9)$$

$$\text{tr} \mathbf{Q}^3 = \sum_i \lambda_i^3 = 0. \quad (9.10)$$

Now, we will construct the free energy that is needed for the complete description of the LC. In a general phenomenological theory multiple terms contribute to the free energy, which are the elastic energy of distortions to the LC, the thermotropic energy that defines if the LC is in the isotropic or nematic phase, electromagnetic energy terms resulting from external fields and terms introduced by interactions with the surface of the LC [264].

For our model of the orientation field of the MT network we need to define a free energy term \mathcal{F}_{el} , for the distortion of the \mathbf{Q} -tensor due to spatial variations, the thermotropic energy \mathcal{F}_{n} and boundary a energy term \mathcal{F}_{B} , because of the finite size of the system. The total free energy then is

$$\mathcal{F}[\mathbf{Q}] = \mathcal{F}_{\text{n}}[\mathbf{Q}] + \mathcal{F}_{\text{el}}[\mathbf{Q}] + \mathcal{F}_{\text{B}}[\mathbf{Q}]. \quad (9.11)$$

9.3.1. Thermotropic energy

The thermotropic energy \mathcal{F}_{n} defines the state (isotropic or nematic) of the LC and can be derived by following the Landau theory of phase transitions [263]. In the isotropic phase $\mathbf{Q} = 0$, which suggests to express this potential function as a power series expansion around $\mathbf{Q} = 0$. A common way of writing this expansion is [230]

$$f_n = \frac{a}{2} Q_{ij} Q_{ji} + \frac{b}{3} Q_{ij} Q_{jk} Q_{ki} + \frac{c}{4} (Q_{ij} Q_{ji})^2 \quad (9.12)$$

$$= \frac{a}{2} \text{tr}(\mathbf{Q}^2) + \frac{b}{3} \text{tr}(\mathbf{Q}^3) + \frac{c}{4} (\text{tr}(\mathbf{Q}^2))^2, \quad (9.13)$$

where

$$\mathcal{F}_{\text{n}} = \int_{\Omega} f_n \, dA. \quad (9.14)$$

In general, a , b and c can be temperature dependent, but a common approach is to approximate this dependency by setting b and c as constant and writing

$$a(T) = \gamma(T - T^*) = \gamma \Delta T. \quad (9.15)$$

Now, $\gamma > 0$ is a constant and T^* the critical temperature at which the transition from the isotropic to the nematic phase occurs. In our simulations we keep the temperature fixed and investigate the system in the nematic phase at $T < T^*$, which is why we denote the thermotropic energy as

$$\mathcal{F}_n := \int_{\Omega} -\frac{\alpha^2}{2} \text{tr}(\mathbf{Q}^2) + \frac{c^2}{4} (\text{tr}(\mathbf{Q}^2))^2 \, dA. \quad (9.16)$$

$\alpha^2 > 0$ is temperature dependent and we have dropped the $\text{tr}(\mathbf{Q}^3)$ term, because it is zero. Using Eq. (9.9), Eq. (9.16) becomes

$$\mathcal{F}_n := \int_{\Omega} c^2 S^4 - \alpha^2 S^2 \, dA, \quad (9.17)$$

which obtains its minimum at

$$S_0 = \sqrt{\frac{\alpha^2}{2c^2}}. \quad (9.18)$$

We can then write the thermotropic energy as

$$\mathcal{F}_n = \int_{\Omega} \frac{1}{\epsilon^2} (S^2 - S_0^2)^2 - \frac{S_0^4}{\epsilon^2} \, dA, \quad (9.19)$$

with

$$\epsilon^2 := \frac{1}{c^2}. \quad (9.20)$$

The term S_0^4/ϵ^2 can be dropped, because it contributes only a constant to the total free energy \mathcal{F}

9.3.2. Elastic energy

The elastic energy \mathcal{F}_{el} depends on \mathbf{Q} and $\nabla \mathbf{Q}$ and a common approximation is given by [264, 267]

$$f_{\text{el}} = \frac{L_1}{2} \frac{\partial Q_{ij}}{\partial x_k} \frac{\partial Q_{ij}}{\partial x_k} + \frac{L_2}{2} \frac{\partial Q_{ij}}{\partial x_j} \frac{\partial Q_{ik}}{\partial x_k} + \frac{L_3}{2} \frac{\partial Q_{ik}}{\partial x_j} \frac{\partial Q_{ij}}{\partial x_k} + \frac{L_4}{2} Q_{lk} \frac{\partial Q_{ij}}{\partial x_l} \frac{\partial Q_{ij}}{\partial x_k}, \quad (9.21)$$

where the summation convention is assumed.

The elastic constants can be related to Frank's elastic constants by [264]

$$L_1 = \frac{1}{6S^2}(k_{33} - k_{11} + 3k_{22}) \quad (9.22)$$

$$L_2 = \frac{1}{s^2}(k_{11} - k_{22} - k_{24}) \quad (9.23)$$

$$L_3 = \frac{1}{s^2}k_{24} \quad (9.24)$$

$$L_4 = \frac{1}{2s^3}(k_{33} - k_{11}) . \quad (9.25)$$

In 2D, with the Q-tensor defined as in Eq. (9.5), Eq. (9.21) can be simplified to

$$\begin{aligned} f_{\text{el}} = & \tilde{L}_1(p_x^2 + p_y^2 + q_x^2 + q_y^2) \\ & + \tilde{L}_2(p_y q_x - p_x q_y) \\ & + \tilde{L}_3(2p(p_x p_y + q_x q_y) + q(p_x^2 + q_x^2 - p_y^2 - q_y^2)), \\ \text{with } \tilde{L}_1 := & 2L_1 + L_2 + L_3 = \frac{1}{3s^2}(k_{33} + 2k_{11}) \\ \tilde{L}_2 := & L_2 - L_3 = \frac{1}{s^2}(k_{11} - k_{22} - 2k_{24}) \\ \tilde{L}_3 := & 2L_4 = \frac{1}{s^3}(k_{33} - k_{11}). \end{aligned} \quad (9.26)$$

Here, we use the shorthand notation $p_i = \partial p / \partial x_i$. A more simplistic approach, which is commonly applied to obtain more compact equations, is to keep only the first term of the elastic energy density (Eq. (9.21)) and express it in an approximation with a single elastic constant \tilde{L} , i.e. $k_{11} = k_{22} = k_{33}$. The elastic energy then assumes the form

$$\mathcal{F}_{\text{el}} = \frac{L}{2} \int_{\Omega} \frac{\partial Q_{ij}}{\partial x_k} \frac{\partial Q_{ij}}{\partial x_k} dA = L \int_{\Omega} (p_x^2 + p_y^2 + q_x^2 + q_y^2) dA . \quad (9.27)$$

Notice that we will now drop the tildes again for the elastic constants.

9.3.3. Surface energy and boundary conditions

After having derived the two terms of the Landau–de Gennes free energy in the bulk, we will now turn our attention towards contributions of the surface. The influence of boundary effects might be stronger or weaker, depending on the ratio of bulk volume to surface area. In our model, boundary contributions significantly influence the final orientation field.

Surface effects enter the theory in two ways. Either a fixed orientation at the boundary

is introduced, a so called strong anchoring condition. Alternatively, one defines a surface energy term that depends on the easy direction at the boundary, which is then called weak anchoring.

On the microscopic scale one can think of the easy direction as a preferred alignment of the LC molecules at the surface that can be due to a specific microstructure of the interface. Some examples to create such a microstructure include rubbing the surface or coating it with thin films [230].

In the theoretical description of strong anchoring the eigenvector \mathbf{n} in Eq. (9.3) is constrained to a fixed value, e.g. the surface normal \mathbf{v} or surface tangent $\boldsymbol{\tau}$. The strong anchoring case is incorporated into the theory by a Dirichlet boundary condition $\mathbf{Q} = \mathbf{Q}_B$.

For weak anchoring, a surface energy term is introduced for which the Rapini-Papoular surface energy [268] is a common choice. In a tensorial theory it can be expressed as [269]

$$F_S = \frac{W}{2} \int_{\partial\Omega} \text{tr}((\mathbf{Q} - \mathbf{Q}_B)^2) da, \quad (9.28)$$

where the Q-tensor at the surface is given by \mathbf{Q}_B . This term penalizes any deviations from the easy direction. For $W \rightarrow \infty$ it converges to the strong anchoring case [265].

9.3.4. Scaling of the Landau–de Gennes free energy

If we combine Eqs. (9.19), (9.27) and (9.28), we can write down the Landau–de Gennes free energy in terms of the components of \mathbf{Q} as

$$\mathcal{F}[p, q] = \int_{\Omega} L(|\nabla p|^2 + |\nabla q|^2) + \frac{1}{\epsilon^2}(p^2 + q^2 - S_0^2)^2 dA + W \int_{\partial\Omega} |(p, q) - \mathbf{g}|^2 da \quad (9.29)$$

or by utilizing the short notation according to Eq. (9.7) as

$$\mathcal{F}[\mathbf{q}] = \int_{\Omega} L(\nabla \mathbf{q})^2 + \frac{1}{\epsilon^2}(|\mathbf{q}|^2 - S_0)^2 dA + W \int_{\Gamma_2} |\mathbf{q} - \mathbf{g}|^2 da. \quad (9.30)$$

We now divide Eq. (9.30) by the elastic constant L and define

$$\begin{aligned} \tilde{\mathcal{F}} &:= \mathcal{F}/L \\ \tilde{\epsilon} &:= \epsilon \sqrt{L} \\ \tilde{W} &:= W/L \end{aligned} \quad (9.31)$$

which leads to a rescaled free energy

$$\tilde{\mathcal{F}}[\mathbf{q}] = \int_{\Omega} (\nabla \mathbf{q})^2 + \frac{1}{\tilde{\varepsilon}^2} (|\mathbf{q}|^2 - S_0)^2 dA + \tilde{W} \int_{\Gamma_2} |\mathbf{q} - \mathbf{g}|^2 da. \quad (9.32)$$

Now, the tildes will be dropped and we will use only the rescaled.

9.4. Biologically motivated choice of boundary conditions

From Fig. 7.1 we expect the MT network to be oriented normally in the vicinity of the convex parts of the cell outline and to be oriented tangentially near the concave circular arcs. We include these observations into the theory by assuming strong anchoring according to the surface normal \mathbf{v} on the convex parts Γ_1 of the cell outline and define a Dirichlet boundary condition

$$\mathbf{q} = \mathbf{g}_v = S_B \begin{pmatrix} 2v_x^2 - 1 \\ v_x v_y \end{pmatrix}. \quad (9.33)$$

S_B is the scalar order parameter at the boundary.

On the concave parts Γ_2 of the boundary we introduce a weak anchoring energy expressed according to Eq. (9.28)

$$F_A = W \int_{\Gamma_2} \left| \mathbf{q} - S_B \begin{pmatrix} 2\tau_x^2 - 1 \\ \tau_x \tau_y \end{pmatrix} \right|^2 da, \quad (9.34)$$

which makes the surface tangent $\boldsymbol{\tau}$ the preferred alignment direction.

Around the MTOC we expect radial alignment, because here the minus-ends of the MTs are anchored and no direction should be preferred over another. In our model this is included by defining a ring around the cell centroid and setting up a strong anchoring according to Eq. (9.33) at this interior surface Γ_{MTOC} .

With all boundary conditions defined as above the full form of Eq. (9.32) now reads

$$\begin{aligned}
 \mathcal{F}[\mathbf{q}] &= \int_{\Omega} (\nabla \mathbf{q})^2 + \frac{1}{\varepsilon^2} (|\mathbf{q}|^2 - S_0^2)^2 dA + W \int_{\Gamma_2} |\mathbf{q} - \mathbf{g}_\tau|^2 da \\
 \mathbf{q} &= \mathbf{g}_\nu \quad \text{on } \Gamma_1 \\
 \mathbf{q} &= \mathbf{g}_\nu \quad \text{on } \Gamma_{\text{MTOC}} \\
 \text{with } \mathbf{g}_\nu &= S_B \begin{pmatrix} 2\nu_x^2 - 1 \\ \nu_x \nu_y \end{pmatrix}, \quad \mathbf{g}_\tau = S_B \begin{pmatrix} 2\tau_x^2 - 1 \\ \tau_x \tau_y \end{pmatrix}.
 \end{aligned} \tag{9.35}$$

9.5. Numerical implementation

Our aim is to obtain a Q-tensor field that corresponds to the minimum free energy configuration and extract the director field from it. This director field will be compared to the experimental orientation fields as well as the simulated fields obtained from the filament based models.

In principle various optimization methods could be used to minimize Eq. (9.35). One way is to discretize the simulation region and the equations on a regular, rectangular lattice and use the Monte Carlo method to find the minimum energy configuration [270]. The authors of this paper noted that the discretization of the elastic energy is not straight forward, because the discretized gradients could not be expressed as nearest neighbor differences. Also the metropolis algorithm, applied to perform the minimization, is computationally expensive if very fine discretizations and a large number of Monte Carlo steps are used.

An alternative way of obtaining the minimum energy configuration of \mathbf{Q} is to use the finite-element method (FEM). The FEM is a way to discretize a PDE and thereby allow to solve it numerically. As a starting point, the PDE is formulated as a variational problem by finding the weak formulation, which can be achieved by multiplying it with a test function v and integrating over the spatial domain. Then, integration by parts can be applied to obtain a linear variational problem.

An abstract formulation of such a variational problem is the following [271]. Given a space V of trial functions and a space \hat{V} of test functions, find $u \in V$ such that:

$$a(u, v) = L(v) \quad \forall v \in \hat{V}, \tag{9.36}$$

where $a(u, v)$ is a bilinear form (functional) containing the trial function u and a test function v and $L(v)$ a linear form. This variational problem still is infinitely-dimensional,

because of the continuous function spaces of test and trial functions.

A discretized problem can be constructed by restricting it to a set of discrete trial and test spaces [271]. Find $u_h \in V_h \subset V$

$$a(u_h, v) = L(v) \quad \forall v \in \hat{V}_h \subset \hat{V}. \quad (9.37)$$

Now, u_h can be expanded into a series by a set of basis functions $\{\phi_j\}_{j=1}^N$ and coefficients U_j . $\{\hat{\phi}_j\}_{j=1}^N$ forms a basis of the discrete test space \hat{V}_h . By this, the degrees of freedom U of the solution u_h can be computed through solving a linear system $AU = b$, with

$$\begin{aligned} A_{ij} &= a(\phi_i, \hat{\phi}_j), \quad i, j = 1, 2, \dots, N, \\ b_i &= L(\hat{\phi}_i). \end{aligned} \quad (9.38)$$

A key idea of the FEM is further to discretize the domain Ω on which the variational problem should be solved by a set of cells with disjoint interiors that form a mesh. On these cells local, finite-dimensional function space \mathcal{V} can be defined that can be used to construct the global, discretized function space V_h .

The formal definition of a finite element requires three components [271, 272]. A domain T , a local function space \mathcal{V} and a set of degrees of freedom \mathcal{L} . By defining a set of nodal basis functions $\{\phi_j\}_{j=1}^N$ for \mathcal{V} , any function $v \in \mathcal{V}$ can be expressed by evaluating the function v at the nodes x^j : $v = \sum_j v(x^j)\phi_j$. By considering smoothness constraints between neighboring finite elements one can map the local degrees of freedom to the global degrees of freedom and assemble the linear system in Eq. (9.38), which has to be solved in order to solve the variational problem.

For further aspects like the mapping of deformed finite elements to a reference element or the different classes of finite elements the reader is pointed to [271, 272] for a more detailed discussion.

Eq. (9.35) is nonlinear in (q, p) , so one cannot simply employ the formalism mentioned above. A formulation of a nonlinear variational problem is the following. Find $u \in V$ such that

$$F(u; v) = 0 \quad \forall v \in \hat{V}, \quad (9.39)$$

where $F(u; v)$ now is a semilinear form that is linear in the arguments after the semicolon. Solving such a problem is usually done by a Newton method, where the $F(u; v)$ is linearized around $u = u_h$ to obtain the linear form $F'(u_h; \delta u, v)$. Then at each newton step a

linear variational problem is solved according to: find $\delta u \in V_{h,0}$ such that

$$F'(u_h; \delta u, v) = F(u_h; v) \quad \forall v \in \hat{V}_h. \quad (9.40)$$

δu is then used to update u_h by

$$u_h^{k+1} = u_h^k - \delta u. \quad (9.41)$$

By the methods from the calculus of variations we can derive a minimizer for Eq. (9.35) that satisfies the following integral

$$0 = \int_{\Omega} \nabla \mathbf{q} \nabla \mathbf{v} + \frac{2}{\varepsilon^2} (\mathbf{q} \cdot \mathbf{q} - S_0^2) \mathbf{q} \cdot \mathbf{v} dA + W \int_{\Gamma_2} (\mathbf{q} - \mathbf{g}_\tau) \cdot \mathbf{v} da \quad \forall \mathbf{v} \in H^1(\Omega). \quad (9.42)$$

$\mathbf{v} \in H^1(\Omega)$ is a test function in the Sobolev space of L2-functions with square integrable derivatives up to first order [265]. A full derivation will be given in the appendix (Appendix A.3).

For the numerical implementation we used the open-source FEM package FEniCS [271], which provides algorithms for mesh-generation, discretization of minimizer, derivation of the Jacobian of Eq. (9.42) and for automated solution of the nonlinear variational problem by a Newton method. Some alternative FEM software packages are COMSOL Multiphysics [273], deal.II [274] or DUNE [275].

A weakness of Newton's method is that it strongly depends on initial conditions [265]. In order to obtain stable and reproducible solutions we start from an initial radial director configuration

$$\mathbf{Q}_0(\mathbf{r}) = S_0 (2\hat{\mathbf{r}}' \otimes \hat{\mathbf{r}}' - \mathbf{I}), \quad \text{with} \quad (9.43)$$

$$\hat{\mathbf{r}}' = \frac{\mathbf{r} - \mathbf{r}_0}{\|\mathbf{r} - \mathbf{r}_0\|}. \quad (9.44)$$

\mathbf{r}_0 is the position of the MTOC and the center of radial orientation. The surface anchoring parameter W was increased iteratively and at each step the minimum energy configuration was computed. This configuration was then used as the initial condition for the next iteration.

9.6. Influence of the parameters ε and W

Due to the scaling by the elastic constant L in Eq. (9.35), the elastic energy term now sets a reference and the thermotropic energy as well as the surface energy are scaled relative

to it. Due to the $1/\varepsilon^2$ scaling of the thermotropic energy, low values of ε force the system into the nematic regime and the term $\frac{1}{\varepsilon^2}(|\mathbf{q}|^2 - S_0^2)^2$ in Eq. (9.35) acts as a regularization term enforcing $|\mathbf{q}|^2 = S_0^2$ throughout the simulation domain [265]. For high values of ε the thermotropic potential is very shallow and $|\mathbf{q}|^2 \neq S_0^2$ can easily be achieved.

In a scan of the parameter space we observed two different kinds of behavior. The first one is a predominantly radial configuration with local tangential alignment at the boundaries, which is very similar to the experimental findings (Fig. 9.4a, lower left region). For an increase in W , $m = -1/2$ defects start to form at the convex boundaries that move into the bulk, a short distance away from the boundaries ($W = 2$, $\varepsilon = 2$ in Fig. 9.4a).

In the second case, for higher values of W and ε , one of the defects detaches from the convex boundaries and migrates fully into the bulk, which leads to asymmetric configurations ($W = 2.5$, $\varepsilon = 2$ in Fig. 9.4). If both defects detach from the boundary the configuration is even more unstable and both $m = -1/2$ defects will annihilate with the $m = 1$ defect that is fixed at the cell centroid to mimic the MTOC. The resulting orientation field then obtains an up-down configuration and the local radial alignment around to the MTOC does not get transmitted to the cell boundaries. The winding number around the outline of a cell on a ∇ -shaped MP is $m = 0$, so it is to be expected that two $m = -1/2$ defects form and also the annihilation with the $m = 1$ defect at the centroid can be understood in this way.

For the H and Y MP, similar patterns were found and $m = -1/2$ defects appear near the convex parts of the boundary and then move into the bulk. In the case of the Y MP, a $m = -1/2$ defect is retained at the center, because the winding number of the director around the boundary is $-1/2$ (Fig. 9.4b,c).

Comparing the various terms of Eq. (9.35) we found that the elastic energy was always the dominating term, being 5 to over 200 fold higher than the thermotropic energy in the given parameter range. The comparison of elastic energy to surface energy yielded factors from 2 to 60. A transition from the radial phase to the up-down phase always coincides with a significant decrease of the elastic energy and also often with a decrease of the surface energy. The thermotropic energy usually does not change upon such a transition.

Although such LC configurations are energetically favorable, their biological relevance is questionable. For example, the up-down configuration for the ∇ -shaped and H-shaped cells can hardly be explained by a MT network with minus-ends anchored to the centrosome. It might be possible to achieve such configurations in a *in vitro* system, where the MT network has no organizing aster, but for the mammalian we study here it seems unrealistic.

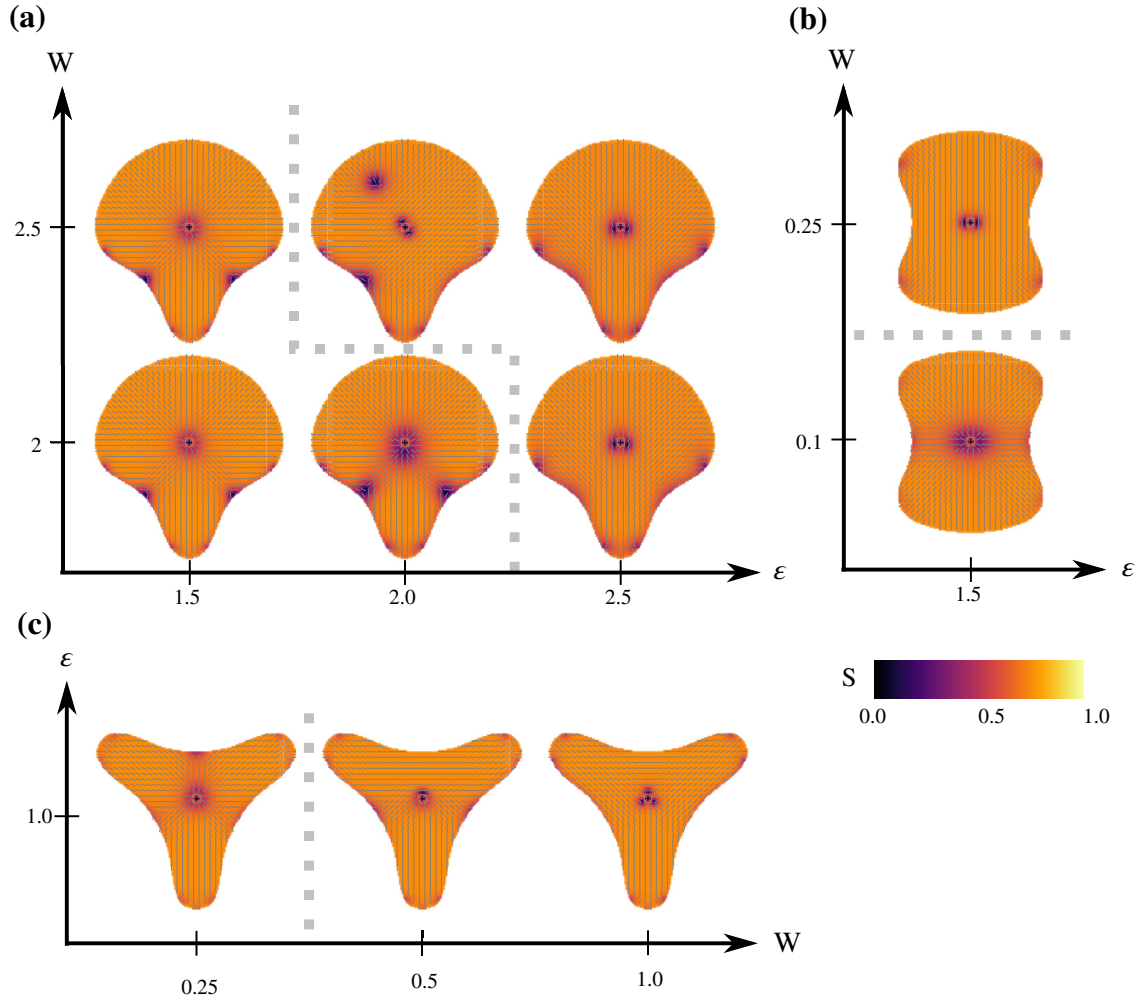


Figure 9.4.: Extract of the configuration space for different MP geometries. Orientation is symbolized by small oriented bars. Bulk order parameter $S_0 = 0.75$ for all plots. **(a)** Υ -shaped MP. Lower left part separated by dotted gray line: Radial configuration with local tangential anchoring at the convex boundaries and formation of $m = -1/2$ defects. ($\epsilon = 2, W = 2.5$): One defects has moved into the bulk leading to an asymmetric configuration. ($\epsilon = 2.5$): Both $m = -1/2$ defects have annihilated with the $m = 1$ defect at the cell center leading to an up-down configuration of the orientation field. Local tangential anchoring at the cell centroid cannot extend into the bulk anymore. **(b)** H-shaped MP: Similar transition from radial to up-down configuration. **(c)** Y-shaped MP: Absorption of one $m = -1/2$ defect from the top boundary is followed by absorption of the lower two defects, leading to an effective $m = -1/2$ defect at the centroid. Parameter axes are rotated.

9.7. Comparison to the experiments

To compare the LC model to the experiments, the model parameters were varied in the following way

LC model	Parameters	Description
	$\varepsilon \in [0.01, 10]$	Effective temperature
	$W \in [0.01, 1000]$	Surface anchoring strength at concave boundaries

For the LC model we find that the overlap between experimental and simulated orientation fields is comparable to the filament-based models, although slightly smaller. In Fig. 9.5a–c the experimental orientation fields for the three MP types are shown (red bars) with an overlay of the minimum free energy configuration of the LC model (blue bars). The cell outline is divided into convex (green) and concave (red) parts. The angle difference was split up into two sets of more parallel and more orthogonal directors (cf. Eq. (7.4)) and the set T_{\perp} (gray) highlights regions where the experimental fields and the simulations deviate by more than $\pi/4$.

As discussed earlier in Section 9.6, boundary defects start to form for an increase in the surface anchoring strength W . At certain values for the effective temperature ε and W , those defects detach from the surface, move into the bulk and eventually annihilate with the $m = +1$ defect at the cell center. This causes LC configurations that are energetically favorable. Due to the large regions of tangential alignment with the concave boundaries in those configurations, the overlap with experimental results is higher than for the situation of radial alignment around the MTOC. Nevertheless, we will exclude such configurations from the parameter estimation procedure, because they are biologically unrealistic.

Model MP	PRW			Cytosim			LC		
	\bar{s}	s_{\parallel}	s_{\perp}	\bar{s}	s_{\parallel}	s_{\perp}	\bar{s}	s_{\parallel}	s_{\perp}
\Uparrow	0.41	0.79	-0.68	0.51	0.76	-0.58	0.35	0.82	-0.73
H	0.46	0.79	-0.71	0.58	0.80	-0.56	0.45	0.74	-0.67
Y	0.72	0.86	-0.55	0.67	0.79	-0.57	0.68	0.92	-0.58

Table 9.1.: Average order parameters \bar{s} , s_{\parallel} and s_{\perp} for the comparison of orientation fields obtained by experimental analysis and computational modeling for all three models.

Fig. 9.5a–c shows director configurations for the parameters ($\varepsilon = 1.5$, $W = 2$) for the \Uparrow shaped MP, ($\varepsilon = 0.05$, $W = 100$) for the H and ($\varepsilon = 0.05$, $W = 200$) for Y-shaped cells that had the highest overlap with the experimental results (cf. Table 9.1). Fig. 9.5d

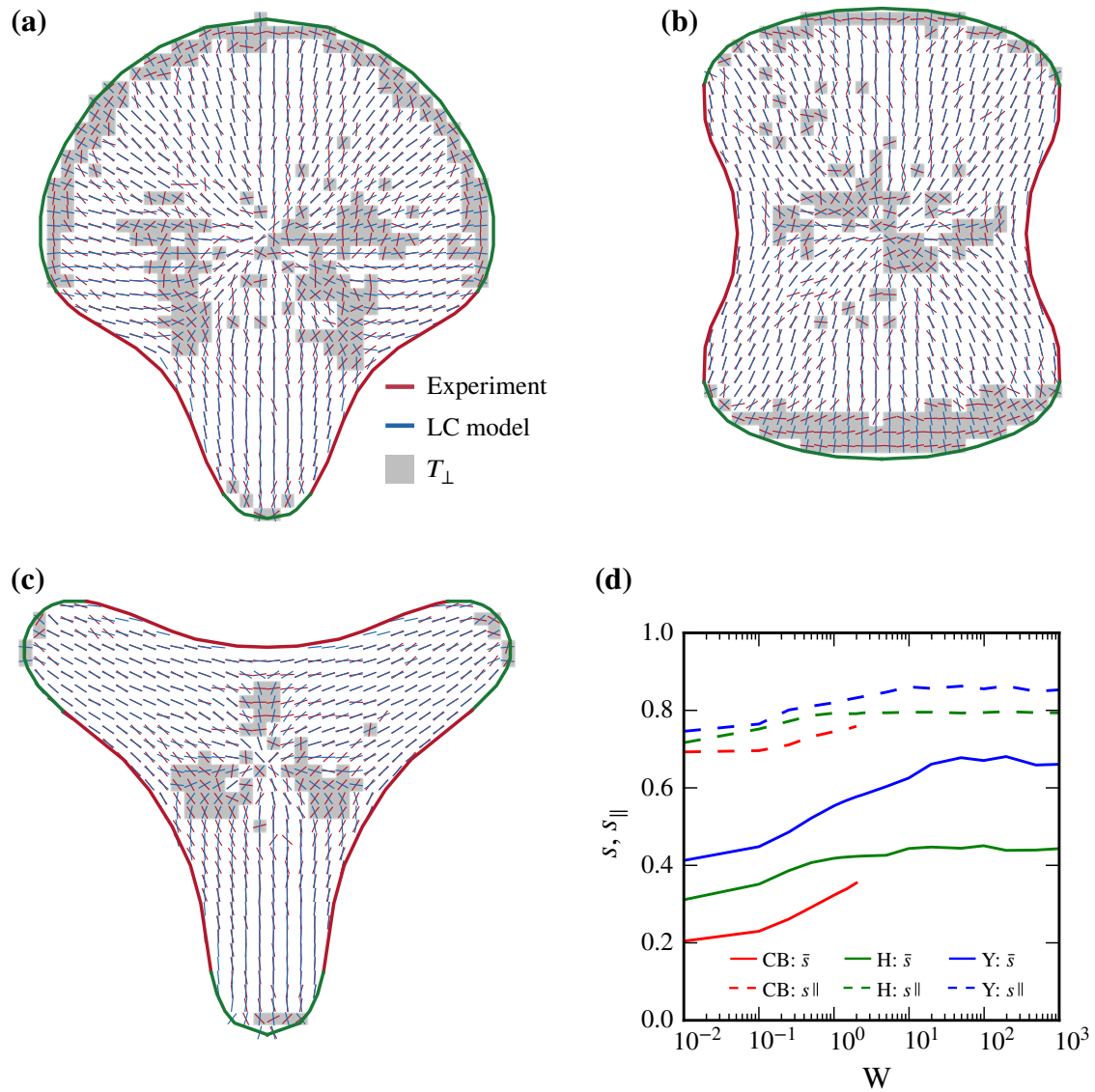


Figure 9.5.: Comparison of experimental and simulated MT orientation fields. **(a)** Overlay of experimental MT orientation field (red bars) and orientation simulated using the LC model (blue bars). Areas where the orientation differs by more than $\pi/4$ are shaded in gray (for definition of T_{\perp} see Eq. (7.4)). For parameters of LC model see main text. **(b) & (c)** Same as in (a), but for the H and Y MP. **(d)** Convergence plot of s and s_{\parallel} considering the difference of simulated and experimental orientation patterns for increasing surface anchoring strength W . Curve for ∇ -shaped MP is truncated, because it the model switches to the biologically unrealistic up-down configuration for $W > 2$ (see main text).

shows the trend for the order parameters s and s_{\parallel} for increasing surface anchoring strength W .

For the H and Y MP maximum overlap is reached for a configuration with low ϵ , deep in the nematic phase. Thus, the defects that form at the convex boundaries stay localized there and do not annihilate with the $m = +1$ defect at the cell centroid, even for further increase of W . For $W > 200$ the order parameters reaches a plateau and no further improvement in the overlap between experiments and theory can be achieved. Larger overlap is only possible for the excluded, unrealistic configurations.

Orientation fields with local tangential anchoring as discussed for the Cytosim simulations in Section 8.2.4 cannot be achieved with the current LC model. Such a tangential alignment results from filaments growing along the convex boundaries and would have to be realized in the LC model only in terms of boundary conditions. If tangential orientation would be introduced as the easy-direction at the boundary, it would also translate into the interior of the simulation domain and the radial alignment around the MTOC would be confined to a very small region. Examples for such configurations are shown in Fig. 9.6 and are not more realistic than the up-down configurations that were excluded earlier.

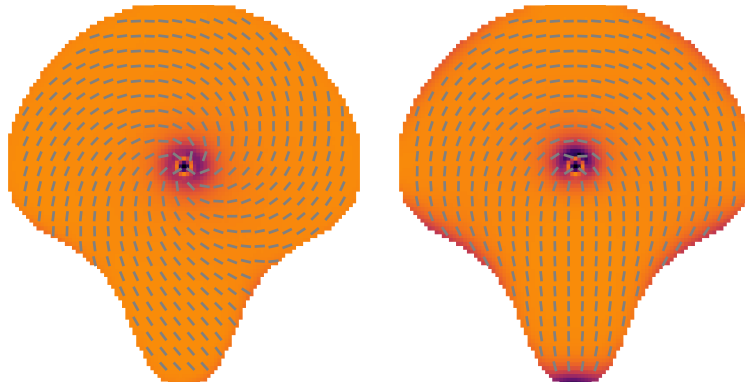


Figure 9.6.: Two configurations of the director field for weak tangential anchoring at the complete boundary. Radial alignment around the cell centroid only has local effect.

9.8. Liquid crystal model compared to filament-based models

The agreement between the LC model and the filament based models can only be assessed in terms of the orientation fields. We therefore searched for a maximum in the angular

difference order parameter s for all combinations of the parameter sets. As before, for the comparison with the experiments, we excluded LC configurations in which the radial anchoring at the cell centroid vanished due to annihilation of the defects that form at the boundaries. The ∇ -shaped MP was used as a reference.

The best match between the LC model and the PRW model could be obtained for ($\varepsilon = 1.0$, $W = 5.0$) and ($l_p = 120 \mu\text{m}$, $\omega_r = 0.064 \text{ s}^{-1}$). This parameter set for the LC model is close to the transition point, where the boundary defects that form close to the concave boundaries start to move into the bulk. An increase of the effective temperature to $\varepsilon = 1.5$ induces this transition.

The LC model agrees best with Cytosim for the LC model parameters ($\varepsilon = 1.0$, $W = 0.5$) and the Cytosim parameters ($l_p = 500 \mu\text{m}$, $\omega_a^+ = 1.0 \text{ s}^{-1}$, $\omega_a^- = 0.5 \text{ s}^{-1}$). Here, for a wide range of parameters for both models a high order parameter ($\bar{s} > 0.9$), but for smaller ω_a^+ the overlap decreases. This is caused again by the filaments that are being bent at the convex boundaries of the Cytosim simulation domain and cause tangential alignment there. With the LC model such a configuration cannot be achieved, as mentioned earlier, which explains the lower value for s .

The minimum energy configurations of the LC model that match best with the filament based models are similar to the ones discussed upon comparing it to experimental orientation fields. The highest agreement can be found for parameter values that induce the formation of defects slightly detached from the concave boundaries. Such a configuration, however, is sensitive to parameter changes and an increase in the effective temperature ε or surface anchoring strength W can lead to configurations where one or multiple defects annihilate with the defect at the centroid of the simulation domain. Such a LC director field might be energetically favorable and interesting to investigate further, but for the purpose of predicting the MT network it is less suited.

We therefore suggest to choose parameters from the regime where the defects are still located near the concave boundaries. With such parameters, the agreement with experimental data and the filament based models is still very good and the LC model provides an excellent way to predict the organization of the MT network within cells on MP substrates.

9.9. Conclusion

In this chapter we developed an effective continuum description of the MT network based on the theory of LCs. We considered the system from a more abstract point of view and

described the microscopic interactions of MTs terms of a continuous order parameter, from which we extracted an orientation field. With this model we are able to capture most of the experimental observations. One feature such a model cannot represent is the tangential alignment of MTs at convex parts of the cell outline, because the bulk configuration is determined by the boundary conditions. If we consider tangential alignment as a local effect, our proposed model can nevertheless predict the MT configuration in the cell interior.

A large advantage of this framework is that it is computationally cheap compared to Brownian dynamics simulations. If one is only interested in studying the organization of a reference cell by utilizing the normalization properties of MP substrates, it can make predictions for arbitrarily shaped cells with little effort. Therefore, it could be combined with a model for cell shape, such as the cellular Potts model [119], to predict cell shape and intracellular orientation. Such a coupling could either be realized by using simulated cell shape as an initial condition for the LC model or by including hydrodynamic effects into the LC theory to directly influence the cell shape model, e.g. by defining a polarization direction of the cell.

10

Conclusion

The aim of this thesis was to develop image analysis methods to study cellular organization and combine these techniques with mathematical modeling in order to gain a deeper understanding of cellular behavior. The unifying component for this work was the use of micropatterned environments, which control cell shape and normalize intracellular organization. Thereby, image analysis is facilitated, but such environments also have interesting effects on cellular structure that help to gain a deeper understanding in the physical processes that determine cellular organization

Chapter 3 was dedicated to the study of the actin cytoskeleton. There, we analyzed the shape of peripheral stress fibers that span between adhesion sites of the cell to the substrate. We presented an image processing workflow that detects circular arcs along the cell contour in a fully automated fashion and fits circles to these arcs by optimizing their overlap with fluorescently labeled stress fibers. By fitting the extracted parameters to the tension-elasticity model, we could quantify that the HeLa cells used in the experiments form weaker stress fibers compared to different cell lines used in earlier work.

Then, we extended the analysis of cell shape into three dimensions. We fitted circular arcs to stress fibers of cells that were adhering in microscavolds fabricated by direct laser writing. We could show that stress fibers form at distinct regions of the cell and could quantify their radius of curvature and spanning distance. We used our results to configure a computational model based on contractile cables and showed that such a model explains the shape of cells in three dimensional microscavolds in a quantitative way. A conclusion of this is, that the similar physical principles govern cell shape in two and three dimensions.

Next, we had a closer look at the microstructure of stress fibers by analyzing images that were obtained by structured illumination microscopy. In these images, the individual

force generating units of stress fibers, myosin II minifilaments, could be resolved and we developed a workflow to measure their location along the fibers. Furthermore, we outlined how this quantitative information can be incorporated into future modeling efforts.

In Chapter 4 investigated intracellular dynamics of the actin cytoskeleton, which was controlled by light-induced stimulation and the use of optogenetics. For this, we applied an optical flow algorithm and measured cytoskeletal velocity fields. The resulting flow patterns were linked to the orientation of the actin cytoskeleton and by this, we could show that stress fibers are the main contributors for cellular contraction dynamics. We observed characteristic backflow after the external stimulation ceased and could explain this by the stretching of elastic components of the stress fiber. We compared our analysis results to mathematical models could show that the protein zyxin is required for maintaining the elasticity of stress fibers.

In Chapter 5 we analyzed to organization of the microtubule network in cells on micropatterned substrates. We measured the orientation of microtubules and utilized the normalization of cell shape by the substrate to calculate averaged orientation fields of the microtubule network. We found different alignment of the microtubules at peripheral stress in comparison to region where the cell adheres to the substrate. This leads to new insights in the coordination between microtubules and the actin cytoskeleton, that we further investigated by computational modeling in the second part of the thesis.

The first part of the thesis was completed in Chapter 6 by the development of image analysis methods to quantify the distribution of intracellular vesicles. We utilized the shape normalization properties of the micropatterned substrates to develop a workflow that extracts spatial distribution maps of fluorescently labeled intracellular structures. We applied this workflow to experimental data, in which gene expression was modified by RNA interference. With our analysis method we were able to statistically assess differences in the intracellular accumulation of integrin signaling proteins, depending on gene knockdown. Such an analysis method, in combination with micropatterned substrates, can also be used in high-throughput screens and will provide meaningful results with less effort than conventional techniques.

In the second part of the thesis we focus on computational modeling of the organization of the microtubule network in cells on micropatterned substrates. In Chapter 8 we present two approaches that are based either on the simulation of polymers by a persistent random walk or on Brownian dynamics simulations with the software Cytosim. For bot cases we motivated interactions with the cell boundaries based on our experimental results.

With the conceptually simple persistent random walk model, we could capture most

of the experimentally observed behavior and related the model parameters to measured values for the microtubule rigidity.

In the Cytosim simulations we implemented more detailed interactions with the cell boundary by a mechanisms of dynamic binding and unbinding of microtubule tips. By this, we could explain the experimentally observed tangential alignment of microtubules in regions where the cell adheres to the micropatterned substrate. Based on our model predictions, we proposed further experimental work to investigate the effects we observed by image analysis and modeling.

In Chapter 9 we developed an effective continuum description of the organization of the microtubule network, based on the theory of nematic liquid crystals. We defined a free energy functional and motivated suitable boundary conditions to model the orientation of the microtubule network in cells on micropatterned substrates. We minimized the functional using the finite-element method and compared the predicted orientation fields to experimental results and the aforementioned models. This framework captures all relevant effects for the organization of the microtubule network on the level of the whole cell. Furthermore, we gave an outlook on how to combine our model for intracellular organization with other models that predict cell shape.

In conclusion, this thesis demonstrates how an interplay between the normalization of cellular organization by micropatterned substrates, suitable image analysis techniques and mathematical modeling leads to novel insights in cellular behavior.



Appendix

A.1. Parameters for the persistent random walk simulations

Parameter	Value	Comment, reference
MT segment length	$\Delta\xi = 65 \text{ nm}$	
Time step	$\Delta t = 1 \text{ s}$	
Persistence length	$l_p \in [30 \mu\text{m}, 3000 \mu\text{m}]$	[91]: $30 \mu\text{m}$; [63]: $l_p = 5200 \mu\text{m}$
Polymerization speed	$v_+ = 0.13 \mu\text{m/s}$	[239]
Depolymerization speed	$v_- = 0.26 \mu\text{m/s}$	[239]
Rescue rate	$\omega_r \in \{0.0 \text{ s}^{-1}, 0.064 \text{ s}^{-1}\}$	[239]: 0.064 s^{-1}
Catastrophe rate	$\omega_c \in \{0, 1\}$	0 at convex boundaries; 1 at concave boundaries

A.2. Parameters for the Cytosim simulations

Parameter	Value	Comment, reference
MT rigidity	$k_B T l_p \in [0.0126 \text{ pN}\mu\text{m}^2, 1.26 \text{ pN}\mu\text{m}^2]$	Corresponds to $l_p \in [30 \mu\text{m}, 3000 \mu\text{m}]$
Polymerization speed	$v_+ = 0.13 \mu\text{m/s}$	[239]
Depolymerization speed	$v_- = 0.27 \mu\text{m/s}$	[239]
Rescue rate	$\omega_r = 0.064 \text{ s}^{-1}$	[239]
Stall force	5 pN	[276]
Catastrophe rate	$\omega_c \in \{0.01 \text{ s}^{-1}, 0.04 \text{ s}^{-1}\}$	Unloaded catastrophe rate and stalled catastrophe rate [231]
Number of MTs	$N_{\text{MT}} = 100$	[233]
Radius of centrosome	0.5 μm	Fixed at cell centroid
bead		
Anchoring stiffness	1000 μm , 500 μm	Anchoring stiffness to the center and the outer of the centrosome bead
Viscosity	0.1 pN/ μm^2	Effective viscosity of the cytoplasm [277]
Binding rate to cell cortex	$\omega_a^+ \in [0.025 \text{ s}^{-1}, 1 \text{ s}^{-1}]$	Varied for fitting to experiments and other models
Unbinding rate from cell cortex	$\omega_a^- \in [0.025 \text{ s}^{-1}, 0.5 \text{ s}^{-1}]$	

A.3. Derivation of the minimizer of the Landau–de Gennes free energy

To derive the minimizer of the the Landau–de Gennes free energy

$$\mathcal{F}[\mathbf{q}] = \int_{\Omega} (\nabla \mathbf{q})^2 + \frac{1}{\varepsilon^2} (|\mathbf{q}|^2 - S_0)^2 dA + W \int_{\Gamma_2} |\mathbf{q} - \mathbf{g}|^2 da,$$

we use the calculus of variation and obtain

$$\begin{aligned} \delta \mathcal{F}[\mathbf{q}, \mathbf{v}] &= \left[\frac{d}{d\alpha} \mathcal{F}[\mathbf{q} + \alpha \mathbf{v}] \right]_{\alpha=0} \\ &= \left[\frac{d}{d\alpha} \left\{ \int_{\Omega} (\nabla (\mathbf{q} + \alpha \mathbf{v}))^2 + \frac{1}{\varepsilon^2} (|\mathbf{q} + \alpha \mathbf{v}|^2 - S_0)^2 dA + W \int_{\Gamma_2} |\mathbf{q} + \alpha \mathbf{v} - \mathbf{g}|^2 da \right\} \right]_{\alpha=0} \\ &= \left[\frac{d}{d\alpha} \left\{ \int_{\Omega} (\nabla \mathbf{q})^2 + 2\alpha (\nabla \mathbf{q})(\nabla \mathbf{v}) + \alpha^2 (\nabla \mathbf{v})^2 dA \right. \right. \\ &\quad \left. \left. + \int_{\Omega} \frac{1}{\varepsilon^2} (|\mathbf{q}|^2 + 2\alpha \mathbf{q} \cdot \mathbf{v} + \alpha^2 |\mathbf{v}|^2 - S_0)^2 dA \right. \right. \\ &\quad \left. \left. + W \int_{\Gamma_2} |\mathbf{q}|^2 + 2\alpha \mathbf{v} \cdot (\mathbf{q} - \mathbf{g}) - 2\mathbf{q} \cdot \mathbf{g} + \alpha^2 |\mathbf{v}|^2 da \right\} \right]_{\alpha=0} \\ &= \left[\int_{\Omega} 2(\nabla \mathbf{q})(\nabla \mathbf{v}) + 2\alpha (\nabla \mathbf{v})^2 dA \right. \\ &\quad \left. + \int_{\Omega} \frac{2}{\varepsilon^2} (2\mathbf{q} \cdot \mathbf{v} + 2\alpha |\mathbf{v}|^2) (|\mathbf{q}|^2 + 2\alpha \mathbf{q} \cdot \mathbf{v} + \alpha^2 |\mathbf{v}|^2 - S_0) dA \right. \\ &\quad \left. + W \int_{\Gamma_2} 2\mathbf{v} \cdot (\mathbf{q} - \mathbf{g}) + 2\alpha |\mathbf{v}|^2 da \right]_{\alpha=0} \\ &= 2 \int_{\Omega} \nabla \mathbf{q} \cdot \nabla \mathbf{v} + \frac{2}{\varepsilon^2} (\mathbf{q} \cdot \mathbf{q} - S_0^2) \mathbf{q} \cdot \mathbf{v} dA + W \int_{\Gamma_2} (\mathbf{q} - \mathbf{g}) \cdot \mathbf{v} da. \end{aligned}$$

This is the minimizer used in Eq. (9.42).

A.4. Parameters for the liquid crystal model

Parameter	Value	Comment
ε	$\in [0.01, 10]$	Effective temperature
W	$\in [0.01, 1000]$	Surface anchoring strength at concave boundaries
S_0	0.75	Bulk order parameter
S_B	0.75	Boundary order parameter
r_{MTOC}	1 μm	Radius of circle around the centroid, which defines radial anchoring

Bibliography

- [1] Alberts, B. et al. *Molecular Biology of the Cell*. Garland Science (2007) (Referenced on pp. 1, 9–11, 14, 15, 17).
- [2] Boas, D. A., Pitris, C., and Ramanujam, N. *Handbook of Biomedical Optics*. CRC Press (2011) (Referenced on pp. 2, 4).
- [3] Demtröder, W. *Experimentalphysik 2*. Springer (2013) (Referenced on p. 3).
- [4] Gustafsson, M. G. L. “Nonlinear structured-illumination microscopy: wide-field fluorescence imaging with theoretically unlimited resolution.” *Proceedings of the National Academy of Sciences* 102, 37 (2005) (Referenced on p. 3).
- [5] Huang, B., Bates, M., and Zhuang, X. “Super-Resolution Fluorescence Microscopy”. *Annual Review of Biochemistry* 78, 1 (2009) (Referenced on pp. 2–4).
- [6] Hell, S. W. et al. “Confocal microscopy with an increased detection aperture: type-B 4Pi confocal microscopy.” *Optics Letters* 19, 3 (1994) (Referenced on p. 2).
- [7] Gustafsson, M. G. L. “Surpassing the lateral resolution limit by a factor of two using structured illumination microscopy”. *Journal of Microscopy* 198, 2 (2000) (Referenced on p. 2).
- [8] Cornea, A. and Conn, M. P. *Fluorescence Microscopy*. Elsevier, Academic Press (2014) (Referenced on pp. 2, 4).
- [9] Nobelprize.org. *The Nobel Prize in Chemistry 2014*. URL: https://www.nobelprize.org/nobel_prizes/chemistry/laureates/2014/ (visited on 10/13/2016) (Referenced on p. 3).
- [10] Hell, S. W. and Wichmann, J. “Breaking the diffraction resolution limit by stimulated emission: stimulated-emission-depletion fluorescence microscopy”. *Optics Letters* 19, 11 (1994) (Referenced on p. 3).
- [11] Leica Microsystems. *Leica TCS SP8 STED 3X*. URL: <http://www.leica-microsystems.com/products/confocal-microscopes/details/product/leica-tcs-sp8-sted-3x/> (visited on 10/17/2016) (Referenced on p. 4).
- [12] Betzig, E. et al. “Imaging intracellular fluorescent proteins at nanometer resolution.” *Science* 313, 5793 (2006) (Referenced on p. 4).
- [13] Moerner, W. E. and Fromm, D. P. “Methods of single-molecule fluorescence spectroscopy and microscopy”. *Review of Scientific Instruments* 74, 8 (2003) (Referenced on p. 4).

- [14] Rust, M. J., Bates, M., and Zhuang, X. W. "Sub-diffraction-limit imaging by stochastic optical reconstruction microscopy (STORM)". *Nature Methods* 3, 10 (2006) (Referenced on p. 4).
- [15] Voie, A. H., Burns, D. H., and Spelman, F. A. "Orthogonal-plane fluorescence optical sectioning: three-dimensional imaging of macroscopic biological specimens." *Journal of Microscopy* 170, 3 (1993) (Referenced on p. 4).
- [16] Huisken, J. et al. "Optical sectioning deep inside live embryos by selective plane illumination microscopy." *Science* 305, 5686 (2004) (Referenced on p. 4).
- [17] Kourkoutis, L. F., Plitzko, U. M., and Baumeister, W. "Electron Microscopy of Biological Materials at the Nanometer Scale". *Annu. Rev. Mater. Res* 42 (2012) (Referenced on p. 4).
- [18] Moffat, J. and Sabatini, D. M. "Building mammalian signalling pathways with RNAi screens". *Nature Reviews. Molecular Cell Biology* 7, 3 (2006) (Referenced on pp. 4, 42).
- [19] Théry, M. "Micropatterning as a tool to decipher cell morphogenesis and functions." *Journal of Cell Science* 123, Pt 24 (2010) (Referenced on p. 5).
- [20] Chen, C. S. et al. "Micropatterned Surfaces for Control of Cell Shape, Position, and Function". *Biotechnology Progress* 14, 3 (1998) (Referenced on p. 5).
- [21] Bischofs, I. B. et al. "Filamentous Network Mechanics and Active Contractility Determine Cell and Tissue Shape". *Biophysical Journal* 95, 7 (2008) (Referenced on pp. 5, 21, 22, 41, 45, 49, 50).
- [22] Théry, M. et al. "Cell distribution of stress fibres in response to the geometry of the adhesive environment". *Cell Motility and the Cytoskeleton* 63, 6 (2006) (Referenced on pp. 5, 6, 21).
- [23] Singhvi, R. et al. "Engineering cell shape and function". *Science* 264, 5159 (1994) (Referenced on p. 5).
- [24] Ruiz, S. A. and Chen, C. S. "Microcontact printing: A tool to pattern". *Soft Matter* 3, 2 (2006) (Referenced on p. 5).
- [25] Qin, D., Xia, Y., and Whitesides, G. M. "Soft lithography for micro- and nanoscale patterning." *Nature Protocols* 5, 3 (2010) (Referenced on pp. 5, 6).
- [26] Palchesko, R. N. et al. "Development of Polydimethylsiloxane Substrates with Tunable Elastic Modulus to Study Cell Mechanobiology in Muscle and Nerve". *PLoS ONE* 7, 12 (2012) (Referenced on p. 5).
- [27] Ashby, M. F. *Materials Selection in Mechanical Design*. Elsevier (2005) (Referenced on p. 5).
- [28] Fink, J. et al. "Comparative study and improvement of current cell micro-patterning techniques." *Lab on a chip* 7, 6 (2007) (Referenced on p. 6).
- [29] CYTOO SA. CYTOO. URL: www.cytoo.com (visited on 09/02/2016) (Referenced on p. 6).

- [30] Chen, C. S. et al. "Geometric control of cell life and death." *Science* 276, 5317 (1997) (Referenced on p. 6).
- [31] McBeath, R. et al. "Cell shape, cytoskeletal tension, and RhoA regulate stem cell lineage commitment". *Developmental Cell* 6, 4 (2004) (Referenced on p. 6).
- [32] Guilak, F. et al. "Control of Stem Cell Fate by Physical Interactions with the Extracellular Matrix". *Cell Stem Cell* 5, 1 (2009) (Referenced on p. 6).
- [33] Kilian, K. A. et al. "Geometric cues for directing the differentiation of mesenchymal stem cells." *Proceedings of the National Academy of Sciences* 107, 11 (2010) (Referenced on p. 6).
- [34] Théry, M. et al. "The extracellular matrix guides the orientation of the cell division axis." *Nature Cell Biology* 7, 10 (2005) (Referenced on p. 6).
- [35] Théry, M. et al. "Anisotropy of cell adhesive microenvironment governs cell internal organization and orientation of polarity". *Proceedings of the National Academy of Sciences* 103, 52 (2006) (Referenced on pp. 6, 7, 71, 73, 74, 77, 89, 99, 102, 116).
- [36] Lee, J., Cuddihy, M. J., and Kotov, N. A. "Three-dimensional cell culture matrices: state of the art." *Tissue Engineering: Part B* 14, 1 (2008) (Referenced on pp. 7, 8).
- [37] Hunt, N. C. and Grover, L. M. "Cell encapsulation using biopolymer gels for regenerative medicine". *Biotechnology Letters* 32, 6 (2010) (Referenced on p. 7).
- [38] Li, M. L. et al. "Influence of a reconstituted basement membrane and its components on casein gene expression and secretion in mouse mammary epithelial cells." *Proceedings of the National Academy of Sciences* 84, 1 (1987) (Referenced on p. 7).
- [39] Lin, J.-y. et al. "Morphology and organization of tissue cells in 3D microenvironment of monodisperse foam scaffolds". *Soft Matter* 7, 21 (2011) (Referenced on p. 8).
- [40] Lo, Y.-P. et al. "Three-dimensional spherical spatial boundary conditions differentially regulate osteogenic differentiation of mesenchymal stromal cells". *Scientific Reports* 6, February (2016) (Referenced on p. 8).
- [41] Warnke, P. et al. "Growth and transplantation of a custom vascularised bone graft in a man". *Lancet* 364, 9436 (2004) (Referenced on p. 8).
- [42] Murphy, S. V. and Atala, A. "3D bioprinting of tissues and organs." *Nature Biotechnology* 32, 8 (2014) (Referenced on p. 8).
- [43] Soukoulis, C. M., Linden, S., and Wegener, M. "Negative Refractive Index at Optical Wavelengths". *Science* 315, 5808 (2007) (Referenced on p. 8).
- [44] Rill, M. S. et al. "Photonic metamaterials by direct laser writing and silver chemical vapour deposition". *Nature Materials* 7, 7 (2008) (Referenced on p. 8).

- [45] Dolling, G. et al. “Negative-index metamaterial at 780 nm wavelength”. *Optics Letters* 32, 1 (2007) (Referenced on p. 8).
- [46] Enoch, S. et al. “A Metamaterial for Directive Emission”. *Physical Review Letters* 89, 21 (2002) (Referenced on p. 8).
- [47] Zhang, X. and Liu, Z. “Superlenses to overcome the diffraction limit”. *Nature Materials* 7, 6 (2008) (Referenced on p. 8).
- [48] Schurig, D. et al. “Metamaterial electromagnetic cloak at microwave frequencies.” *Science* 314, 5801 (2006) (Referenced on p. 8).
- [49] Klein, F. et al. “Elastic fully three-dimensional microstructure scaffolds for cell force measurements”. *Advanced Materials* 22, 8 (2010) (Referenced on pp. 8, 29, 46).
- [50] Klein, F. et al. “Two-component polymer scaffolds for controlled three-dimensional cell culture”. *Advanced Materials* 23, 11 (2011) (Referenced on p. 8).
- [51] Richter, B. et al. “Three-dimensional microscaffolds exhibiting spatially resolved surface chemistry”. *Advanced Materials* 25, 42 (2013) (Referenced on p. 8).
- [52] Scheiwe, A. C. et al. “Subcellular stretch-induced cytoskeletal response of single fibroblasts within 3D designer scaffolds”. *Biomaterials* 44 (2015) (Referenced on p. 8).
- [53] Milo, R. and Phillips, R. *Cell Biology by the Numbers*. Garland Science (2015) (Referenced on p. 9).
- [54] Wikimedia Commons. *The cells of eukaryotes (left) and prokaryotes (right)*. URL: <https://commons.wikimedia.org/wiki/File:Celltypes.svg> (visited on 09/13/2016) (Referenced on p. 10).
- [55] Fletcher, D. A. and Mullins, R. D. “Cell mechanics and the cytoskeleton”. *Nature* 463, 7280 (2010) (Referenced on p. 11).
- [56] Huber, F. et al. “Cytoskeletal crosstalk: When three different personalities team up”. *Current Opinion in Cell Biology* 32 (2015) (Referenced on pp. 11, 12, 17).
- [57] Phillips, R. et al. *Physical Biology of the Cell*. Garland Science (2013) (Referenced on pp. 12, 13).
- [58] Howard, J. *Mechanics of Motor Proteins and the Cytoskeleton*. Sinauer Associates (2001) (Referenced on p. 12).
- [59] Dominguez, R. and Holmes, K. C. “Actin structure and function.” *Annual Review of Biophysics* 40 (2011) (Referenced on p. 12).
- [60] Halliburton, W. “On muscle-plasma”. *Journal of Physiology* 8 (1887) (Referenced on p. 12).
- [61] Szent-Györgyi, A. “Studies on muscle”. *Acta Physiologica Scandinavica* 9, 25 (1945) (Referenced on p. 12).

-
- [62] Straub, F. B. and Feuer, G. "Adenosinetriphosphate. The functional group of actin." *Biochimica et Biophysica Acta* 4 (1950) (Referenced on p. 12).
- [63] Gittes, F. et al. "Flexural rigidity of microtubules and actin filaments measured from thermal fluctuations in shape". *Journal of Cell Biology* 120, 4 (1993) (Referenced on pp. 13, 14, 17, 108, 145).
- [64] Blanchoin, L. et al. "Actin dynamics, architecture, and mechanics in cell motility". *Physiological reviews* 94, 1 (2014) (Referenced on pp. 13, 14).
- [65] Pollard, T. D. and Borisy, G. G. "Cellular motility driven by assembly and disassembly of actin filaments." *Cell* 112, 4 (2003) (Referenced on p. 13).
- [66] Burridge, K. "Focal Adhesions: Transmembrane Junctions Between The Extracellular Matrix And The Cytoskeleton". *Annual Review of Cell and Developmental Biology* 4, 1 (1988) (Referenced on p. 14).
- [67] Balaban, N. Q. et al. "Force and focal adhesion assembly: a close relationship studied using elastic micropatterned substrates". *Nature Cell Biology* 3, 5 (2001) (Referenced on pp. 14, 19).
- [68] Schwarz, U. S. et al. "Calculation of forces at focal adhesions from elastic substrate data: the effect of localized force and the need for regularization." *Biophysical Journal* 83, 3 (2002) (Referenced on pp. 14, 19).
- [69] Hotulainen, P. and Lappalainen, P. "Stress fibers are generated by two distinct actin assembly mechanisms in motile cells". *Journal of Cell Biology* 173, 3 (2006) (Referenced on p. 14).
- [70] Peterson, L. J. et al. "Simultaneous Stretching and Contraction of Stress Fibers In Vivo". *Molecular Biology of the Cell* 15, July (2004) (Referenced on pp. 14, 64).
- [71] Dogterom, M. and Surrey, T. "Microtubule organization in vitro". *Current Opinion in Cell Biology* 25, 1 (2013) (Referenced on p. 15).
- [72] Borisy, G. G. and Taylor, E. W. "The mechanism of action of colchicine. Colchicine binding to sea urchin eggs and the mitotic apparatus." *Journal of Cell Biology* 34, 2 (1967) (Referenced on p. 14).
- [73] Borisy, G. G. and Taylor, E. W. "The mechanism of action of colchicine. Binding of colchicine-3H to cellular protein." *Journal of Cell Biology* 34, 2 (1967) (Referenced on p. 14).
- [74] Brady, S. T. "A novel brain ATPase with properties expected for the fast axonal transport motor." *Nature* 317, 6032 (1985) (Referenced on p. 14).
- [75] Vale, R. D., Reese, T. S., and Sheetz, M. P. "Identification of a novel force-generating protein, kinesin, involved in microtubule-based motility". *Cell* 42, 1 (1985) (Referenced on p. 14).
- [76] Scholey, J. M. et al. "Identification of kinesin in sea urchin eggs, and evidence for its localization in the mitotic spindle". *Nature* 318, 6045 (1985) (Referenced on p. 14).

- [77] Paschal, B. M. and Vallee, R. B. “Retrograde transport by the microtubule-associated protein MAP 1C”. *Nature* 330, 6144 (1987) (Referenced on p. 14).
- [78] Lye, R. J. et al. “Identification of a microtubule-based cytoplasmic motor in the nematode *C. elegans*”. *Cell* 51, 2 (1987) (Referenced on p. 14).
- [79] Mitchison, T. and Kirschner, M. “Dynamic instability of microtubule growth.” *Nature* 312, 5991 (1984) (Referenced on p. 14).
- [80] Bornens, M. “Organelle positioning and cell polarity.” *Nature Reviews. Molecular Cell Biology* 9, 11 (2008) (Referenced on p. 15).
- [81] Tang, N. and Marshall, W. F. “Centrosome positioning in vertebrate development”. *Journal of Cell Science* 125, 21 (2012) (Referenced on p. 15).
- [82] Lodish, H. et al. *Molecular Cell Biology*. Freeman Macmillan Higher Education (2013) (Referenced on p. 16).
- [83] Etienne-Manneville, S. “Microtubules in cell migration.” *Annual Review of Cell and Developmental Biology* 29 (2013) (Referenced on p. 16).
- [84] Stehbens, S. and Wittmann, T. “Targeting and transport: How microtubules control focal adhesion dynamics”. *Journal of Cell Biology* 198, 4 (2012) (Referenced on p. 16).
- [85] Kaverina, I., Krylyshkina, O., and Small, J. V. “Microtubule targeting of substrate contacts promotes their relaxation and dissociation”. *Journal of Cell Biology* 146, 5 (1999) (Referenced on p. 16).
- [86] Kaverina, I., Rottner, K., and Small, J. V. “Targeting, capture, and stabilization of microtubules at early focal adhesions”. *Journal of Cell Biology* 142, 1 (1998) (Referenced on p. 16).
- [87] Conde, C. and Cáceres, A. “Microtubule assembly, organization and dynamics in axons and dendrites.” *Nature Reviews. Neuroscience* 10, 5 (2009) (Referenced on p. 16).
- [88] Waterman-Storer, C. M. and Salmon, E. D. “Actomyosin-based retrograde flow of microtubules in the lamella of migrating epithelial cells influences microtubule dynamic instability and turnover and is associated with microtubule breakage and treadmilling”. *Journal of Cell Biology* 139, 2 (1997) (Referenced on p. 16).
- [89] Herrmann, H. et al. “Intermediate filaments: from cell architecture to nanomechanics”. *Molecular Cell Biology* 8, 7 (2007) (Referenced on p. 17).
- [90] Brangwynne, C. P. et al. “Nonequilibrium microtubule fluctuations in a model cytoskeleton”. *Physical Review Letters* 100, 11 (2008) (Referenced on pp. 17, 90).
- [91] Brangwynne, C. P., MacKintosh, F. C., and Weitz, D. A. “Force fluctuations and polymerization dynamics of intracellular microtubules.” *Proceedings of the National Academy of Sciences* 104, 41 (2007) (Referenced on pp. 17, 90, 98, 103, 108, 115, 145).

-
- [92] Akhmanova, A. and Steinmetz, M. O. "Microtubule +TIPs at a glance". *Journal of Cell Science* 123, 20 (2010) (Referenced on p. 17).
- [93] Matov, A. et al. "Analysis of microtubule dynamic instability using a plus-end growth marker." *Nature Methods* 7, 9 (2010) (Referenced on p. 17).
- [94] López, M. P. et al. "In Vitro Reconstitution of Dynamic Microtubules Interacting with Actin Filament Networks". In: *Methods in Enzymology*. Ed. by Vale, R. D. Vol. 540. 2014 (Referenced on pp. 18, 93).
- [95] López, M. P. et al. "Actin-microtubule coordination at growing microtubule ends". *Nature Communications* (2014) (Referenced on pp. 17, 90).
- [96] Rodriguez, O. C. et al. "Conserved microtubule-actin interactions in cell movement and morphogenesis." *Nature Cell Biology* 5, 7 (2003) (Referenced on p. 17).
- [97] Huda, S. et al. "Microtubule guidance tested through controlled cell geometry." *Journal of Cell Science* 125, Pt 23 (2012) (Referenced on pp. 18, 71, 78, 90).
- [98] Etienne-Manneville, S. "Actin and microtubules in cell motility: Which one is in control?" *Traffic* 5, 7 (2004) (Referenced on p. 18).
- [99] Farina, F. et al. "The centrosome is an actin-organizing centre". *Nature Cell Biology* February (2015) (Referenced on p. 18).
- [100] Henty-Ridilla, J. L. et al. "Accelerated actin filament polymerization from microtubule plus ends". *Science* 352, 6288 (2016) (Referenced on p. 18).
- [101] Ridley, A. J. and Hall, A. "The small GTP-binding protein rho regulates the assembly of focal adhesions and actin stress fibers in response to growth factors". *Cell* 70, 3 (1992) (Referenced on pp. 18, 19).
- [102] Ridley, A. J. et al. "The small GTP-binding protein rac regulates growth factor-induced membrane ruffling". *Cell* 70, 3 (1992) (Referenced on p. 18).
- [103] Sit, S.-T. and Manser, E. "Rho GTPases and their role in organizing the actin cytoskeleton." *Journal of Cell Science* 124, Pt 5 (2011) (Referenced on p. 19).
- [104] Heasman, S. J. and Ridley, A. J. "Mammalian Rho GTPases: new insights into their functions from in vivo studies." *Nature Reviews. Molecular Cell Biology* 9, 9 (2008) (Referenced on p. 19).
- [105] Etienne-Manneville, S. and Hall, A. "Rho GTPases in cell biology." *Nature* 420, 6916 (2002) (Referenced on p. 19).
- [106] Jaffe, A. B. and Hall, A. "Rho GTPases: biochemistry and biology." *Annual Review of Cell and Developmental Biology* 21 (2005) (Referenced on p. 19).
- [107] Kong, F. et al. "Demonstration of catch bonds between an integrin and its ligand". *Journal of Cell Biology* 185, 7 (2009) (Referenced on p. 19).
- [108] Rivelino, D. et al. "Focal contacts as mechanosensors: Externally applied local mechanical force induces growth of focal contacts by an mDia1-dependent and ROCK-independent mechanism". *Journal of Cell Biology* 153, 6 (2001) (Referenced on p. 19).

- [109] Geiger, B., Spatz, J. P., and Bershadsky, A. D. “Environmental sensing through focal adhesions.” *Nature Reviews. Molecular Cell Biology* 10, 1 (2009) (Referenced on p. 19).
- [110] Bridgewater, R. E., Norman, J. C., and Caswell, P. T. “Integrin trafficking at a glance.” *Journal of Cell Science* 125, Pt 16 (2012) (Referenced on pp. 19, 82).
- [111] Legate, K. R. et al. “Genetic and cell biological analysis of integrin outside-in signaling Genetic and cell biological analysis of integrin outside-in signaling”. *Genes and Development* 23 (2009) (Referenced on p. 20).
- [112] Abram, C. L. and Lowell, C. A. “The ins and outs of leukocyte integrin signaling”. *Annu Rev Immunol* 27 (2009) (Referenced on p. 20).
- [113] Friedl, P. and Wolf, K. “Tumour-cell invasion and migration: diversity and escape mechanisms.” *Nature Reviews. Cancer* 3, 5 (2003) (Referenced on p. 20).
- [114] Shankar, J. et al. “Pseudopodial actin dynamics control epithelial-mesenchymal transition in metastatic cancer cells”. *Cancer Research* 70, 9 (2010) (Referenced on p. 20).
- [115] Caswell, P. T. et al. “Rab25 Associates with $\alpha 5 \beta 1$ Integrin to Promote Invasive Migration in 3D Microenvironments”. *Developmental Cell* 13, 4 (2007) (Referenced on p. 20).
- [116] Zand, M. S. and Albrecht-Buehler, G. “What structures, besides adhesions, prevent spread cells from rounding up?” *Cell Motility and the Cytoskeleton* 13, 3 (1989) (Referenced on p. 20).
- [117] Bar-Ziv, R. et al. “Pearling in cells: a clue to understanding cell shape.” *Proceedings of the National Academy of Sciences* 96, 18 (1999) (Referenced on pp. 20, 21).
- [118] Rayleigh, L. “On the instability of a cylinder of viscous liquid under capillary force”. *The London, Edinburgh, and Dublin Philosophical Magazine and Journal of Science* 34, 207 (1892) (Referenced on p. 21).
- [119] Albert, P. J. and Schwarz, U. S. “Modeling cell shape and dynamics on micropatterns”. *Cell Adhesion and Migration* 6918, June (2016) (Referenced on pp. 21, 22, 93, 139).
- [120] Ziebert, F., Swaminathan, S., and Aranson, I. S. “Model for self-polarization and motility of keratocyte fragments.” *Journal of the Royal Society, Interface* 9, 70 (2012) (Referenced on pp. 21, 22).
- [121] Guthardt Torres, P., Bischofs, I. B., and Schwarz, U. S. “Contractile network models for adherent cells”. *Physical Review E* 85, 1 (2012) (Referenced on p. 22).
- [122] Brand, C. “Forces and Flow of Contractile Networks”. PhD Thesis. Heidelberg University, 2015 (Referenced on pp. 22, 47, 52, 53, 63).
- [123] Albert, P. J. and Schwarz, U. S. “Dynamics of cell shape and forces on micropatterned substrates predicted by a cellular Potts model”. *Biophysical Journal* 106, 11 (2014) (Referenced on pp. 22, 57).

- [124] Shao, D., Rappel, W.-J., and Levine, H. “Computational Model for Cell Morphodynamics”. *Physical Review Letters* 105, 10 (2010) (Referenced on p. 22).
- [125] Löber, J., Ziebert, F., and Aranson, I. S. “Collisions of deformable cells lead to collective migration.” *Scientific Reports* 5 (2015) (Referenced on p. 22).
- [126] Sommer, C. et al. “Ilastik: Interactive learning and segmentation toolkit”. In: *Proceedings of the Eighth IEEE International Symposium on Biomedical Imaging*. 2011 (Referenced on p. 28).
- [127] Goodfellow, I., Bengio, Y., and Courville, A. *Deep Learning*. MIT Press (2016) (Referenced on p. 28).
- [128] Litjens, G. et al. “Deep learning as a tool for increased accuracy and efficiency of histopathological diagnosis.” *Scientific Reports* 6, April (2016) (Referenced on p. 28).
- [129] Deserno, T. M. *Biomedical Image Processing*. Springer (2011) (Referenced on p. 28).
- [130] Zitová, B. and Flusser, J. “Image registration methods: A survey”. *Image and Vision Computing* 21, 11 (2003) (Referenced on p. 28).
- [131] Goshtasby, A. A. *Image Registration: Principles, Tools and Methods* (2012) (Referenced on p. 29).
- [132] Yoo, T. S. et al. “Engineering and algorithm design for an image processing API: A technical report on ITK - The Insight Toolkit”. In: *Studies in Health Technology and Informatics*. Vol. 85. 2002 (Referenced on p. 29).
- [133] Mattes, D. et al. “PET-CT image registration in the chest using free-form deformations”. *IEEE Transactions on Medical Imaging* 22, 1 (2003) (Referenced on p. 29).
- [134] *ITK 4.5.0: Registration/MultiResImageRegistration1.cxx*. URL: https://itk.org/Doxygen45/html/Registration_2MultiResImageRegistration1_8cxx-example.html (visited on 08/18/2016) (Referenced on p. 29).
- [135] Shamonin, D. P. et al. “Fast parallel image registration on CPU and GPU for diagnostic classification of Alzheimer’s disease.” *Frontiers in Neuroinformatics* 7, January (2014) (Referenced on p. 29).
- [136] Marstal, K. *SimpleElastix*. URL: <http://simpleelastix.github.io/> (visited on 09/18/2016) (Referenced on p. 29).
- [137] Otsu, N. “A Threshold Selection Method from Gray Level Histograms”. *IEEE Transactions on Systems, Man and Cybernetics*. 9, 1 (1979) (Referenced on p. 30).
- [138] MacQueen, J. “Some methods for classification and analysis of multivariate observations”. In: *Proc. Fifth Berkeley Symp. on Math. Statist. and Prob.* Vol. 1. University of California Press, 1967 (Referenced on p. 30).

- [139] Manjon-Herrera, J. V. *kmeans image segmentation*. URL: <https://de.mathworks.com/matlabcentral/fileexchange/8379-kmeans-image-segmentation> (Referenced on p. 30).
- [140] Hough, P. “Method and means for recognizing complex patterns”. 1962 (Referenced on p. 32).
- [141] Duda, R. O. and Hart, P. E. “Use of the Hough transform to detect lines and curves in pictures”. *Communications of the Association Computing Machinery* 15, 1 (1972) (Referenced on p. 32).
- [142] Ballard, D. “Generalizing the Hough transform to detect arbitrary shapes”. *Pattern Recognition* (1981) (Referenced on p. 32).
- [143] Haidekker, M. A. *Advanced Biomedical Image Analysis* (2010) (Referenced on p. 32).
- [144] Illingworth, J. and Kittler, J. “A survey of the hough transform”. *Computer Vision, Graphics and Image Processing* 44, 1 (1988) (Referenced on p. 32).
- [145] Xu, L., Oja, E., and Kultanen, P. “A new curve detection method: randomized Hough transform (RHT)”. *Pattern Recognition Letters* 11 (1990) (Referenced on pp. 32, 33).
- [146] Freeman, W. T. and Adelson, E. H. “The Design and Use of Steerable Filters”. *IEEE Transactions on Pattern Analysis and Machine Intelligence* 13, 9 (1991) (Referenced on p. 34).
- [147] Eltzner, B. et al. “The filament sensor for near real-time detection of cytoskeletal fiber structures”. *PLoS ONE* 10, 5 (2015) (Referenced on pp. 34, 55).
- [148] Püspöki, Z. et al. “Transforms and Operators for Directional Bioimage Analysis: A Survey”. In: *Focus on Bio-Image Informatics*. Vol. 219. Advances in Anatomy, Embryology and Cell Biology. Springer International Publishing, 2016. Chap. 3 (Referenced on pp. 34, 36).
- [149] Jähne, B. *Digital Image Processing*. Springer (2005) (Referenced on pp. 34, 36).
- [150] Köthe, U. *Generische Programmierung für die Bildverarbeitung*. Books on Demand (2000) (Referenced on p. 36).
- [151] Köthe, U. “Reusable software in computer vision”. In: *Handbook of Computer Vision and Applications: Systems and Applications (Vol. 3)*. Ed. by Jähne, B., Haussecker, H., and Geissler, P. Vol. 3. San Diego: Academic Press, 1999 (Referenced on p. 36).
- [152] team, T. scikit-image development. *scikit-image*. URL: scikit-image.org (Referenced on p. 36).
- [153] Fisher, N. I. *Statistical Analysis of Circular Data*. Cambridge University Press (1996) (Referenced on p. 37).

- [154] Abràmoff, M. D. and Viergever, M. A. “Computation and visualization of three-dimensional soft tissue motion in the orbit”. *IEEE Transactions on Medical Imaging* 21, 4 (2002) (Referenced on p. 37).
- [155] Roberts, T. J. et al. “Estimating the motion of plant root cells from in vivo confocal laser scanning microscopy images”. *Machine Vision and Applications* 21 (2009) (Referenced on p. 37).
- [156] Amat, F., Myers, E. W., and Keller, P. J. “Fast and robust optical flow for time-lapse microscopy using super-voxels”. *Bioinformatics* 29, 3 (2013) (Referenced on p. 37).
- [157] Horn, B. K. P. and Schunck, B. G. “Determining optical flow”. *Artificial Intelligence* 17, 1-3 (1981) (Referenced on pp. 38, 39).
- [158] Baker, S. et al. “A database and evaluation methodology for optical flow”. *International Journal of Computer Vision* 92, 1 (2011) (Referenced on p. 38).
- [159] Fortun, D., Bouthemy, P., and Kervrann, C. “Optical flow modeling and computation: A survey”. *Computer Vision and Image Understanding* 134 (2015) (Referenced on p. 38).
- [160] Adrian, R. J. and Westerweel, J. *Particle Image Velocimetry* (2011) (Referenced on p. 38).
- [161] Pan, B. et al. “Two-dimensional digital image correlation for in-plane displacement and strain measurement: a review”. *Measurement Science and Technology* 20, 6 (2009) (Referenced on p. 38).
- [162] Paragios, N., Chen, Y., and Faugeras, O. *Handbook of Mathematical Models in Computer Vision*. Springer US (2006) (Referenced on pp. 38, 39).
- [163] Lucas, B. D. and Kanade, T. “An iterative image registration technique with an application to stereo vision”. In: *Proceedings of the 7th International Joint Conference on Artificial Intelligence*. x. 1981 (Referenced on p. 39).
- [164] Bradski, G. “The opencv library”. *Dr. Dobbs’s Journal of Software Tools* () (Referenced on p. 39).
- [165] Brox, T. et al. “High accuracy optical flow estimation based on a theory for warping”. In: *Proceedings of the 8th European Conference on Computer Vision*. Vol. 4. 2004 (Referenced on p. 39).
- [166] Bruhn, A. and Weickert, J. “Towards ultimate motion estimation: Combining highest accuracy with real-time performance”. In: *Proceedings of the IEEE International Conference on Computer Vision*. Vol. I. 2005 (Referenced on p. 39).
- [167] Sanchez, J., Monzon, N., and Salgado, A. “Robust optical flow estimation”. *Image Processing On Line* 3 (2013) (Referenced on pp. 39, 61).
- [168] Umbach, D. and Jones, K. “A few methods for fitting circles to data”. *IEEE Transactions on Instrumentation and Measurement* 52, 6 (2003) (Referenced on pp. 42, 52).

- [169] Hakkinen, K. M. et al. "Direct comparisons of the morphology, migration, cell adhesions, and actin cytoskeleton of fibroblasts in four different three-dimensional extracellular matrices." *Tissue engineering: Part A* 17, 5-6 (2011) (Referenced on pp. 45, 46).
- [170] Billington, N. et al. "Characterization of three full-length human nonmuscle myosin II paralogs". *Journal of Biological Chemistry* 288, 46 (2013) (Referenced on p. 54).
- [171] Beach, J. R. et al. "Nonmuscle myosin II isoforms coassemble in living cells". *Current Biology* 24, 10 (2014) (Referenced on pp. 54, 55).
- [172] Besser, A. and Schwarz, U. S. "Coupling biochemistry and mechanics in cell adhesion: A model for inhomogeneous stress fiber contraction". *New Journal of Physics* 9, 07 (2007) (Referenced on p. 55).
- [173] Albert, P. J., Erdmann, T., and Schwarz, U. S. "Stochastic dynamics and mechanosensitivity of myosin II minifilaments". *New Journal of Physics* 16 (2014) (Referenced on p. 57).
- [174] Schwarz, U. S. and Soiné, J. R. D. "Traction force microscopy on soft elastic substrates: A guide to recent computational advances". *Biochimica et Biophysica Acta - Molecular Cell Research* 1853, 11 (2015) (Referenced on p. 57).
- [175] Tseng, Q. et al. "A new micropatterning method of soft substrates reveals that different tumorigenic signals can promote or reduce cell contraction levels". *Lab on a Chip* 11, 13 (2011) (Referenced on p. 57).
- [176] Guillot, C. et al. "Mechanics of epithelial tissue homeostasis and morphogenesis." *Science* 340, 6137 (2013) (Referenced on p. 59).
- [177] Shaw, T. J. and Martin, P. "Wound repair at a glance." *Journal of Cell Science* 122, Pt 18 (2009) (Referenced on p. 59).
- [178] Deisseroth, K. "Optogenetics". *Nature Methods* 8, 1 (2011) (Referenced on p. 59).
- [179] Zemelman, B. V. et al. "Selective photostimulation of genetically chARGed neurons". *Neuron* 33, 1 (2002) (Referenced on p. 59).
- [180] Boyden, E. S. et al. "Millisecond-timescale, genetically targeted optical control of neural activity." *Nature Neuroscience* 8, 9 (2005) (Referenced on p. 59).
- [181] Tischer, D. and Weiner, O. D. "Illuminating cell signalling with optogenetic tools." *Nature Reviews. Molecular Cell Biology* 15, 8 (2014) (Referenced on p. 59).
- [182] Strickland, D. et al. "TULIPs: tunable, light-controlled interacting protein tags for cell biology." *Nature Methods* 9, 4 (2012) (Referenced on p. 59).
- [183] Oakes, P. W. et al. "Spatial Regulation of RhoA Reveals Zyxin-mediated Elasticity of Stress Fibers". *Submitted to eLife* (2016) (Referenced on pp. 61, 63, 68, 69, 171).
- [184] Smith, M. A. et al. "A Zyxin-mediated mechanism for actin stress fiber maintenance and repair". *Developmental Cell* 19, 3 (2010) (Referenced on p. 68).

- [185] CYTOO SA. *CYTOOCHIPS™ STARTER'S A X18*. URL: <https://cytoo.com/micropattern-products/chips/cytoochips%E2%84%A2-starters-x18> (visited on 08/19/2016) (Referenced on pp. 72, 82).
- [186] Schermelleh, L., Heintzmann, R., and Leonhardt, H. "A guide to super-resolution fluorescence microscopy". *Journal of Cell Biology* 190, 2 (2010) (Referenced on p. 73).
- [187] Pallavicini, C. et al. "Lateral motion and bending of microtubules studied with a new single-filament tracking routine in living cells". *Biophysical Journal* 106, 12 (2014) (Referenced on p. 73).
- [188] Brangwynne, C. P. et al. "Bending dynamics of fluctuating biopolymers probed by automated high-resolution filament tracking." *Biophysical Journal* 93, 1 (2007) (Referenced on p. 73).
- [189] Gerlitz, G., Reiner, O., and Bustin, M. "Microtubule dynamics alter the interphase nucleus". *Cellular and Molecular Life Sciences* 70, 7 (2013) (Referenced on p. 74).
- [190] Schauer, K. et al. "Probabilistic density maps to study global endomembrane organization." *Nature Methods* 7, 7 (2010) (Referenced on pp. 79, 80).
- [191] Schauer, K. et al. "A Novel Organelle Map Framework for High-Content Cell Morphology Analysis in High Throughput". *Journal of Biomolecular Screening* 19, 2 (2014) (Referenced on p. 79).
- [192] Grossier, J.-P. et al. "Cell adhesion defines the topology of endocytosis and signaling". *The EMBO journal* 33, 1 (2014) (Referenced on p. 79).
- [193] Collinet, C. et al. "Systems survey of endocytosis by multiparametric image analysis." *Nature* 464, 7286 (2010) (Referenced on p. 79).
- [194] Eskova, A. et al. "RNAi screen identifies KIF15 as a novel regulator of integrin endocytic trafficking." *Journal of Cell Science* (2014) (Referenced on pp. 79, 82).
- [195] Duong, T., Goud, B., and Schauer, K. "Closed-form density-based framework for automatic detection of cellular morphology changes." *Proceedings of the National Academy of Sciences* 109, 22 (2012) (Referenced on p. 80).
- [196] Scholz, F. W. and Stephens, M. A. "K-Sample Anderson-Darling Tests". *Journal of the American Statistical Association* 82, 399 (1987) (Referenced on p. 81).
- [197] Zhu, F. S. and Angie. *kSamples: K-Sample Rank Tests and their Combinations*. URL: <http://cran.r-project.org/package=kSamples> (Referenced on p. 81).
- [198] QIAGEN. *AllStars Negative Control siRNA*. URL: <https://www.qiagen.com/us/shop/rnai/allstars-negative-control-sirna/> (visited on 08/13/2016) (Referenced on p. 82).
- [199] Mosesson, Y., Mills, G. B., and Yarden, Y. "Derailed endocytosis: an emerging feature of cancer." *Nature reviews. Cancer* 8, 11 (2008) (Referenced on p. 82).

- [200] Mimori-Kiyosue, Y. et al. "CLASP1 and CLASP2 bind to EB1 and regulate microtubule plus-end dynamics at the cell cortex". *Journal of Cell Biology* 168, 1 (2005) (Referenced on pp. 89, 106).
- [201] Frey, F. "Physical Models for Cytoskeletal Organization and Intracellular Transport in Adherent Cells". Master Thesis, unpublished. Heidelberg University, 2015 (Referenced on pp. 90, 93, 98).
- [202] Allard, J. et al. "A mechanochemical model explains interactions between cortical microtubules in plants". *Biophysical Journal* 99, 4 (2010) (Referenced on pp. 90, 93).
- [203] Yu, H. et al. "High-quality binary protein interaction map of the yeast interactome network." *Science* 322, 5898 (2008) (Referenced on p. 91).
- [204] Karsenti, E., Nédélec, F., and Surrey, T. "Modelling microtubule patterns." *Nature Cell Biology* 8, 11 (2006) (Referenced on p. 91).
- [205] Wells, D. B. and Aksimentiev, A. "Mechanical properties of a complete microtubule revealed through molecular dynamics simulation". *Biophysical Journal* 99, 2 (2010) (Referenced on p. 91).
- [206] Jülicher, F. et al. "Modeling molecular motors". *Reviews of Modern Physics* 69, 4 (1997) (Referenced on p. 91).
- [207] Erdmann, T., Albert, P. J., and Schwarz, U. S. "Stochastic dynamics of small ensembles of non-processive molecular motors: The parallel cluster model". *Journal of Chemical Physics* 139, 17 (2013) (Referenced on p. 91).
- [208] Broedersz, C. P. and Mackintosh, F. C. "Modeling semiflexible polymer networks". *Reviews of Modern Physics* 86, 3 (2014) (Referenced on pp. 91, 97).
- [209] Prost, J., Jülicher, F., and Joanny, J. F. "Active gel physics". *Nature Physics* 11, February (2015) (Referenced on pp. 91, 92).
- [210] Kratky, O. and Porod, G. "Röntgenuntersuchung Gelöster Fadenmoleküle". *Recueil des Travaux Chimiques des Pays-Bas-Journal of the Royal Netherlands Chemical Society* 68, 12 (1949) (Referenced on p. 91).
- [211] Heussinger, C., Bathe, M., and Frey, E. "Statistical mechanics of semiflexible bundles of wormlike polymer chains". *Physical Review Letters* 99, 4 (2007) (Referenced on p. 91).
- [212] Wilhelm, J. and Frey, E. "Elasticity of stiff polymer networks." *Physical review letters* 91 (2003) (Referenced on p. 92).
- [213] Head, D. a., Levine, A. J., and MacKintosh, F. C. "Deformation of Cross-Linked Semiflexible Polymer Networks". *Physical Review Letters* 91, 10 (2003) (Referenced on p. 92).
- [214] Huisman, E. M., Storm, C., and Barkema, G. T. "Monte Carlo study of multiply crosslinked semiflexible polymer networks". *Physical Review E - Statistical, Nonlinear, and Soft Matter Physics* 78, 5 (2008) (Referenced on p. 92).

- [215] Andrews, S. S. “Methods for modeling cytoskeletal and DNA filaments.” *Physical Biology* 11, 1 (2014) (Referenced on p. 92).
- [216] Nédélec, F. and Foethke, D. “Collective Langevin dynamics of flexible cytoskeletal fibers”. *New Journal of Physics* 9 (2007) (Referenced on pp. 92, 104, 105).
- [217] Surrey, T. et al. “Physical properties determining self-organization of motors and microtubules.” *Science* 292, 5519 (2001) (Referenced on p. 92).
- [218] Letort, G. et al. “Geometrical and mechanical properties control actin filament organization.” *PLoS Computational Biology* 11, 5 (2015) (Referenced on pp. 92, 105).
- [219] Nédélec, F. J. et al. “Self-organization of microtubules and motors.” *Nature* 389, 6648 (1997) (Referenced on p. 92).
- [220] Schaller, V. et al. “Polar patterns of driven filaments.” *Nature* 467, 7311 (2010) (Referenced on p. 92).
- [221] Tee, Y. H. et al. “Cellular chirality arising from the self-organization of the actin cytoskeleton”. *Nature Cell Biology* 17, 4 (2015) (Referenced on p. 92).
- [222] Reymann, A.-C. et al. “Nucleation geometry governs ordered actin networks structures.” *Nature materials* 9, 10 (2010) (Referenced on p. 92).
- [223] Kruse, K. et al. “Generic theory of active polar gels: a paradigm for cytoskeletal dynamics”. *European Physical Journal E* 16, 1 (2005) (Referenced on p. 92).
- [224] Jülicher, F. et al. “Active behavior of the Cytoskeleton”. *Physics Reports* 449, 1-3 (2007) (Referenced on p. 92).
- [225] Marchetti, M. C. et al. “Hydrodynamics of soft active matter”. *Reviews of Modern Physics* 85, 3 (2013) (Referenced on p. 92).
- [226] Kruse, K. et al. “Asters, Vortices, and Rotating Spirals in Active Gels of Polar Filaments”. *Physical Review Letters* 92, 7 (2004) (Referenced on p. 92).
- [227] Gupta, M. et al. “Adaptive rheology and ordering of cell cytoskeleton govern matrix rigidity sensing”. *Nature Communications* 6, May (2015) (Referenced on p. 92).
- [228] Brugués, J. and Needleman, D. “Physical basis of spindle self-organization”. *Proceedings of the National Academy of Sciences* 111, 52 (2014) (Referenced on pp. 92, 122).
- [229] Foster, P. J. et al. “Active contraction of microtubule networks.” *eLife* 4 (2015) (Referenced on p. 92).
- [230] Gennes, P.-G. de and Prost, J. *The Physics of Liquid Crystals*. Clarendon Press (1993) (Referenced on pp. 92, 120, 121, 123, 125, 128).
- [231] Letort, G. et al. “Centrosome centering and decentering by microtubule network rearrangement”. *Molecular Biology of the Cell* (2016) (Referenced on pp. 93, 105, 116, 146).

- [232] Ma, R. et al. “General theory for the mechanics of confined microtubule asters”. *New Journal of Physics* 16, 1 (2014) (Referenced on p. 93).
- [233] Zhu, J. et al. “Finding the Cell Center by a Balance of Dynein and Myosin Pulling and Microtubule Pushing: A Computational Study”. *Molecular Biology of the Cell* 21, 24 (2010) (Referenced on pp. 93, 146).
- [234] Hely, T. a. and Willshaw, D. J. “Short-term interactions between microtubules and actin filaments underlie long-term behaviour in neuronal growth cones.” *Proceedings of the Royal Society of London B* 265 (1998) (Referenced on p. 93).
- [235] Mehrbod, M. and Mofrad, M. R. K. “On the significance of microtubule flexural behavior in cytoskeletal mechanics”. *PLoS ONE* 6, 10 (2011) (Referenced on p. 93).
- [236] Fürth, R. “Die Brownsche Bewegung bei Berücksichtigung einer Persistenz der Bewegungsrichtung. Mit Anwendungen auf die Bewegung lebender Infusorien”. *Zeitschrift für Physik* 2, 3 (1920) (Referenced on p. 98).
- [237] Gail, M. H. and Boone, C. W. “The locomotion of mouse fibroblasts in tissue culture.” *Biophysical Journal* 10, 10 (1970) (Referenced on p. 98).
- [238] Kampen, N. V. *Stochastic Processes in Physics and Chemistry*. Elsevier (2007) (Referenced on p. 99).
- [239] Burakov, A. et al. “Centrosome positioning in interphase cells”. *Journal of Cell Biology* 162, 6 (2003) (Referenced on pp. 99, 115, 145, 146).
- [240] Janson, M. E., De Dood, M. E., and Dogterom, M. “Dynamic instability of microtubules is regulated by force”. *Journal of Cell Biology* 161, 6 (2003) (Referenced on p. 101).
- [241] Lemons, D. S. *An Introduction to Stochastic Processes in Physics*. John Hopkins University Press (2002) (Referenced on p. 104).
- [242] Purcell, E. “Life at low Reynolds number”. *American Journal of Physics* 45, 1 (1977) (Referenced on p. 104).
- [243] Limbach, H. J. et al. “ESPReso—an extensible simulation package for research on soft matter systems”. *Computer Physics Communications* 174, 9 (2006) (Referenced on p. 104).
- [244] Andrews, S. S. and Bray, D. “Stochastic simulation of chemical reactions with spatial resolution and single molecule detail.” *Physical biology* 1, 3-4 (2004) (Referenced on p. 104).
- [245] Schöneberg, J. and Noé, F. “ReaDDy—a software for particle-based reaction-diffusion dynamics in crowded cellular environments.” *PloS one* 8, 9 (2013) (Referenced on p. 104).
- [246] Kozłowski, C., Srayko, M., and Nedelec, F. “Cortical Microtubule Contacts Position the Spindle in *C. elegans* Embryos”. *Cell* 129, 3 (2007) (Referenced on p. 105).

- [247] Loughlin, R., Heald, R., and Nédélec, F. “A computational model predicts *Xenopus* meiotic spindle organization”. *Journal of Cell Biology* 191, 7 (2010) (Referenced on p. 105).
- [248] Lukinavičius, G. et al. “Fluorogenic probes for live-cell imaging of the cytoskeleton.” *Nature Methods* 11, 7 (2014) (Referenced on p. 116).
- [249] Chaikin, P. and Lubensky, T. C. *Principles of Condensed Matter Physics*. Cambridge University Press (2006) (Referenced on pp. 119–121).
- [250] Landau, L. D. “On the theory of phase transitions”. *Zh. Eks. Teor. Fiz.* 7, 1937 (1937) (Referenced on p. 119).
- [251] Wikimedia Commons. *Schlieren texture of liquid crystal nematic phase*. URL: https://commons.wikimedia.org/wiki/File:Nematische_Phase_Schlierentextur.jpg (visited on 08/31/2016) (Referenced on p. 121).
- [252] Hitt, A. L., Cross, A. R., and Williams, R. C. “Microtubule Solutions Display Nematic Liquid Crystalline Structure”. *Journal of Biological Chemistry* 265, 3 (1990) (Referenced on p. 122).
- [253] Sanchez, T. et al. “Spontaneous motion in hierarchically assembled active matter.” *Nature* 491, 7424 (2012) (Referenced on p. 122).
- [254] Giomi, L. et al. “Defect annihilation and proliferation in active Nematics”. *Physical Review Letters* 110, 22 (2013) (Referenced on p. 122).
- [255] Keber, F. C. et al. “Topology and dynamics of active nematic vesicles”. *Science* 345, 6201 (2014) (Referenced on p. 122).
- [256] Kamien, R. D., Le Doussal, P., and Nelson, D. R. “Theory of directed polymers”. *Physical Review A* 45, 12 (1992) (Referenced on p. 122).
- [257] Oseen, C. W. “The theory of liquid crystals”. *Transactions of the Faraday Society* 29, 1 (1933) (Referenced on p. 123).
- [258] Zocher, H. “The effect of a magnetic field on the nematic state”. *Transactions of the Faraday Society* 29, 140 (1933) (Referenced on p. 123).
- [259] Frank, F. C. “I. Liquid crystals. On the theory of liquid crystals”. *Discussions of the Faraday Society* 25, I (1958) (Referenced on p. 123).
- [260] Virga, E. G. *Variational theories for liquid crystals*. Chapman & Hall (1994) (Referenced on p. 123).
- [261] Andrienko, D. *Introduction to liquid crystals*. URL: <http://www2.mpi-mainz.mpg.de/~andrienk/teaching/IMPRS/> (Referenced on p. 123).
- [262] De Gennes, P. G. “Short Range Order Effects in the Isotropic Phase of Nematics and Cholesterics”. *Molecular Crystals and Liquid Crystals* 12, 3 (1971) (Referenced on p. 123).
- [263] Landau, L. D. and Lifshitz, E. M. *Statistical Physics, Part 1*. Pergamon Press (1980) (Referenced on pp. 123, 125).

- [264] Mottram, N. J. and Newton, C. J. P. “Introduction to Q-tensor theory”. *arXiv preprint arXiv:1409.3542* (2014) (Referenced on pp. 123, 125–127).
- [265] Luo, C., Majumdar, A., and Erban, R. “Multistability in planar liquid crystal wells”. *Physical Review E* 85, 6 (2012) (Referenced on pp. 124, 128, 132, 133).
- [266] Majumdar, A. “The Landau-de Gennes theory of nematic liquid crystals: Uniaxiality versus Biaxiality”. *Communications on Pure and Applied Analysis* 11, 3 (2011) (Referenced on p. 124).
- [267] Ball, J. M. *Mathematics of liquid crystals, Cambridge Centre for Analysis short course*. URL: <https://people.maths.ox.ac.uk/ball/teaching.shtml> (visited on 04/22/2014) (Referenced on p. 126).
- [268] Rapini, A. and Papoular, M. “Distortion d’une lamelle nématique sous champ magnétique conditions d’ancrage aux parois”. *Le Journal de Physique Colloques* 30, C4 (1969) (Referenced on p. 128).
- [269] Nobili, M. and Durand, G. “Disorientation-induced disordering at a nematic-liquid-crystal-solid interface”. *Physical Review A* 46, 10 (1992) (Referenced on p. 128).
- [270] Gruhn, T. and Hess, S. “Monte Carlo simulation of the director field of a nematic liquid crystal with three elastic coefficients”. *Zeitschrift für Naturforschung - Section A Journal of Physical Sciences* 51, 1-2 (1996) (Referenced on p. 130).
- [271] Logg, A., Mardal, K.-A., and Wells, G. *Automated Solution of Differential Equations by the Finite Element Method*. Springer (2012) (Referenced on pp. 130–132).
- [272] Brenner, S. C. and Scott, L. R. *The mathematical theory of finite element methods*. Springer (2008) (Referenced on p. 131).
- [273] COMSOL Inc. *COMSOL Multiphysics® Modeling Software*. URL: www.comsol.com (Referenced on p. 132).
- [274] Bangerth, W., Hartmann, R., and Kanschat, G. “deal.II—A general-purpose object-oriented finite element library”. *ACM Transactions on Mathematical Software* 33, 4 (2007) (Referenced on p. 132).
- [275] Dedner, A. et al. “A generic interface for parallel and adaptive discretization schemes: abstraction principles and the Dune-Fem module”. *Computing* 90, 3-4 (2010) (Referenced on p. 132).
- [276] Dogterom, M. and Bernard, Y. “Measurement of the Force-Velocity Relation for Growing Microtubules”. *Science* 278, 5339 (1997) (Referenced on p. 146).
- [277] Daniels, B. R., Masi, B. C., and Wirtz, D. “Probing single-cell micromechanics in vivo: the microrheology of *C. elegans* developing embryos.” *Biophysical journal* 90, 12 (2006) (Referenced on p. 146).

- [278] Waldecker, M. et al. “Differential time-dependent volumetric and surface area changes and delayed induction of new permeation pathways in *P. falciparum* - infected hemoglobinopathic erythrocytes”. *Cellular Microbiology* (2016) (Referenced on p. 171).

List of abbreviations

ADP Adenosine diphosphate	PSF Point spread function
AF Actin filament	RHT Randomized Hough transform
ATP Adenosine triphosphate	RNAi RNA interference
CSK Cytoskeleton	ROCK Rho-associated kinase
ECM Extracellular matrix	SF Stress fiber
FA Focal adhesion	SIM Structured illumination microscopy
FEM Finite-element method	siRNA Small interfering RNA
GAP GTPase-activating protein	SNR Signal-to-noise ratio
GDP Guanosine-diphosphate	STED Stimulated emission depletion
GEF Guanine nucleotide exchange factor	STORM Stochastic optical reconstruction microscopy
GFP Green fluorescent protein	WLC Wormlike chain
GTP Guanosine-triphosphate	
LC Liquid crystal	
MP Micropattern	
MT Microtubule	
MTOC Microtubule organizing center	
OF Optical flow	
PALM Photoactivated localization microscopy	
PDMS Poly(dimethylsiloxane)	
PRW Persistent random walk	

List of manuscripts

The following manuscripts have been published or drafted during the course of this thesis. The first paper, in which I contributed to the segmentation and shape analysis of Malaria infected red blood cells, is not included in the main text.

Waldecker, M., Dasanna, A. K., Lansche, C., Linke, M., Srismith, S., Cyrklaff, M., Sanchez, C. P., Schwarz, U. S., Lanzer, M. “Differential time-dependent volumetric and surface area changes and delayed induction of new permeation pathways in <i>P. falciparum</i> - infected hemoglobinopathic erythrocytes”. <i>Cellular Microbiology</i> (2016). DOI: 10.1111/cmi.12650	[278]
Oakes, P. W., Wagner, E., Brand, C. A., Probst, D., Linke, M., Schwarz, U. S., Glotzer, M., Gardel, M. L. “Spatial Regulation of RhoA Reveals Zyxin-mediated Elasticity of Stress Fibers” <i>Submitted</i>	Chapter 4
Linke, M. Frey, F., Nedelec, F., Starkuviene-Erfle, V., Schwarz U. S. “Modeling of microtubule-actin coordination in cells on micropatterns” <i>In preparation</i>	Chapters 5, 8 and 9
Linke M., Reusing, S., Albert, P. J., Garbenciute, G., Gunkel, M., Valiokas, R., Erfle, H., Schwarz U. S., Starkuviene-Erfle, V. “Integrin endocytosis in micropatterned cells” <i>In preparation</i>	Chapter 6
Brand, C., Linke M., Weißenbruch, K., Richter, B., Bastmeyer, M., Schwarz, U. S. “Active cable model explains cell shape in three-dimensional microscavolds” <i>In preparation</i>	Section 3.2
Weißenbruch, K., Linke M., Brand, C., Richter, B., Schwarz, U. S., Bastmeyer, M. and co-workers “Analysis and modeling of stress fiber microstructure” <i>In preparation</i>	Section 3.3

Danksagung

Zunächst möchte ich meinem Betreuer Ulrich Schwarz dafür danken, dass er mich in seine Arbeitsgruppe aufgenommen hat, mir ermöglicht hat diese Arbeit anzufertigen und mir stets mit hilfreichen Tipps, Anregungen und Diskussionen zur Seite stand. Von ihm konnte ich sehr viel über Physik, Biophysik und die wissenschaftliche Forschung lernen.

Heinz Horner danke ich für sein Interesse und die Begutachtung meiner Arbeit.

Die Arbeit an den vorgestellten Themen wäre nicht ohne die zahlreichen Kollaborationen möglich gewesen. Vor allem möchte ich mich für die Finanzierung durch das MEHTRICS Projekt bedanken. Allen meinen Kooperationspartnern, Vytaute Starkuviene-Erfle, Susanne Reusig, Manuel Gunkel und Johann Engelhardt aus dem BioQuant in Heidelberg, Benjamin Richter, Kai Weißenbruch und Martin Bastmeyer aus Karlsruhe, Patrick Oakes, Margaret Gardel, Elizabeth Wagner und Michael Glotzer aus Chicago sowie Francois Nedelec vom EMBL, danke ich dafür, dass sie ihre Daten mit mir geteilt haben und außerdem für den interessanten Austausch zu biologischen und technischen Fragestellungen. Fred Hamprecht und seiner Arbeitsgruppe danke ich für hilfreiche Tipps zur Bildverarbeitung.

Melinda Feucht und dem Team der BioQuant-IT gebührt mein Dank für die Unterstützung bei Computerproblemen und für die Sicherstellung einer reibungslos funktionierenden Infrastruktur.

Außerordentlicher Dank gebührt allen derzeitigen und früheren Mitgliedern der Arbeitsgruppe Schwarz, die diese Zeit sehr unterhaltsam gemacht haben. Insbesondere sind hier Christoph Brand, Philipp Albert, Anil Kumar Dasanna, Felix Frey und Dimitri Probst für die gute Zusammenarbeit und den Austausch über verschiedenste Projekten zu nennen. Meinen Bürokollegen Anna Battista, Christoph Brand, Anil Kumar Dasanna, Fabian Fuchs und Nikolas Schnellbacher sei für die vielen interessanten Diskussionen über Wissenschaft, das Leben, das Universum und den ganzen Rest gedankt. Max Hoffman danke ich für die Organisation von Reisen zu Konferenzen, Jerome Soine für unsere Experimente mit Fluggeräten und Marvin Böttcher für all die Stunden an künstlichen und echten Felsen.

Miriam, ich danke dir von ganzem Herzen für all deine Liebe, die großartige Unterstützung und dein Verständnis während des Schreibens dieser Arbeit und weit darüber hinaus.

Meiner Familie danke ich dafür, dass sie mir das Studium der Physik ermöglicht haben und mich stets in allen Lebenslagen unterstützen.